Biogenic gas bubble dynamics in a Northern peatland observed using electrical geophysics and other methods

By

Neil Terry

A dissertation submitted to the

Graduate School-Newark

Rutgers, The State University of New Jersey

In partial fulfillment of the requirements

For the degree of

Doctor of Philosophy

Graduate Program in Environmental Science

Written under the direction of

Lee Slater

And approved by

_____

_____

_____

_____

Newark, New Jersey

January, 2017

ABSTRACT OF THE DISSERTATION

Biogenic gas bubble dynamics in a Northern peatland observed using electrical geophysical methods

By NEIL TERRY

Dissertation Director:

Professor Lee Slater

The ability of peatlands to produce, sequester, and release large volumes of greenhouse gases (particularly methane) has resulted in a large body of research dedicated toward understanding how these soils respond to climactic variations. Yet, there still exist many uncertainties regarding variation in the mechanisms that drive the production, storage, and release of methane in peatlands, in part due to limited information at relevant spatiotemporal scales. This work harnesses the power of geophysical methods to bridge this information gap and offer new insights on the mechanics of biogenic gas dynamics in peatlands.

The first portion of this work develops a methodological basis for monitoring field-scale biogenic gas variations in peatlands from electrical resistivity imaging (ERI). This approach is used to provide insight on the controlling factors that drive methane ebullition, particularly from deep peat regimes (i.e., below 1 m) that are difficult to sample with traditional methods. Using this technique, anomalous variations in resistivity are observed that correspond to decreases in atmospheric pressure and suggest that biogenic gas releases occur throughout the peat profile. Furthermore, smaller

changes in resistivity seem to correspond well with expected variations in gas bubble size due to changing pressure and temperature conditions.

A follow up study examines two sites in Caribou Bog, Maine in an effort to understand how peat structural and hydrogeological properties influence gas releases. This study employs a suite of direct methods (i.e., direct coring, methane flux monitoring, and gas sample collection), geochemical and environmental data, and indirect geophysical methods (ERI, ground penetrating radar, and peat deformation) to show that peat structure and underlying hydrogeology likely play a critical role in controlling methane production and release. It is observed that a highly decomposed peat site overlying an esker deposit exhibits larger methane content, larger magnitude resistivity variations (particularly in deep peat), and larger individual methane flux measurements compared to a less well decomposed peat site nearby.

The concluding piece of this research develops a quantitative technique to estimate biogenic gas bubble size from frequency information derived from ground penetrating radar signals. Bubble size may be a critical parameter governing methane ebullition given the increased buoyancy and reduced oxidation potential of larger bubbles. Additionally, previous research has demonstrated a disproportionately large percentage of the total methane flux may originate from large bubbles. The approach is used to estimate bubble size variations in two laboratory studies as well as from field data, and suggests that bubbles with radii of greater than 0.04 m may exist in natural peat deposits. Employing this estimation approach in the future may help to understand the connection between bubble size, peat type/structure, and fluxes observed at the surface.

Preface

I have been honored to work with Lee Slater as my PhD advisor. His guidance, unflagging faith, kindness, positivity, and devotion to science have both enabled me to succeed and truly inspired me throughout my time at Rutgers.

It has also been a great pleasure to work with Xavier Comas on numerous field campaigns and manuscripts. His uniqueness, selfless generosity and determination both in the field and during manuscript preparation have been a crucial part to my completing this PhD. Other mentors I am thankful to are and Kristina Keating, for helping me to develop mathematical and computational skills and providing me opportunities to grow professionally, and Dimitrios Ntarlagiannis, for the opportunities he provided me in the lab and field to hone my skills and become a more well-rounded geophysicist. Also, I remain indebted to Zhangshuan Hou for taking me in as an M.S. student and passing on a unique quantitative skillset that continues to be useful in my research.

I thank Karina Schäfer and Andrew Reeve for their hospitality, assistance with data, and critical review, as well as Andrew Parsekian for initiating me to Rutgers and for his incredible responsiveness to data requests. I am very appreciative of Andrew Binley's assistance and useful correspondence regarding ERI inversion tools, and I am grateful to Liz Morrin for her frankness and efficiency in kindly sorting out countless travel and logistical issues.

A special thanks to all of those involved in the 2011 – 2013 Caribou Bog field research campaigns – making these trips both fun scientifically rich. In addition to some already named above, this includes Wagner Alcivar, Jonathan Algeo, Zachary Freeburg, Barbara Goldman, Deborah Gonzalez, Gerhard Heij, Evan Lewis, Paul Monahan,

Adriana Morocho, Kisa Mwakanyamale, Sundeep Sharma, William Wright, and Zhongjie Yu.

I am also appreciative of my fellow students and office mates, who were all kind and supportive during my time at Rutgers, including Jon Algeo, Sweeta Chauhan, Xi Chen, Mehrez Elwaseif, Jeff Heenan, Kisa Mwakanyamale, Gordon Osterman, Yves Persona, Judy Robinson, and Chi Zhang.

Financial support for this research was provided by the National Science Foundation. I am very grateful to be having been funded for this project as a Graduate Research Assistant.

Finally, my sincerest gratitude goes to Anna Scime as well as my family and friends for all of their encouragement during this PhD.

TABLE OF CONTENTS

LIST OF TABLES

LIST OF ILLUSTRATIONS

Chapter 1: Introduction

1.1 Background and overview

Northern peatlands fix significant carbon dioxide (CO_2), yet account for an estimated 5-10% of the annual global methane (CH_4) flux to the atmosphere [*Charman*, 2002]. The past, present, and future effect of peatlands on climate change is unclear, largely due to incomplete understanding of greenhouse gas dynamics within peatlands. An ongoing research challenge in peatlands research is to build quantitative models that link environmental variables to methane fluxes.

Peatlands consist of waterlogged organic soil where the rate of accumulation exceeds the rate of decomposition. In peat, the predominantly saturated, anoxic conditions favor methanogenesis as a means of microbial respiration. Under anoxic conditions where inorganic terminal electron acceptors (TEAs) like nitrate, ferric iron, manganese, or sulfate are available, CO_2 is predominantly produced [*Ye et al.*, 2012]. When these nutrients are depleted, CO_2 and/or acetic acid act as TEAs (as opposed to oxygen) [*Drake et al.*, 2009], and CO_2 and CH_4 are produced by methanogens in roughly equal amounts. Where oxygen is available, CO_2 is the primary gas byproduct of microbial respiration, and CH_4 is to some extent oxidized. The rate at which microbes produce these gases is influenced, often nonlinearly, by factors such as temperature, water table position, pH, and nutrient supply [*Chasar et al.*, 2000a; *Paul et al.*, 2006; *Jaatinen et al.*, 2007; *Keller and Bridgham*, 2007]. The gas that is produced may undergo further chemical reactions, remain trapped in the peat, and/or migrate upwards from its initial position to higher up in the peat or leave the soil entirely to enter the atmosphere.

Although CH_4 flux to the atmosphere can occur through diffusion and vascular transport, the contributions to total flux due to episodic ebullition (bubbling) events are a source of great uncertainty. Although it is now recognized that changes in atmospheric pressure stimulate episodic ebullition events [*Comas et al.*, 2011a; *Kellner et al.*, 2006; *Kettridge et al.*, 2011; *Tokida et al.*, 2005a, 2007; *Waddington et al.*, 2009], conceptual models describing the processes that contribute to methane ebullition are still uncertain, although two have been proposed.

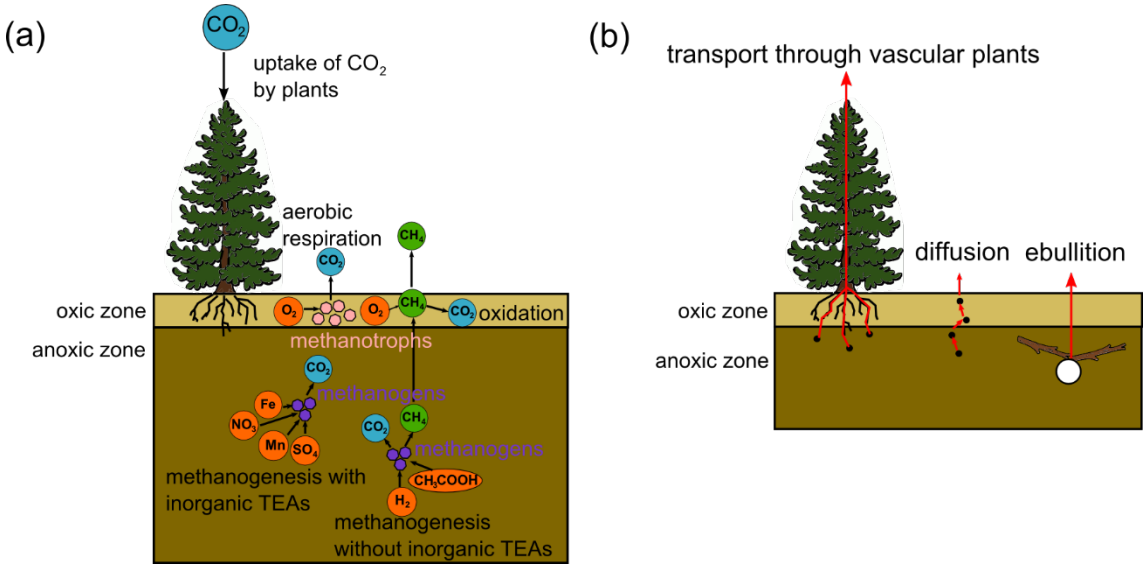

Figure 1.1 – simple conceptual diagrams of (a) biogenic gas production and (b) the three mechanisms for biogenic gas release from peatlands.

The 'deep peat model' [*Glaser et al.*, 2004], developed from a suite of geodetic and hydrogeological observations in the Glacial Lake Agassiz Peatlands (GLAP), posits that labile carbon is provided to methanogens in the deep peat, where anaerobic conditions allow for enhanced (relative to shallow peat) production of methane. Methanogens produce gas that is trapped in semi-confining layers until falling water

levels and/or dropping atmospheric pressure cause the semi-confining layer to rupture and release gas to the atmosphere. The sudden release of gas causes surface deformation.

The 'shallow peat model' [*Coulthard et al.*, 2009], developed from a collection of laboratory and field-based studies of shallow peat, instead highlights the significant contribution of methane accumulation that occurs just below the water table, with an unknown upward flux of methane from the deep peat. This model is based on the large episodic ebullition fluxes (observed at rates greater than 1000 mg CH_4 m^{-2} d^{-1} [*Rosenberry et al.*, 2003]) that originate in the shallow peat. The shallow peat model does not deny the potential importance of deep peat contributions to ebullition, but rather states that these contributions are not as well quantified as those in the shallow peat.

This work develops geophysical tools in tandem with traditional techniques to study the magnitude, frequency, and driving forces behind methane ebullition. In particular, I focus on electrical geophysical methods, such as direct current electrical resistivity imaging (ERI) and ground penetrating radar (GPR), as a means to study these processes at an intermediate scale (processes occurring on scales of sub-meter to 10s of meters).

ERI is a technique that was initially developed for natural resource exploration but has recently seen increasing use in environmental investigations, particularly for observing time-lapse processes (see *Singha et al.* [2014] for a review). Using several electrodes implanted in the Earth's surface, current is injected at a given pair of electrodes and voltage is measured across several other pairs (Figure 1.1a). The flow of current is directly influenced by the resistivity of the Earth. Thus, the data can be used to construct an image of the resistivity structure of the subsurface. Resistivity is, in turn, a

parameter that is influenced by environmental properties of interest, particularly lithology and water content. Laboratory-based studies have used ERI for monitoring changes in gas content in peat [*Slater et al.*, 2007; *Kettridge et al.*, 2011], but field-scale studies of this nature have not previously been performed.

GPR uses radio waves to study near surface (less than 100 meters deep) phenomena. A radio pulse with a given center frequency is directed into the ground, while a receiver nearby records the elapsed time and the returned pulse (Figure 1.1b). The velocity, energy, and propagation path of these waves are sensitive to contrasts in electromagnetic properties within the earth. The larger the contrast in electromagnetic properties, the more energy reflected back to the surface. Typically, one analyzes GPR data in the time domain; by looking at the magnitude of the returned radio pulse through time. This approach has been applied to monitoring changes in peatland biogenic gas content through observing changes in the time required for GPR energy to propagate through peat and applying a petrophysical transformation given information on porosity and the dielectric permittivity of constituent materials (e.g., *Comas et al.* [2005a]; *Comas et al.* [2005c]; *Comas et al.* [2007], *Strack and Mierau* [2010]; *Parsekian et al.* [2010, 2011]). In contrast, time-frequency domain analysis also examines the frequency, or spectral content of the returned pulse to potentially yield information on parameters that are frequency dependent, such as the attenuation (or energy decay) of GPR waves. Attenuation is in turn affected by the electrical conductivity and size and composition of particles in the medium being studied. Such analysis has not previously been performed in the context of peatland biogenic gas dynamics.

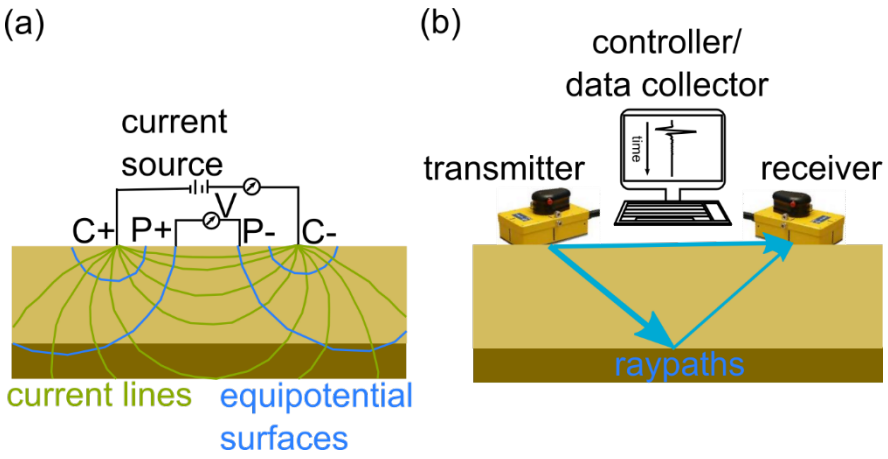

Figure 1.2 – basic schematic of (a) an ERI survey and (b) a GPR survey.

1.2 Research objectives

This work endeavors to accomplish three primary tasks, along with several secondary objectives:

1. Develop a methodology for field scale analysis of biogenic gas variation from ERI data.
    a. Explore autonomous ERI monitoring as a tool for monitoring biogenic gas content variation in peat;
    b. Explore the influence of environmental variables, particularly atmospheric pressure and water levels, in triggering methane release from peat;

2. Determine spatiotemporal variability in gas dynamics at two peatland sites in Caribou Bog, Maine.
    a. Find evidence to support models of carbon cycling in peat (the 'shallow peat model' *vs.* the 'deep peat model');
    b. Explain differences in biogenic gas dynamics at the two sites in terms of peat structural properties, biogeochemistry, and underlying hydrogeology;

3. Develop a technique for estimating biogenic gas bubble size from GPR frequency information.
    a. Provide the mathematical foundation for estimating frequency-dependent scattering attenuation of a GPR signal based on Mie theory;
    b. Test this approach on two lab datasets and a field dataset;
    c. Draw inferences on the size of bubbles in Caribou Bog, Maine.

1.3 Summary of work and general findings

The next three chapters of this dissertation are comprised of a published paper and two submitted papers.

1.3.1 Autonomous ERI monitoring of peatland gas dynamics

The first paper, published in 2016 in *Water Resources Research*, tackles the first research objective outlined in section 1.2 above: the use of autonomous ERI to estimate biogenic gas content variations in a natural peatland. In this study, an ERI system is set to collect resistivity data over a period of several months on a sampling interval of several hours. The results show distinctly layered variations in resistivity, which are linked to variations in gas content through petrophysical models. These layered variations most often manifest as a loss of gas from shallow peat and an increase in gas content in the deep peat, and often correspond to drops in atmospheric pressure. A strong negative correlation with water levels throughout much of the sampling volume is also observed, which is interpreted as an immediate response of bubble volume to hydrostatic pressure changes as predicted by the Ideal Gas Law. This paper highlights the enormous benefits of ERI in studying natural biogenic gas dynamics: the non-invasive sampling of a 3D volume (including deep peat), the intermediate spatiotemporal scale of

measurement, and the ability to collect data autonomously. The limitations of this approach are also presented: the indirect nature of sampling (it is shown that a quantifiable estimate of gas content is unrealistic at the field scale) and the spatiotemporal 'blurring' of final images due to constraints necessary to carry out the numerical inversion of the raw data.

1.3.2 Multimethod approach to observe hydrogeological and peat structural influences on biogenic gas dynamics in peatlands: comparison of two sites

The second paper, submitted in 2016 to *Journal of Geophysical Research – Biogeosciences*, builds on the first paper by examining several additional datasets in addition to ERI at two field sites in Caribou Bog, Maine. This paper directly addresses the second research objective outlined in section 1.2 above. Each dataset provides clues as to the underlying biogenic gas dynamics at the two sites to reveal distinct characteristics at each site that support both shallow and deep peat models. Each site is initially characterized through coring, common offset GPR, and ERI. The first 'pools' site has numerous pools of water at the surface and is underlain by a permeable esker deposit, whereas the second 'wooded heath' site has a clay mineral soil and no standing pools. In terms of peat properties, the pool site shows increasing decomposition with depth and chaotic GPR reflection events (likely generated from less decomposed debris semi-randomly distributed throughout the peat), whereas the wooded heath site shows less decomposition at depth and subhorizontal, mostly continuous GPR reflection events. Common midpoint GPR data are used to generate 1D estimates of gas content with depth at both sites and show significantly higher gas content (roughly 14%) at depth at the wooded heath site. This general pattern is consistent with data from moisture probes

inserted in the peat at each site. The ERI data show distinctive patterns as well, with activity predominantly occurring over the esker deposit at the pools site, while the wooded heath site shows generally horizontally homogeneous variations. Measurements of peat deformation (peat expands/contracts with gas increases/decreases) at various depths show a similar pattern, with relatively little variation observed at the wooded heath site, whereas the pools site shows variations that increase with proximity to the underlying esker crest. In addition, below 1 m depth the pools site shows higher temperature, higher pH, higher methane content, and enrichment in various nutrients when compared to wooded heath site. The geochemical conditions observed at the pools site are more favorable for microbial respiration (and hence gas production). Indeed, limited methane flux data suggest typically larger fluxes at the pools site.

Overall, the results suggest the esker deposit below the pools site likely generates a hydraulic gradient that brings with it nutrients, higher temperatures, and more alkaline waters that act to enhance biogenic gas production at this site. The absence of continuous layers at the pools site allows ebullition to occur more readily when compared to the wooded heath site, where gas may become trapped under such layers to form large pockets of gas.

1.3.3 Estimation of peat gas bubble size from GPR

The third and final paper, submitted to *Water Resources Research* in 2016, addresses the third research objective outlined above, and forms the foundation for a methodology to gain information about the size of individual gas bubble clusters – information potentially crucial in determining when ebullition will occur in peat, particularly in areas like the wooded heath site where gas is believe to remain trapped

until bubble buoyancy overcomes the force from above. The technique relates changes in the frequency content of GPR signals (after basic processing) to changes in bubble radius through established models of frequency dependent attenuation and scattering. Two laboratory datasets are investigated using the technique. The first dataset consists of transmission GPR measurements taken at nine positions for a period of several weeks across a peat monolith. The results show increases in overall gas content at all monitoring positions, while bubble radius shows a pattern of mostly decreasing in size in the upper layers and mostly increasing in size in the lower layers, with the average bubble radius ranging from 0.002 m to less than 0.01 m. The second experiment is of similar design to the first except that GPR data were collected in reflection mode and that bubble sizes on the side of the peat monolith tank were observed. Somewhat larger bubbles are estimated than in the first experiment (with a maximum radius of about 0.02 m), but show a similar pattern of larger bubbles resulting in deeper areas of the monolith. The size of bubbles observed on the side of the tank are consistently smaller than those estimated by the GPR estimation approach. The bubble size estimation approach is finally applied to a dataset from a borehole GPR field study at the pools site in Caribou Bog, suggesting an average bubble radius of about 0.04 m and possibly as large as 0.1 m at an interface where a change in decomposition was noted during coring. The highlight to the approach is that it may provide evidence of bubble size in peat – information not readily available by any other means. Bubble size determines buoyancy and therefore may affect the amount of methane that reaches the atmosphere during ebullition (due to larger bubbles passing more readily through the oxic zone and avoiding consumption by methanotrophs [*Ramirez et al.*, 2016]), and be a controlling factor in triggering ebullition

itself (due to the greater ability of large bubbles to overcome confining forces [*Tokida et al.*, 2007; *Comas et al., 2011a*; *Chen and Slater, 2015*]). Additionally, the approach could theoretically be used on existing and future GPR datasets. Limitations include that the bubble size estimation model assumes spherical bubbles, does not account for redirected energy from multiple scattering events, and provides only an average bubble size (i.e., many bubbles, possibly of varying size, are within the sampling volume of a GPR pulse).

1.3.4 General findings

These studies suggest that large volumes of biogenic gas are stored in peat, particularly below confining layers consisting of peat fabric and/or poorly decomposed material. Coring data suggest these confining layers are on the order of several cm thickness. At a site with pools on the surface and underlain by a permeable esker deposit, gas dynamics appear to intensify in the deep peat, as evidenced by higher levels of decomposition, larger peat surface deformations, and larger resistivity variations observed when compared to a site where the esker deposit is not present in the sampling area. Furthermore, analysis of the frequency content of GPR traces from this same site suggest that gas bubbles are 0.04 m in radius or larger. These findings highlight the usefulness of geophysical tools for studying biogenic gas dynamics in peatlands.

1.3.5 Broad implications

This work provides a unique view of biogenic gas dynamics at cm to m scale spatial resolution over a 3D volume at hourly temporal resolution and indicates that these processes exhibit significant variability at this scale. Previous work does not include information at these scales and at that resolution. In the broad context, this degree of variability of biogenic gas dynamics may need to be considered in global models that

incorporate peatland gas dynamics and stresses the importance of information about the underlying peat structure and hydrogeology. Further, the apparent influence of the esker deposit in regulating biogenic gas dynamics in Caribou Bog indicates that the age and development of peat within the formational process of peatlands as a whole may be key factors in understanding gas dynamics at different peatlands across the world.

The tools and techniques explored and developed in this thesis have broad applicability to future studies of gas dynamics in peatlands. The use of autonomous ERI would be a useful addition to future studies for observing qualitative changes in gas content and to support other datasets. Once set up, an autonomous ERI system can be operated entirely remotely, and sampling frequency, the measurement scheme, and other data collection parameters can be monitored and modified if required. Given a sufficient power supply (in this study a 400W solar array and a battery bank were used), such a system could run for several years. The GPR bubble size estimation technique is unique in that it provides information on bubble size *in situ*, without disturbing the peat. Additionally, the procedure could be applied to existing and future datasets to better constrain ebullition models, where the size of bubbles may influence when ebullition occurs and the degree of oxidation when it is released to the atmosphere.

Chapter 2: Free phase gas processes in a northern peatland inferred from autonomous field-scale resistivity imaging[1]

Abstract

The mechanisms that control free phase gas (FPG) dynamics within peatlands, and therefore estimates of past, present, and future gas fluxes to the atmosphere remain unclear. Electrical resistivity imaging (ERI) is capable of autonomously collecting three dimensional data on the cm to tens of meter scale and thus provides a unique opportunity to observe FPG dynamics *in situ*. We collected 127 3D ERI datasets as well as water level, soil temperature, atmospheric pressure, and limited methane flux data at a site in a northern peatland over the period July-August, 2013 to improve the understanding of mechanisms controlling gas releases at a hitherto uncaptured field scale. Our results show the ability of ERI to image the spatial distribution of gas accumulation and infer dynamics of gas migration through the peat column at high (i.e., hourly) temporal resolution. Furthermore, the method provides insights into the role of certain mechanisms previously associated with the triggering of FPG releases such as drops in atmospheric pressure. During these events, buoyancy-driven gas release primarily occurs in shallow peat as proposed by the 'shallow peat model.' Releases from the deeper peat are impeded by confining layers, and we observed a large loss of FPG in deep peat that may likely represent a rupture event where accumulated FPG escaped the confining layer as suggested by the 'deep peat model'. Negative linear correlations between water table elevation and resistivity result from hydrostatic pressure regulating bubble volume, although these variations did not appear to trigger FPG transfer or release.

[1]This chapter published as: Terry, N., L. Slater, X. Comas, A. S. Reeve, K. V. R. Schäfer, and Z. Yu (2016), Free phase gas processes in a northern peatland inferred from autonomous field-scale resistivity imaging, *Water Resour. Res.*, 52, 2996–3018, doi:10.1002/2015WR018111.

2.1 Introduction

Methane (CH_4) is the third most abundant greenhouse gas in the atmosphere but has 34 times the heat trapping potential of carbon dioxide [*Forster et al.*, 2007]. Wetlands, and peatlands in particular, are major sources of CH_4 and account for approximately 22% of the global CH_4 flux to the atmosphere [*Stocker et al.*, 2013]. In addition, global warming is anticipated to further stimulate CH_4 production from these ecosystems, creating a positive feedback loop [*Bridgham et al.*, 2013].

Despite the known significance of wetlands with respect to climate change, the 2013 Intergovernmental Panel on Climate Change report [*Stocker et al.*, 2013] states that confidence in modeled CH_4 flux from wetlands remains low, owing to a lack of observational datasets for calibration of process-based models (i.e., [*Hodson et al.*, 2011; *Ringeval et al.*, 2011; *Spahni et al.*, 2011]). The spatial and temporal variability in CH_4 production, transport, and release within these wetlands also remains poorly constrained [*Papa et al.*, 2010].

CH_4 is produced in peatlands primarily by microbes and is released to the atmosphere through diffusion, transport through vascular plants, and/or rapid ebullition (bubbling). The overall CH_4 produced by these microbes and the subsequent release to the atmosphere is controlled by a number of biological and environmental factors. A considerable body of research has been dedicated to linking these factors to CH_4 flux in order to understand the current and future response of peatlands to climate change. *Walter and Heimann* [2000] developed a process-based model for estimating methane emissions from wetlands that includes diffusion, transport, and ebullition mechanisms. However, this model lacks a bubble dynamics component. In order to better understand

the relationship between bubble dynamics and ebullition, there is a need for observational data sets at high spatiotemporal resolution.

Direct chamber-based measurements of CH_4 fluxes typically have a small (< 1 m^2) footprint that may not be suitable for upscaling, whereas eddy covariance systems integrate over a much larger area but may not have the required resolution to capture short-term ebullition events, which can episodically release a large amount of CH_4 over a short time period [*Rosenberry et al.*, 2006]. In a recent study, *Gålfalk* et al. [2015] developed an optimized infrared hyperspectral imaging system capable of photographing CH_4 at the sub m^2 scale that offers great promise to bridge scale differences between chamber measurements and eddy covariance systems. In a laboratory study of a peat monolith, *Yu et al.* [2014] recorded 926 ebullition events lasting minutes to hours, which released CH_4 at a rate of 212.2 ± 44.3 mg m^{-2} d^{-1} during a single event. *Glaser et al.* [2004], relying on peat deformation and hydraulic head measurements, calculated a loss of 130 g m^{-2} of CH_4 over 3 individual ebullition events believed to originate deep (>4 m) in the peat profile during the late summer from the Glacial Lake Agassiz peatlands (GLAP) in Northern Minnesota. This result, when averaged over an entire year, is an order of magnitude larger than the diffusive rate based on seasonal chamber measurements from the same site [*Chasar*, 2002].

Such results and the observations of others [*Chanton et al.*, 1995; *Chasar*, 2002; *Chasar et al.*, 2000a, 2000b; *Crill et al.*, 1988, 1992; *Romanowicz et al.*, 1993, 1995; *Rosenberry et al.*, 2003; *Siegel et al.*, 2001] formed the basis for the so-called 'deep peat model' [*Glaser et al.*, 2004]. This model stresses extensive CH_4 production in 'hot spots' within the most anaerobic deep peat (> 3 m) [*Siegel et al.*, 2001] due to readily available

labile C substrate transported from above. When equilibrium is disrupted, such as by changes in atmospheric pressure [*Comas et al.*, 2011a], gas migrates upward due to increased buoyancy. Gas bubbles that are trapped under confining layers are episodically released in large concentrations when confining forces are exceeded by buoyancy forces associated with bubble expansion during abrupt drops in atmospheric pressure [*Rosenberry et al.*, 2003; *Glaser et al.*, 2004]. However, increases in atmospheric pressure have also been correlated with increased fluxes in deep parts of the peat column in northern systems and in shallow peat along subtropical systems (*Comas et al.*, 2011a, *Comas and Wright*, 2014).

The 'shallow peat model' proposed by *Coulthard et al.* [2009] instead suggests that most biogenic gas production, and particularly CH_4, likely occurs in the shallow (< 1 m) anaerobic zone, driven by higher summer temperatures [*Dunfield et al.*, 1993], more abundant labile C [*Moore and Dalva*, 1997], and trapped bubbles acting as nucleation sites for CH_4 during water table rise [*Beckwith and Baird*, 2001]. This model holds that FPG buildup and episodic ebullition are common in the shallow peat, and may contribute more to FPG flux than less frequent ebullition events from deep layers. *Coulthard et al.* [2009] base their model on the large body of literature on methane production and bubble formation in shallow peat [e.g., *Baird et al., 2004*; *Beckwith and Baird*, 2001; *Christensen et al.*, 2003; *Comas and Slater*, 2007; *Kellner et al., 2006*; *Laing et al.*,2008; *Ström et al.*, 2005; *Tokida et al.*, 2005a]. However they stress that improved direct observation of deep FPG dynamics is required to confirm the relative importance of deep peat to ebullition.

Geophysical methods provide a unique opportunity to study three-dimensional FPG dynamics below the peat surface at spatial scales ranging from centimeters to tens of meters. Measurements can be made non-invasively, without disturbing the internal structure of the peat and therefore altering the naturally existing gas dynamics. In contrast, direct measurements made by installing wells or inserting probes into peat can immediately create a vent for gas to escape and potentially leave a preferential flow pathway for gas to migrate along thereafter [*Rosenberry et al.*, 2006]. Ground penetrating radar (GPR) has been extensively employed as an indirect and minimally invasive methodology for determining temporal variations in FPG content in peatlands [*Comas et al.*, 2005, 2011a; *Parsekian et al.*, 2010, 2011; *Strack and Mierau*, 2010] at both laboratory and field scales. Here, 'minimally invasive' implies that although there is some disturbance to the peat surface from walking over it with antennas, no disturbance of the internal structure of the peat is necessary. GPR wave velocities are very sensitive to moisture content, and can hence be used to qualitatively and semi-quantitatively assess changes in FPG content [*Comas et al.*, 2008]. As previously mentioned, the minimally invasive nature of GPR offers a critical advantage when seeking to avoid disruption of the natural FPG dynamics within peatlands. However, GPR is not ideal as a long term monitoring tool as it is not readily automated, particularly at the field scale.

Electrical resistivity imaging (ERI) is another minimally invasive geophysical technique that potentially can be used to indirectly monitor FPG in peat, as the degree of saturation (and therefore amount of gas) influences the bulk resistivity of the peat. Unlike GPR, which relies on field operators to acquire subsequent datasets, ERI can be completely automated to collect time-lapse 3D data [e.g., *Daily et al.*, 2004; *Singha et al.*,

2014 for review]. Two laboratory studies have previously highlighted the potential of ERI for assessing FPG dynamics in peat. *Slater et al.* [2007] demonstrated the utility of electrical imaging to monitor time-lapse changes in gas content in a single laboratory peat monolith and *Kettridge et al.* [2011] extended this approach to study biogenic gas dynamics in several peat cores reflecting different peat types and meteorological conditions. Both these laboratory studies concluded that a quantitative assessment of FPG content and/or flux is unrealistic using ERI, but that this technique is effective at capturing changes in gas content in peat and for inferring the mechanisms driving these changes. However, a field-scale application of this approach has not yet been undertaken.

In this study we report on the first attempt to apply time-lapse ERI to monitor biogenic gas dynamics at the field scale. Time-lapse ERI datasets are compared with a shorter duration set of direct high temporal resolution measurements of CH_4 flux to further evaluate the driving forces behind FPG dynamics and ebullition. We show how ERI datasets provide valuable insights into the processes regulating CH_4 bubble transport and ebullition at a unique spatial scale hitherto unachieved with other investigation techniques. Our results give large-scale information on the role of atmospheric pressure and water levels variations on gas release and demonstrate that major episodic ebullition events associated with large pressure drops are clearly associated with changes in gas content throughout the peat profile. These results also offer clear insights into the relative importance of shallow versus deep sources of CH_4 releases via ebullition release regulated by atmospheric pressure and water level. Our analysis supports the shallow peat model in that the release of gas from the upper meter of peat appears to be more

common than below 1 m. However, ERI data from this study also support the deep peat model as we witnessed one large ebullition event originating from deep peat below a woody layer. This work has implications for better understanding how climate induced changes in pressure, rainfall, and temperature may increase greenhouse gas release from peat soils.

2.2 Background

2.2.1 Electrical resistivity imaging (ERI)

ERI surveys involve driving a known current (normally using a modified low frequency square wave) between two electrodes and measuring the potential difference between other pairs of electrodes at multiple locations. Raw ERI data thus consist of transfer resistances, which are simply the potential differences divided by the injected current (Ohm's law). In a homogenous medium, resistivity can be computed analytically using the positions of the electrodes and the transfer resistance. Heterogeneous resistivity distributions require inverse methods to arrive at a solution (see *Binley and Kemna* [2005] for further details). Historically ERI was primarily used for geologic characterization and natural resource exploration, but application of ERI to study near surface dynamic processes via time-lapse imaging is now well established (see *Singha et al.* [2014] for a recent review). Electrical resistivity has been used as a proxy for time-varying parameters of interest including moisture content [*Binley et al.*, 2002], salinity [*Hayley et al.*, 2009], and temperature [*Krautblatter and Hauck*, 2007]. Well-established petrophysical relations link resistivity to certain physical and chemical properties of the pore space. As we will discuss, however, it is often impossible or impractical to establish such a link under field conditions.

The measured bulk resistivity (1/conductivity) of a metal-free soil consists of the combined effects of electrolytic conduction (ions in the solution filling the interconnected pore space) and surface conduction (ions in the electrical double layer at the walls of the connected pores) pathways, which add in parallel. Ignoring surface conduction, the resistivity of a soil (ρ_{soil}) can be modeled using Archie's law for unsaturated sediments,

$$\frac{1}{\rho_{soil}} = \sigma_{el} = (\phi_{int})^m S^n \sigma_w, \quad (2.1)$$

where σ_{el} is the electrolytic conduction pathway representing the flow of current through ions in the pore fluid, ϕ_{int} is the interconnected porosity, S is saturation, σ_w is the conductivity of the pore fluid, m is the 'cementation' factor which depends on pore structure and tortuosity, and n is the saturation exponent describing the distribution of air in pore spaces and is dependent on soil type.

Archie's law may be poorly parameterized for organic soils, and alternative formulations linking resistivity to the soil property of interest may be needed. Archie's Law assumes (1) no surface conduction, which will certainly be violated in organic soils of large surface area saturated with pore fluids of low ionic concentrations as is typical of ombrotrophic bogs, and (2) a non-conducting soil matrix, which may also be violated in organic sediments as there is evidence for electronic conduction occurring across organic particles themselves [*Comas and Slater*, 2004]. In addition, peat soils exhibit a strong dependence of ϕ_{int} on σ_w [*Comas and Slater*, 2004] likely due to pore dilation resulting from the flocculation of organic acids on macropore surfaces [*Ours et al.*, 1997]. *Comas and Slater* [2004] found an empirical power-law relationship linking ρ_{soil} to surface conductivity and σ_w.

Slater et al. [2007] used a time-lapse inversion approach to highlight changes in resistivity that they associated with changes in S due to biogenic gas production, gas transport and subsequent release from peat soils. While resistivity values were corrected for changes in σ_w, *Slater et al.* [2007] assumed negligible surface conduction effects and insignificant temporal changes in the Archie exponents m and n to use the following relationship,

$$S = \frac{\theta}{\phi} = \frac{(\phi - FPG)}{\phi} = \left[\frac{\rho_{[unsat]}}{\rho_{[sat]}}\right]^{-1/n}, \tag{2.2}$$

where θ is the water content, ϕ is the total porosity, FPG is free phase gas content, and $\rho_{[unsat]}$ and $\rho_{[sat]}$ are the resistivity of the soil in unsaturated and completely saturated conditions, respectively. Time-lapse resistivity was thus related to relative changes in FPG content through comparison of their ratios,

$$\rho_{rat} = \frac{\rho_{soil,t}}{\rho_{soil,0}} = \left[\frac{\phi_t - FPG_t}{\phi_0 - FPG_0}\right]^{-n}, \tag{2.3}$$

where ρ_{rat} is referred to as the ratio resistivity, $\rho_{soil,0}$, ϕ_0, FPG_0, $\rho_{soil,t}$, ϕ_t and FPG_t are the resistivity, porosity, and free phase gas content of the soil at time 0 and t, respectively. In the *Slater et al.* [2007] study, porosity variations were monitored through elevation rod measurements, while n and FPG_0 values were estimated from a parallel block experiment [*Comas and Slater*, 2007].

Controlled laboratory conditions allowed quantification of FPG in the study of *Slater et al.* [2007], but it is likely impractical to establish any such quantitative link between resistivity and gas content in the field. Application of equation 2.3 at the field-scale requires spatiotemporal information on the variation of porosity, the saturation exponent,

and an initial estimate of the free phase gas content. Estimation of FPG_0 through evaluation of equation 2.1 in turn requires information on interconnected porosity, the cementation exponent, and pore water conductivity. An assumption that surface conduction effects are negligible and that the peat matrix acts as a pure insulator is also needed. Given these limitations, we restrict our analysis to ratio resistivity, and abandon the idea of quantitatively predicting gas content/changes from the images. *Johnson et al.* [2012] stress the utility of geophysics, and ERI in particular, for capturing the inherent hydrogeological responses within geophysical data without the need to explicitly reconstruct hydrogeological properties from the geophysical data. Following their lead, we use ERI to capture spatiotemporal dynamics of gas releases as a function of environmental forcing without attempting to estimate physical properties given the likely futility of the approach in such an electrically complex porous medium. We recognize that peat is a highly compressible material whose physical properties may vary through time and that we cannot necessarily attribute all changes in ERI data to changes in gas content. However, we assume these changes are negligible in our case when considering the scale difference between our gas content estimates, which are based on the entire thickness of the peat column (over 6 m thick within our study area), and typical changes in vertical deformation due to matrix contraction and expansion (i.e., only as high as 0.02-0.03 m for shallow portions of the column as recorded from other studies at the same peatland unit [*Comas et al.*, 2011a]).

2.2.2 Time-lapse inversion of ERI data

Inverse methods are needed to estimate the distribution of model parameters from boundary observations. This problem is ill-posed for ERI data where many resistivity

distributions may satisfy the data. We used R3t (Andrew Binley, Lancaster University) to invert the ERI data. In R3t, forward data are numerically simulated by evaluating the 3D Poisson equation using the finite element method. For inversion, R3t iteratively minimizes an objective function of the general form,

$$\Psi_{total} = \Psi_d + \alpha\Psi_m, \tag{2.4}$$

where Ψ_d is the data misfit, Ψ_m is the model misfit, and α is a regularization term penalizing departure from a starting model. At each iteration, model parameters (resistivity of mesh elements) are updated through a Gauss-Newton approach, with α optimized through a line search at each Gauss-Newton iteration. Convergence is gauged by the root mean squared error of the data misfit normalized by a user-supplied estimate of the data error. It is therefore critical to supply quantitative estimates of the errors in the field data to the inversion routine to avoid over or under fitting the data which can result in image artifacts unrelated to the subsurface resistivity structure [*LaBrecque et al.*, 1996]. For more information on the theory of inverse methods for ERI, see *Binley and Kemna* [2005].

Although it is possible to simply compare resistivity images post inversion through division or subtraction, time-lapse ERI data can be 'differenced' prior to inversion to enhance the sensitivity of the inverse procedure to changes in the data [*Labrecque and Yang*, 2001]. Changes in resistivity are highlighted through this approach by modification of data input into the inverse routine,

$$\mathbf{d}_{diff,i} = \mathbf{d}_i + \mathbf{d}_f - \mathbf{d}_0, \tag{2.5}$$

where $\mathbf{d}_{diff,i}$ are the differenced resistance data, $\mathbf{d}_i$ are the observed data, $\mathbf{d}_0$ are the resistance data from a reference dataset in time, and $\mathbf{d}_f$ are theoretical resistances for a forward model for that reference dataset. Here, the subscript i refers to the time index of each dataset. Following standard rules of error propagation, the total errors $\boldsymbol{\varepsilon}_i$ required to weight each measurement in the inversion appropriately are then,

$$\boldsymbol{\varepsilon}_{diff,i} = \sqrt{\boldsymbol{\varepsilon}_i{}^2 + \boldsymbol{\varepsilon}_f{}^2 + \boldsymbol{\varepsilon}_0{}^2}, \tag{2.6}$$

where $\boldsymbol{\varepsilon}_{diff,i}$ are the errors put into the difference inversion, $\boldsymbol{\varepsilon}_i$ are observed data errors, $\boldsymbol{\varepsilon}_f$ are the forward modeling errors (calculated through forward modeling of a 100 ohm m homogeneous medium), and $\boldsymbol{\varepsilon}_0$ are the errors for the background dataset. The absolute percent differences between the data computed in R3t for a homogenous medium and the analytically calculated transfer resistances for the same homogeneous medium are multiplied by $\mathbf{d}_{diff,i}$ and used as $\boldsymbol{\varepsilon}_f$.

2.2.3 Analysis of ERI time-series

Comprehensively representing the information content in large time-lapse ERI datasets can be challenging given that it is impractical and often not informative to present a large number of images (in this study there are 127 raw datasets). *Singha et al.* [2014] outline several strategies for analyzing time-series ERI data. *Johnson et al.* [2012] investigated correlations, cross correlations, and time lag to maximum correlation between the resistivity time series at individual voxels (different spaces in the modeled domain) and environmental variables to derive hydrologic information on controls on groundwater-surface water exchange. We adopt a similar approach to help draw out information on the environmental parameters driving variation in FPG content in peat.

Linear correlations can be calculated using Pearson's correlation coefficient, r.

For convenience of discussion, we employ the following nomenclature for describing the strength of r: $0.0 \leq |r| < 0.1$ = none, $0.1 \leq |r| < 0.4$ = weak, $0.4 \leq |r| < 0.7$ = moderate, $0.7 \leq |r| < 1.0$ = strong.

2.3 Methodology

2.3.1 Study site: Caribou Bog, Maine

Caribou bog is a 2200 ha multi-unit ombrotrophic peatland in central Maine. The central unit of the bog wherein this study was performed lies between Pushaw Lake and the Penobscot River, and features a well-developed pattern of pools and raised bog complexes [*Davis and Anderson*, 1999]. Using a combination of direct measurements and indirect geophysical measurements, *Slater and Reeve* [2002] and *Comas et al.* [2011a] identified the peat layer of the bog as having a variable thickness of less than 12 m in most locations, overlying a discontinuous layer of organic-rich lake sediment exceeding 5 m in certain areas [*Comas et al.*, 2004]. The underlying mineral basement consists of the Presumpscot Formation; a glacio-marine silt-clay layer overlying glacial till resulting from erosion of bedrock during the Pleistocene [*Bloom*, 1963]. The bedrock consists of metamorphosed middle Ordovician to middle Devonian material [*Osberg et al.*, 1985].

This study focuses on an area within the Central unit of Caribou bog vegetated primarily with small-leaved *Sphagna* including Sphagnum capillifolium (Ehrh.) Hedw. and *Sphagnum fuscum* (Schimp.) Klinggr.. This particular site was chosen as part of a larger research project investigating FPG dynamics as a function of land cover type,

including: pools, shrub, and wooded heath (this study). Overlying the *Sphagna* are several low ericaceous shrubs, mainly *Chamaedaphne calyculata* (L.) Moench. A few isolated tall evergreen trees are also present outside the footprint of the ERI survey.

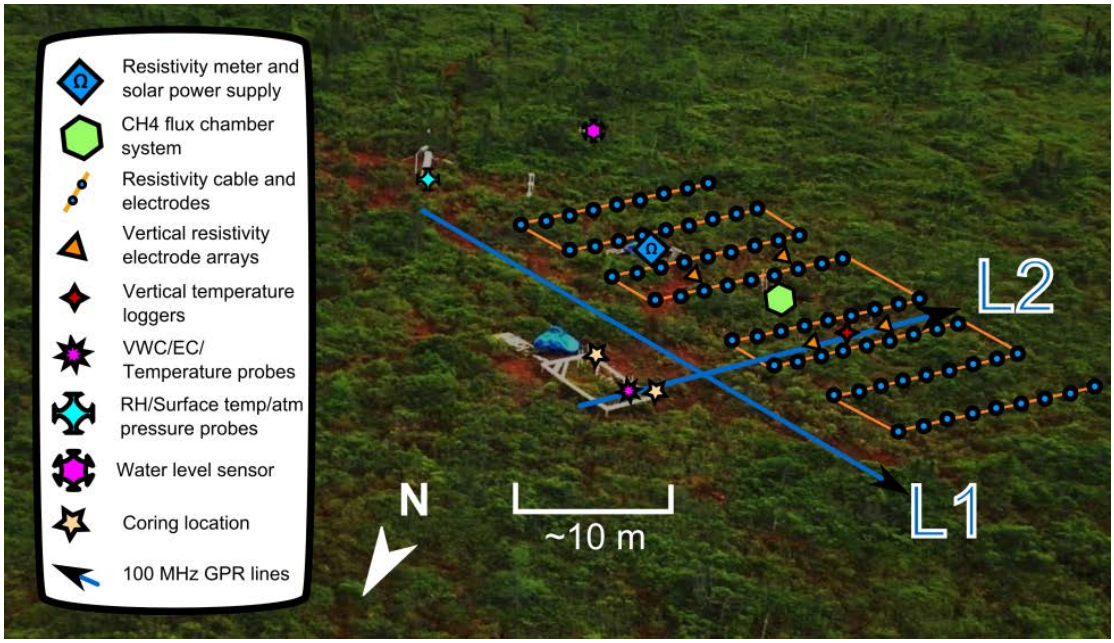

Figure 2.1 –Schematic of the ERI resistivity array and relevant sensors overlain on an oblique aerial image. GPR L2 corresponds to figure 2.3e. Image courtesy of William Wright, 2013.

2.3.2 Field implementation of ERI

A schematic of the ERI monitoring array and associated sensors is shown in Figure 2.1, and Table 2.1 is a summary of these data along with estimated sampling volume, spatiotemporal resolution, and accuracy/precision. Automated ERI data collection used an IRIS Syscal Pro Switch resistivity instrument with two solar circuits to power a transmitter and a receiver/field computer. Complete datasets were collected from July 4, 2013 to August 28, 2013 for a total of 127 time-lapse datasets with a minimum time step

of 2 hours and an average of 10 hours between them. The system employed 72 stainless steel electrodes that covered a 28 by 10 meter area. Electrodes were arranged in eight lines with 1.25 m within line spacing and variable spacing (3.5 to 5 m) between lines to accommodate other instrumentation. The measurement scheme consisted of a non-standard dipole-dipole array, with an intra-dipole (*a*) spacing of 1 and 8 electrodes, and an inter-dipole spacing (*na*) spacing from 1 to 68 electrodes for a total of 2,184 unique measurements at each data collection time. Given the total size of the ERI array (28 m by 10 m), the maximum distance between dipole centers is 27.8 m. Using the common convention of estimating pseudodepth for dipole-dipole arrays by the intersection of 45 degree lines drawn down from the dipole centers, this equates to an investigation depth of 13.9 m. This depth is likely quite exaggerated. Therefore, we performed forward and inverse modeling experiments to confirm the array is sensitive to relatively small changes in resistivity throughout the entire peat profile (down to 6.4 m depth at this site).

Full reciprocal measurements (current and potential electrodes switched) for each dataset were also gathered for error analysis purposes. The reciprocity principle states that an electric field will remain the same if current and potential measurement locations are reversed. To optimize current injections and data collection speed, several 'dummy' measurements were added. Thus, 4,984 data were collected at each time step, including a full set of reciprocal measurements. Each dataset took approximately 1 hour and 15 minutes to collect using 3 stacks and a 500 ms time delay between current injections. Voltage injection was set at 100 V, providing a good compromise between signal to noise ratio and power consumption.

Four vertical electrode arrays (VEAs) each with 16 electrodes spanning from the surface to the mineral soil were installed with electrodes spaced 0.3 m apart at different locations within the resistivity array (Fig. 2.1). Data were collected in a Wenner configuration using a Campus Geopulse resistivity instrument once daily during most of July 2013, but were not gathered during the August monitoring period. These data were primarily collected to add confidence to our 3D ERI inversion results. Given the decaying sensitivity of ERI inversions away from the electrodes, the VEAs provide reassurance (in addition to that from resolution matrix and depth of investigation statistics) that measurements in low sensitivity areas (i.e., the deep peat) are reliable.

2.3.3 Supporting environmental and geophysical data

Environmental sensors installed included 9 HOBO pendant soil temperature loggers spanning from just below the peat surface to 6.4 m depth at 0.8 m intervals (primarily intended to correct resistivity inverse results for temperature variations throughout the peat profile; data logged every 15 minutes), a Solinst LevelLogger Junior 3001 water level sensor (primarily for observing the link between resistivity, water level and gas dynamics; collected at 2 minute intervals), and a relative humidity/air temperature/atmospheric pressure sensor (built into a Hydroinnova Cosmic-ray moisture probe; collected at 1 hour intervals). Water levels were compensated for atmospheric pressure variations using a sensor built in to the logger. The relative humidity/air temperature/atmospheric pressure information was mainly used to perform corrections to methane flux data (described later in this section), as well as to study the relationship between atmospheric pressure and gas dynamics. The locations of the environmental sensors are shown in Fig. 2.1. Daily rainfall data were taken from the local weather

underground station in Bangor, ME (KMEBANGO3). Four Decagon 5TE probes were installed at various depths to monitor bulk electrical conductivity (1 minute data collection interval). These probes also recorded dielectric permittivity and temperature, which in addition to the bulk electrical conductivity, were used to estimate changes in pore water conductivity (described below). The layout of these sensors is shown in Figure 2.1, and a summary of the types of data collected is shown in Table 1.

A key assumption of our resistivity monitoring experiment is that the effect of changing pore water conductivity σ_w remains small compared to the effect of changing FPG content. Using the conversion presented in the 5TE manual and the relationships described by *Hillhorst* [2000], we converted bulk conductivity, bulk dielectric permittivity, and temperature to σ_w at 0.2, 1.0, 3.0 and 4.5 m depth. We recognize that this conversion factor is based on assumptions that are likely violated for organic peat soils and therefore focus our interpretation on the relative variation at each probe.

GPR data were collected along two profiles (shown in Fig. 2.1b) using a MALA ProEx system and 100 MHz unshielded antennas. The data underwent basic processing including (1) dewow, (2) time-zero adjustment, (3) exponential gain, (4) trimming of the profiles to include only the data near the core and resistivity array. For time to depth conversion, a common midpoint survey and subsequent analysis revealed an average EM velocity of 0.034 m/ns, within 0.001 m/ns of values previously reported for Caribou Bog (for example by *Comas et al.* [2005, 2011a]). Limited CH_4 flux data were recorded during the month of July by a dynamic flux chamber system located in the center of the ERI array (location shown in Figure 2.1b). The flux chamber system consists of a modified form of the setup employed by *Mastepanov and Christensen* [2009] and similar

to the laboratory configuration of *Yu et al.*, [2014] whereby an open path fast CH_4 analyzer (FMA, LI-7700, LI-COR Biosciences, Lincoln, NE, USA) is enclosed in a plastic chamber to continuously monitor CH_4 concentrations. The setup is equipped with a pump to circulate air through the system. Due to power limitations at the remote fieldsite, the CH_4 flux data were only acquired over five monitoring periods lasting from 1 to 3 days each at high (1 second) temporal resolution. Raw measurements were adjusted for variations in pressure, temperature, and relative humidity according to Webb-Pearman-Leuning (WPL) [*Webb et al.*, 1980] and spectroscopic corrections [*McDermitt et al.*, 2011] before converting to CH_4 flux.

Table 2.1. Summary of data collected

Method (type of data collected) /instrument used	Sampling volume/Spatial resolution	Temporal resolution (highest) /time period collected	Instrument accuracy/precision
ERI (resistance) /IRIS SyscalPro	>1000 m^3 sampling volume/ < 1 m^3 spatial resolution	2 hrs /July and August 2013	±0.2% accuracy ±1 μV precision
VEA (resistance) /Campus Geopulse Tigre	>1 m^3 sampling volume/ < 1 m^3 spatial resolution	24 hrs /July 2013	~ ±1% accuracy
GPR (EM wave travel times and amplitudes) /MALA ProEx	>100 m^3 sampling volume/ < 1 m^3 spatial resolution	Single measurement /July 3 2013	~ ±0.001 m/ns precision
Dynamic flux chamber (CH_4 concentration) /Licor LI-7700	< 1 m^2/point measurement	1 s /select times during July 2013	±5 ppb accuracy
Temperature logging /HOBO pendants	~1 cm^3/point measurement	15 min /July and August 2013	±0.53 ºC accuracy ±0.14 ºC precision
Electrical conductivity logging /Decagon 5TE	~10 cm^3/point measurement	1 min /July and August 2013	±10% (EC accuracy) /±3% (VWC accuracy)
Pressure transducer (water level) /Solinst LevelLogger Junior 3001	~1 cm/point measurement	2 min /July August 2013	±1 cm accuracy
Atmospheric pressure/surface temperature/relative humidity logging /Hydroinnova cosmic-ray probe	~1 cm^3/point measurement	1 hrs /July and August 2013	±0.1 hPa (atmospheric pressure accuracy) ±1 ºC (temperature accuracy) ±3% (relative humidity accuracy)

2.3.4 Initial subsurface characterization

Initial characterization of the site was based on two cores (locations shown in Fig. 2.1). A von Post humification test was performed for the western core only (Fig. 2.2a). The von Post humification scale is a set of guidelines for identifying the relative degree of peat composition in the field (1 being the least decomposed and 10 being completely decomposed).

Both cores revealed an approximately 6.4 m thick peat layer overlying a 0.4 m transition zone of lake sediment (pictured in Figure 2.2d) becoming pure glaciomarine clay mineral soil at 6.8 m depth. Layers of poorly decomposed wood debris were identified at approximately 1.9, 3.45, and 3.75 m depth in the western core and at 2.3 and 3.45 m depth in the eastern core as shown in Figure 2.2c. The woody layers correspond to distinct decreases in von Post humification (Figure 2.2a). In addition, several ~1 mm dark layers, likely ash or possibly layers of enhanced peat decomposition, were visible between 1 and 2 meters depth in both cores (Figure 2.2b).

Data from one of the GPR lines (shown as L2 in Fig. 2.1) collected at the site are displayed in Figure 2.2e and show distinct reflection events from the mineral sediment and numerous semi-continuous reflectors in between, likely associated with woody debris. This GPR radargram, combined with that obtained on a second line (not shown here for brevity), confirm that the mineral soil is mostly flat but grades slightly downward toward the south (0.4 % and 0.5 % gradient estimated toward the southeast and southwest in lines 1 and 2, respectively). Furthermore, it confirms the lateral continuity of some of the stratigraphic attributes described above (i.e., woody layers at 1.9 and 3.75 m depth as well as the peat-mineral soil interface at 6.4 m).

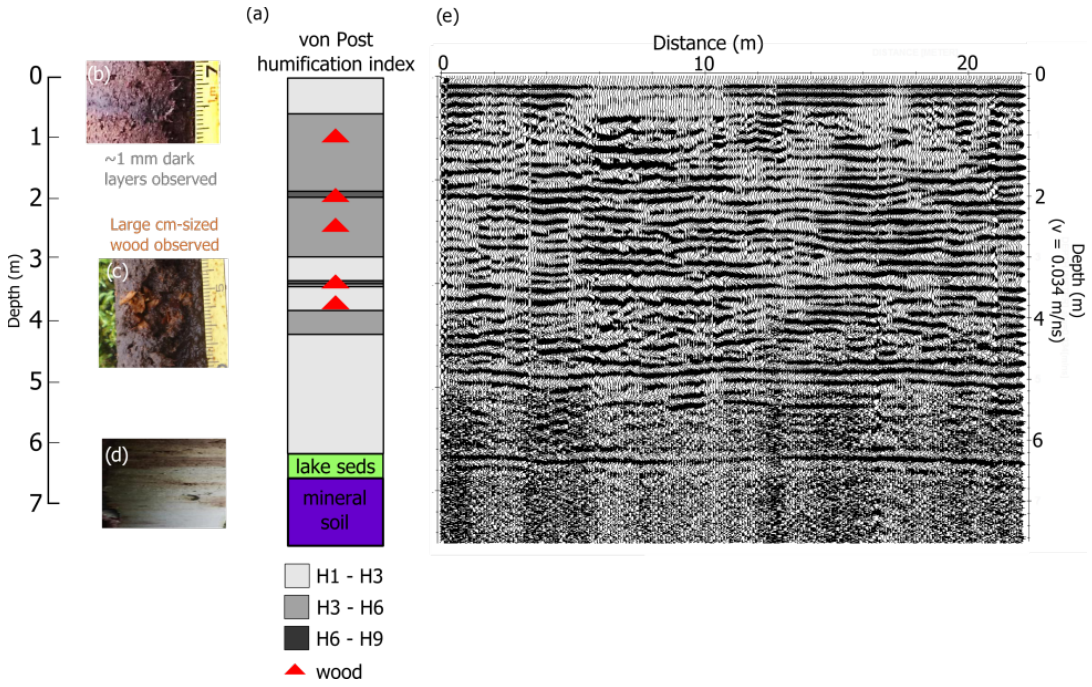

Figure 2.2 – Preliminary characterization of the Caribou Bog site: (a) von Post humification index and select features along the 7.0 m core identified in the field; (b) photograph of example dark layer; (c) photograph of example woody debris observed; (d) photograph of the transition from peat to the lake sediment at 6.4 m; (e) ground penetrating radar (GPR) line taken nearby which shows the peat/mineral soil interface as a clear reflector at 6.4 m. All photographs courtesy of Xavier Comas, 2013.

2.3.5 ERI data processing and time series analysis

2.3.5.1 Data filtering

For quality control purposes, all measurements from the time series with (1) > 25 % reciprocal error, (2) a negative resistivity, or (3) an applied current or measured voltage of less than 1 millivolt or 1 milliAmp were removed (performed after data collection; there was no field filtering of data). Reciprocal error percentage was calculated as the normal measurement minus the reciprocal measurement, all divided by the normal measurement. In the raw data, normal-reciprocal errors were highly left-skewed and

averaged 6% due primarily to a relatively small number of measurements (~3%) possessing large reciprocal errors. The choice of a 25% reciprocal error and 1mV cutoff was based on the relatively low electrical noise at the field site in Caribou Bog.

To make each dataset comparable to the next for time-lapse inversion, measurements failing to meet these conditions within a particular dataset were removed from all datasets in the time series. Under these criteria, each dataset retained 3338 of the 4984 original measurements (67 %). In other words, there were 1,669 normal measurements and 1,669 reciprocal measurements for each time series dataset after the filtering. The remaining data exhibited a mean reciprocal error of 0.46%. Within each dataset, the averages of the normal and reciprocal measurements were used for inversion.

2.3.5.2 Mesh design

A tetrahedral finite element method mesh was designed in GMSH [*Geuzaine and Remacle*, 2009] and was extended 60 m away from electrodes to establish Neumann (no electrical current flow) boundary conditions. Elements at the electrodes were assigned a characteristic length of ¼ the minimum inter-electrode distance (0.3125 m) to ensure adequate forward modeling of electrical potentials near the electrodes, while the characteristic length at boundaries was set at 25 m. Elements in between the electrodes and the boundaries gradually spanned lengths in between these two sizes, consistent with the decaying sensitivity of ERI data away from the electrodes. An additional optimization step was performed in GMSH to remove ill-conditioned elements (slivers, caps, splinters, wedges) [*Cheng et al.*, 1999]. In total this produced a mesh with 47,722 voxels and 11,863 nodes.

2.3.5.3 Error modeling and propagation

A forward model of a homogeneous medium was run to assess numerical errors $\boldsymbol{\varepsilon}_f$, while machine precision errors were considered negligible in this study. Forward modeling errors were very small (maximum error of less than 0.015 ohm m), owing to the singularity removal procedure [*Lowry et al.*, 1989] applied in R3t. Singularity removal requires that the surface of the FEM mesh be completely flat. Although our study area was located on a hummock and hollow area of Caribou bog, the maximum topographic variation (0.21 m) among electrodes was smaller than the characteristic length of the smallest element in the FEM mesh. Therefore, we did not consider this microtopography in our inversion.

We used the binning approach of *Koestel et al.* [2008] to build a data error model based on reciprocal errors. In this approach, transfer resistance values are binned and the average value of the bin and the average of the associated errors are plotted. Various models were analyzed (linear, parabolic, cubic, power-law, and exponential) and a linear model of the form $\boldsymbol{\varepsilon}_i = 6.8 \times 10^{-4} + 1.5 \times 10^{-3}\mathbf{d}_i$ was chosen based on having the lowest Akaike Information Criterion (AIC) value [*Aikaike*, 1974]. The AIC is a means of model selection that penalizes complex models; lower AIC values indicate better fitting models with fewer parameters.

A first order spatial derivative smoothness-constrained inversion was performed on the first dataset using R3t. This constraint is necessary to prevent unrealistic solutions to the inverse problem, but comes at the cost of smoothing out the true resistivity distribution such that sharp boundaries are less well resolved. Time-lapse datasets were

adjusted prior to inversion following eq. 2.5, and the starting model was set to the inverse result from the previous time-lapse dataset to urge consistency.

Propagating error according to equation 2.6 assumes that errors are uncorrelated and are thus additive. This has the effect of giving time-lapse datasets larger errors than the background dataset. However, in cases where systematic errors (i.e., errors from mesh discretization, forward modeling, and field configuration) dominate, as might be expected in a low electrical noise environment such as Caribou Bog, much of the error tends to cancel by the inversion approach of *Labrecque and Yang* [2001]. Although difficult to explicitly differentiate between systematic and uncorrelated errors, an initial inversion of all time-lapse datasets revealed that in the vast majority of cases starting errors exceeded the convergence criterion and the inversion could not be carried out. To address this problem, we scaled the convergence criterion by a factor of one-fourth which allowed 105 of the 126 time-lapse datasets (84%) to converge successfully within 2 iterations. The background dataset convergence criterion was not scaled and converged in 6 iterations.

2.3.5.4 Temperature correction

After inversion of the ERI datasets, temperature correction was applied to the inverse results using the method of *Hayley et al.* [2007],

$$m_{std,j} = \left[\frac{k(T_j-25)+1}{k(T_{std}-25)+1}\right] m_j, \tag{2.7}$$

where $m_{std,j}$ is the voxel resistivity corrected to the standard temperature, T_j is the temperature at the location of the model voxel, T_{std} is the desired reference temperature (chosen as 25 °C for this study) and k is a constant describing the linear slope coefficient

between temperature and conductivity of the soil. The constant k was set as 0.0183, shown to be valid for a variety of soil types in the temperature range from 0 to 25 °C [*Hayley et al.*, 2007].

We used data from our HOBO temperature loggers to produce a 1D monotonic Hermite spline function relating temperature to depth for each of the ERI datasets to allow for temperature correction of resistivity values at each voxel throughout the imaged region away from the logger locations. The monotonic Hermite spline function provides a smooth fit through discrete data whilst preventing over and under shooting that may occur in regular cubic interpolation [*Fritsch and Carlson*, 1980]. For voxels below 6.4 m depth, the temperature was fixed to the value of the deepest sensor given that temperature is unlikely to vary significantly below this point. For example, in a two year study of the thermal properties of a northern peatland, *McKenzie et al.* [2007] observed less than 1 °C annual variation at 4 m (the deepest point investigated in their study). Considering that each 1 °C increase in temperature induces a roughly 2% decrease in resistivity, and the stated accuracy of the temperature probes used for the depth-temperature model (± 0.53 °C), we expect the correction to be reliable to within 1%. Although additional uncertainty exists in terms of horizontal variability in temperature (we considered a perfectly layered 1D temperature model) and the depth-temperature model itself, these factors were beyond our means to reasonably constrain further for this study.

2.3.5.5 Time series analysis of ERI datasets

Each dataset collected in this study consists of 47,722 voxels. To assist in the presentation of these data in an informative way, we took two approaches. The first measure we employed was to average the magnitude of the changes observed between

ratio datasets in order to provide a single number to assess how much change has occurred between datasets. To do so, we calculated,

$$\overline{\rho_{rat}} = \frac{1}{M}\sum_{j=1}^{M}\left|m_{std,j}vol_j - 1\right|, \tag{2.8}$$

where M is the total number of model parameters (voxels) in the foreground region and vol_j is the volume of voxel j divided by the total volume of the foreground region. This is essentially the volume-weighted average magnitude of ratio resistivity change, shifted to have a zero minimum. A single $\overline{\rho_{rat}}$ value is calculated for each time step which represents the variation of resistivity in comparison to the previous measurement. All together, the ρ_{rat}values form a time series that summarize the 3D ERI data, and therefore we can expect $\overline{\rho_{rat}}$ to reflect the overall amount of 'activity' in the monitoring region since the last time step.

Our second approach was to analyze the correlation between resistivity and the measured environmental variables, i.e., atmospheric pressure, water level and temperature. All environmental data were available at a resolution of at least one hour, therefore we selected the datapoints most closely corresponding to each hour for our time series analysis. To make ratio resistivity inverse results directly comparable to 1 hour environmental data, we used Gaussian interpolation to form intermediate datasets such that the time series for the resistivity and the environmental parameters had equal length for correlation analysis.

2.4 Results

2.4.1 Initial Site Characterization

2.4.1.1 Environmental variables

Figure 2.3a shows variations in peat temperature throughout the study period. Diurnal variations are observed in the sensor placed just below the peat surface, ranging from 15 to 27 °C. Temperatures in the region down to 2.4 meters increase gradually until the end of the study period, whereas temperatures below 2.4 m range from 6 to 8 °C, but remain relatively steady at each monitoring location (less than 1 °C variation throughout the study period).

Water levels (Figure 2.3b) fluctuate between 0.1 and 0.2 m below the peat surface, being typical for a northern peatland. Although daily variations were observed (likely due to day-night shifts in evapotransporation [*Mitsch and Gosselink*, 2007]), the water level variations mostly appear to be driven by large rainfall events. The water table generally fell from July 4 to July 22, subsequently rose until August 10, and then fell again until the end of the study period. Atmospheric pressure also exhibited daily variations and ranged from 990 to 1030 hPa. The month of July had a distinctly lower atmospheric pressure than August. Several relatively low pressure events (for example, July 18, July 24, August 10, Fig. 2.3b) occur throughout the study and are usually accompanied by relatively large amounts of rainfall. The drops in atmospheric pressure often occur rapidly. Preceding the July 18 low, for example, the pressure dropped from 1017.8 hPa to 1009.4 hPa over a period of twelve hours.

Pore water conductivity and propagated uncertainty (based on probe accuracy, shown as dotted error bars to the right of the plot) are shown in Figure 2.3c. The pore water conductivity varies between 0.010 and 0.023 S m^{-1}. These values are consistent with ranges previously observed in Caribou Bog [*A. S. Reeve*, unpublished data, 2000]. Values ranging from 0.011 to 0.014 S m^{-1} are observed in the 0.2 m depth pore water conductivity data, which we attribute to rainfall and evapotranspiration. We assume that ERI data acquired at the smallest investigation depths reflect these variations to some extent. Consequently, these investigation depths (top 0.2 meters) are excluded from the time series analysis in order to focus on resistivity changes driven by FPG dynamics.

The pore water conductivity recorded at 1.0 m increased from 0.010 to 0.023 S m^{-1} in July, which is unexpected, then remained more or less steady through the rest of the study period. The July increase could result from heavy rains that occurred prior to the field campaigns and dry deposition, from solute transfer from up hydraulic gradient, or possibly due to peat mineralization and subsequent release of organic acids and other ions into the pore fluid. Another possibility could be FPG bubbles forming on the prongs of the sensors, causing instrument malfunction. Unfortunately, we have no data to support these assumptions.

The fluctuations in the 3.0 and 4.5 m data are largely due to the limited precision and accuracy of the probe measurement of bulk conductivity: the 'jittering' effect results from the limits of the 0.001 S m^{-1} precision. Consequently, the pore water conductivity cannot be assumed to be entirely static. Nevertheless, without any reason to believe that there would be substantial changes in fluid conductivity at depth, we believe these data depict

stable pore water conductivity, supporting our association of changes in resistivity with changes in FPG content.

Figure 2.4a shows the calculated sensitivity map for the first ERI background dataset (July 4). As anticipated, sensitivity is highest in the foreground region of the mesh and decays toward the edges. Although all inversions were performed on the entire mesh, we henceforth only present data from the foreground region (the top 6.4 meters of peat below the 28 m by 10 m electrode array). This represents an informed decision to present only those parts of the model space that likely provide reliable information on resistivity variation as inferred from the sensitivity image.

The temperature-corrected background image of the foreground region is shown in Figure 2.4b and depicts a relatively strong resistivity change that occurs at approximately 6.4 m, indicating the peat-mineral soil boundary and consistent with the GPR and coring data. The peat region (above 6.4 m, 24,668 voxels) has an average resistivity of 192 ohm m and standard deviation of 50 ohm m, while the mineral soil region (below 6.4 m, 174 voxels) has an average resistivity of 75 ohm m and a standard deviation of 15 ohm m. A second resistivity change is also depicted within the peat column at around 3 m (coinciding approximately with the position of the 3.45 m woody layer as per Figure 2.2a) characterized by a deeper region (below 3 m) with an average resistivity of 126 ohm m overlain by a shallow region (above 3 m) with an average resistivity of 161 ohm m.

Data from the VEAs were used to build further confidence in the inversion results. Since the apparent resistivity computed from the VEAs represents an average resistivity of the region surrounding the electrodes, we computed average resistivity from

elements from the 3D inversion within 1.25 m of the center of the quadripole for comparison (Figure 2.4c). In general, the 3D results appear smoothed out compared to the variation observed at the VEAs, consistent with the smoothness constraint imposed by the inverse algorithm. The ERI-derived resistivities are consistently higher than the apparent resistivities from the VEAs between 2 and 5 m depth, which may result from differences in sampling volumes between the two measurements. Nevertheless, a consistent pattern is visible between the ERI and VEA results, adding confidence that the time-lapse ERI inversions are reliable throughout the part of the model domain defined to have sufficient resolution.

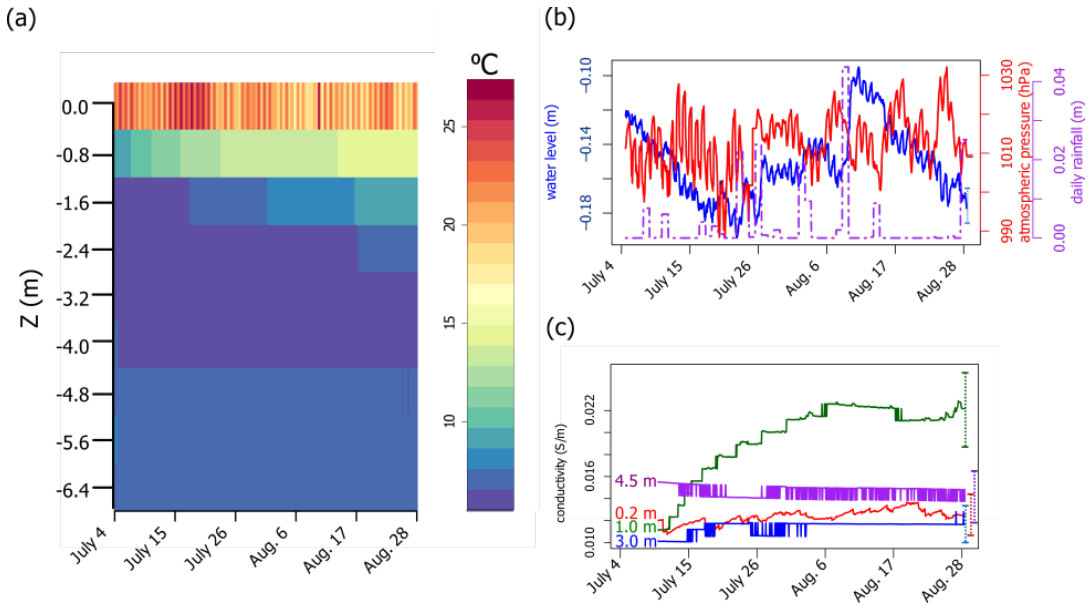

Figure 2.3 – Plots of key environmental parameters throughout the monitoring study: (a) peat temperature recorded at the 9 HOBO loggers through time; (b) water level (compensated for atmospheric pressure variations), atmospheric pressure, and rainfall events; (c) calculated pore fluid conductivity at 0.2, 1.0, 3.0, and 4.5 m.

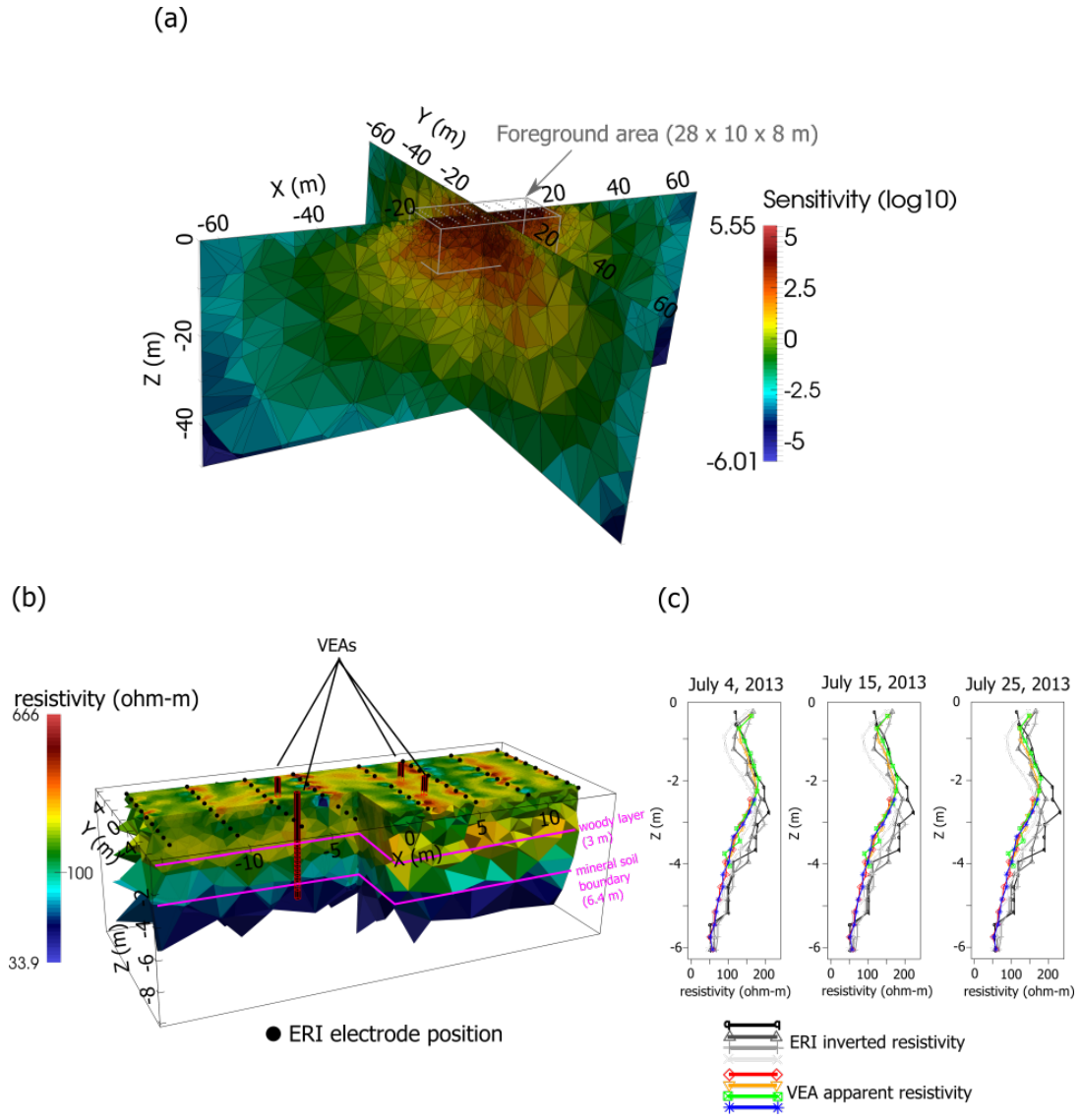

Figure 2.4 – Results of the background dataset inversion from July 4. (a) Fence diagram showing sensitivity of voxels within the FEM mesh – the expected pattern of decaying sensitivity away from the electrodes is observed; (b) cut of the inverted 3D background dataset. The inverted resistivity values depict a boundary near the base of the peat and at a woody layer (shown as pink lines); (c) apparent resistivity values captured by the vertical electrode arrays compared with the inverted resistivity values from the voxels corresponding to the vertical electrode array measurement locations. The values from the 3D inversion are smoothed, but show good agreement with the vertical electrode arrays in terms of magnitude and shape.

2.4.2 Monitoring of resistivity changes

2.4.2.1 Time-lapse ERI results and atmospheric pressure

Figure 2.5a shows $\overline{\rho_{rat}}$ and ratio changes in atmospheric pressure. Figures 2.5b-f show the actual ERI ratio resistivity values from points along the time series, while Figure 2.6 shows increases and decreases in ratio resistivity for a selected time period centered on July 6 (Fig. 2.5b). The distribution of ρ_{rat} is leptokurtic (kurtosis >> 0) with a mean slightly less than 1 (0.99996), a standard deviation of 0.002, and bounds of 0.868 and 1.14. We used the standard deviation to apply a threshold to the ERI images in Figures 2.5b-f to only show absolute changes greater than 0.2% between the one hour interpolated datasets. Ratio resistivity values smaller than 0.9 or larger than 1.1 are shown as color saturated.

Visually, $\overline{\rho_{rat}}$ appears to give a good indication of the overall ratio changes occurring in the actual ERI images. Figures 2.5b,c,d, and f correspond to the four largest $\overline{\rho_{rat}}$ events and occur during abrupt drops in atmospheric pressure (low ratio pressure), whereas Figure 2.5g is a relatively large $\overline{\rho_{rat}}$ event occurring during a period of rising atmospheric pressure, but closely follows a drop in atmospheric pressure (within 24 hours). Fig. 2.5e is a representative image for a relatively static time both in terms of $\overline{\rho_{rat}}$ and atmospheric pressure. Each of the images in Figures 2.5a-g show ratio resistivity changes greater than 0.2 % across the shallow peat layer, while the three July datasets corresponding to large $\overline{\rho_{rat}}$ events (Figs. 2.5b, c, and d) depict strong ratio resistivity changes at depth. Fig. 2.5b depicts predominantly decreases in ratio resistivity

in the shallow peat and predominantly increases in the deep peat, while Figs. 2.5c and 6d show the reverse pattern.

The August images (Figs. 2.5f and g) show fewer ratio resistivity changes greater than the 0.2 % threshold than the July images (Figs. 2.5b, 2.5c, and 2.5d), but depict a similar pattern to that observed in Figs. 2.5c and 2.5d. In Figs. 2.5f and 2.5g, changes in ρ_{rat} > 0.2 % are limited to the uppermost layer and a region of increase in the center of the image not extending beyond 4 m depth. The average ratio resistivity for August 10 midnight (corresponding to Fig. 2.5f) is positive, while the average ratio resistivity for August 24 midnight (corresponding to Fig. 2.5g) is negative, despite the positive anomaly observed in the center of the image.

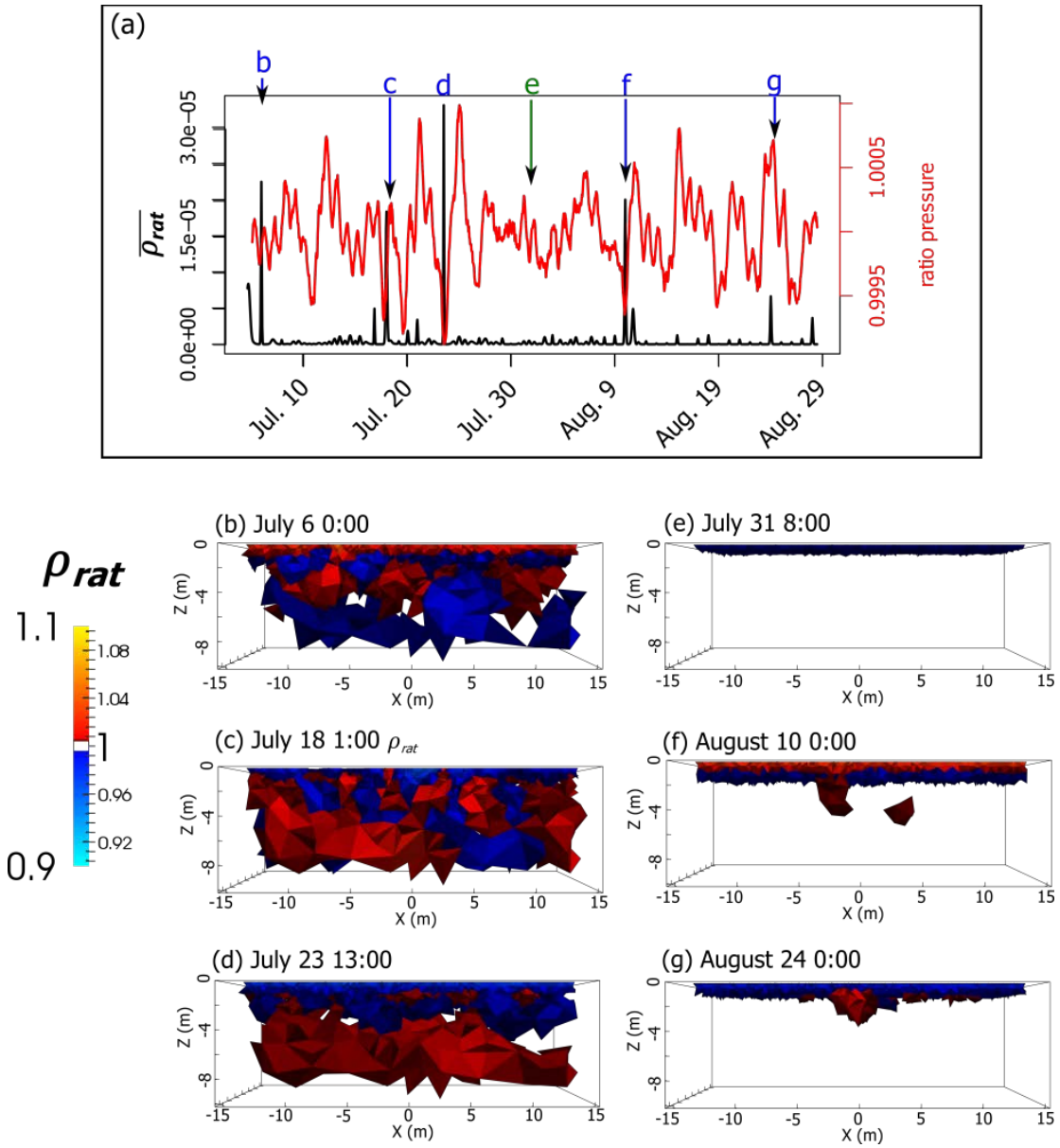

Figure 2.5 – Time-lapse ERI results: (a) average absolute ratio resistivity magnitude ($\overline{\rho_{rat}}$, black) plotted with ratio atmospheric pressure (red). (b-g) select ratio ERI images from the time series. A threshold has been applied to only show changes with magnitude > 0.002 to enhance visibility.

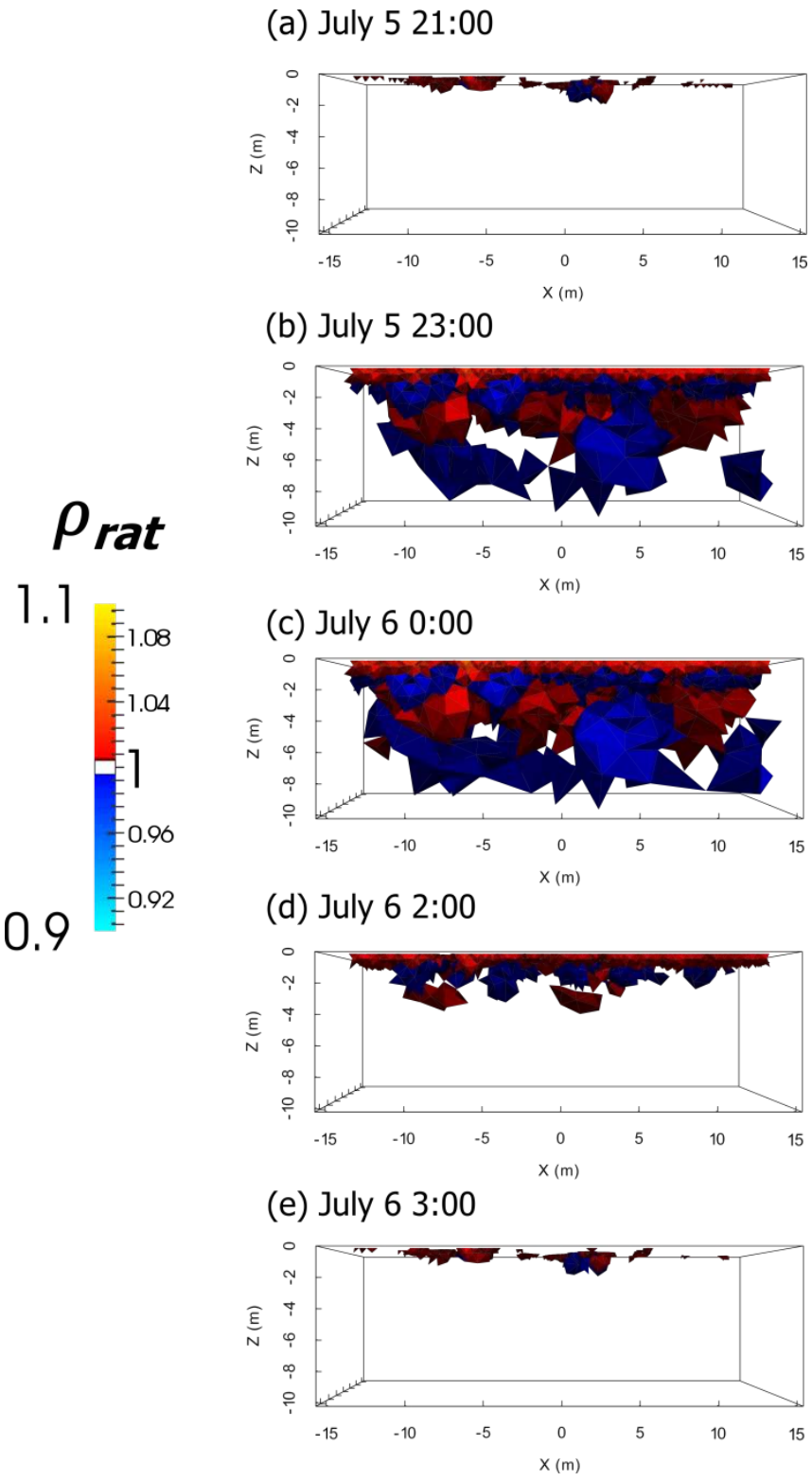

Figure 2.6 – selected time-lapse images before (a-b), during (c), and following (d-e) the July 6 $\overline{\rho_{rat}}$ event.

2.4.2.2 Direct flux measurements, water levels, and atmospheric pressure compared to ERI

Figure 2.7 shows ratio of atmospheric pressure magnitude, $\overline{\rho_{rat}}$, and CH_4 flux data from the dynamic flux chamber during 5 monitoring periods. The flux data consist of a steady, background flux (< 15 mg CH_4 m^{-2} d^{-1}) punctuated by relatively large flux events that show up as spikes (up to 260 mg CH_4 m^{-2} d^{-1}). These spikes occur mostly during periods of decreasing atmospheric pressure (as in flux monitoring periods 1, 2, 5, and partly in 3), but also appear to occur during rising atmospheric pressure (flux monitoring periods 4 and partly in 3). The largest $\overline{\rho_{rat}}$ events are annotated with their corresponding images in Figure 2.5.

There is some correspondence between CH_4 flux recorded at the center of the array and $\overline{\rho_{rat}}$, in that elevated flux apparently corresponds to elevated $\overline{\rho_{rat}}$ on several occasions (Figure 2.7). Flux monitoring periods 1, 3, and 4 depict this general visual relationship, although there appears to be little correlation with the direct flux measurements and $\overline{\rho_{rat}}$ in terms of magnitude. Additionally, monitoring period 2 shows little change in $\overline{\rho_{rat}}$ despite collection of several ERI datasets during this time period and a drop in atmospheric pressure and corresponding elevated CH_4 flux recorded at the surface. There are no large $\overline{\rho_{rat}}$ events during monitoring period 5, but there is a large event that occurs a few hours later during an atmospheric pressure minimum (the CH_4 flux monitoring time series does not overlap this event).

Figures 2.8a and 2.8b show the percentage of the peat volume with moderate to strong (magnitude of $r > 0.4$) linear correlations between ERI resistivity and atmospheric pressure in the shallow and deep peat. Almost no linear correlation exists between atmospheric pressure and resistivity at either depth, even if there appears to be a time lag of various lengths between drops in atmospheric pressure and spikes in $\overline{\rho_{rat}}$ (Fig. 2.5a). In contrast, Figures 2.8c and 2.8d show correlations between water levels and resistivity in the shallow and deep peat. In both cases, a significant portion of the peat volume exhibits moderate to strong negative linear correlations (54 % in the shallow peat, 18 % in the deep peat). Figure 2.9a shows only voxels with correlations of magnitude greater than 0.7, and Figure 2.9b shows an example time-series plot of resistivity and water levels. These correlations occur in the region below the water table, which varies throughout the study period between 0.1 and 0.2 m depth (Fig. 2.9a).

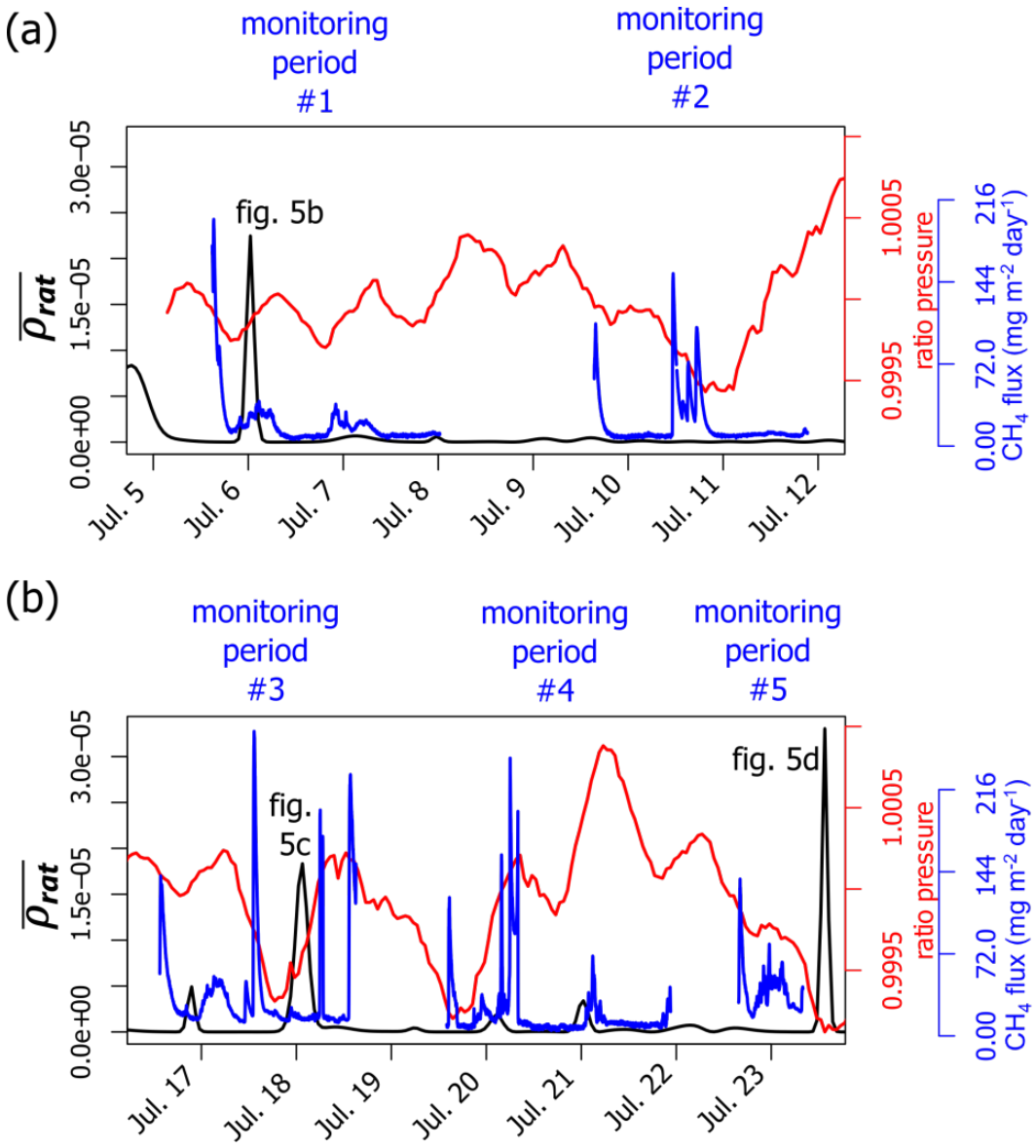

Figure 2.7 – Data from the five dynamic flux chamber monitoring periods (blue), the average absolute ratio resistivity magnitude ($\overline{\rho_{rat}}$, black), and ratio atmospheric pressure (red).

2.5 Discussion

2.5.1 The unique nature of ERI measurements: monitoring FPG dynamics in peat soils at different temporal scales

This study shows the potential of ERI to monitor biogenic gas dynamics within peat soils at high (i.e., hourly) temporal scales. Despite that the technique represents an indirect measurement of gas content as based on changes in electrical conductivity, the method is unique for its ability to autonomously monitor gas dynamics within the peat matrix, therefore representing a minimally invasive measurement. Although installation of the VEAs represent greater disturbance to the peat (compared to the surface ERI), the results of this study indicate that surface array measurements are sensitive enough to observe FPG dynamics in peat, and that within peat VEA measurements are likely not required for future studies of this kind. Furthermore, the ERI method is able to provide information on gas dynamics and migration through the peat column beyond traditional methods (i.e., chambers) that are only able to capture gas releases once reaching the peat-air interface. For example, Figure 2.6 shows increases and decreases in ratio resistivity within the shallow and deep layer around the drop in atmospheric pressure on July 6. The changes are interpreted as gas content increasing in the shallow layer while decreasing in the deeper layer. This pattern might represent vertical migration of gas from deeper to shallower layers. Being able to capture such trends in gas dynamics within the peat column at the temporal resolution shown here (i.e., hourly) has never, to our knowledge, been reported before and exemplifies the unique potential of ERI to monitor gas dynamics in peat soils.

We note that there are some inherent limitations to interpretation of time-lapse ERI as a proxy for FPG dynamics. For one, ERI measurements take time to perform (in this study, 1.25 hours), and thus limit the temporal resolution. Inverted ratio resistivity values represent the sum of all resistivity changes between datasets, which may reflect multiple FPG events. Second, given the time it takes for ERI data collection to occur, ERI measurements do not capture an instantaneous time slice of a dynamic process. Although we are treating changes in resistivity as having occurred between two datasets, such changes could partially represent changes that are taking place during data collection.

Given the indirect nature of ERI measurements, changes in resistivity have multiple interpretations. We have asserted that increases in total FPG volume will be mirrored as increases in resistivity; likewise decreases in FPG volume will show as decreases in resistivity. Volume changes in FPG result from two main processes. First, abrupt gas transfer and/or ebullition events will result in substantial local gains or losses in FPG content, and should be visible in ERI images assuming the events are of detectable magnitude. Second, pressure variations (due to atmospheric or hydrostatic fluctuations) will result in volume changes to the FPG bubbles themselves according to Henry's Law and the ideal gas law. Decreases in pressure allow bubbles to expand, while increases in pressure cause bubble contraction. Significant dilation of FPG bubbles should appear as an increase in resistivity and *vice versa*.

For example, a decrease in water level of 10 cm (the approximate range observed in this study, see Fig. 2.3) is roughly equivalent to a decrease in hydrostatic pressure of 10 hPa below the water table. According to Henry's Law and the Ideal Gas law and assuming an average temperature of 10 °C, an ambient pressure of 1000 hPa and that the

FPG consists solely of methane, this change would induce an approximate +1% increase in bubble volume. Assuming a porosity representative of Caribou Bog of 0.94 [*Parsekian et al.* 2012b] and employing equation 2.3, this would be manifest as a +1.5% increase in ratio resistivity. This change is much greater than the average data error observed (0.46%), and should be well within detection limits of our ERI setup.

Although a quantitative link directly mapping ERI data to FPG content has been deemed unreasonable (in our study as well as the laboratory studies of *Slater et al.* [2007] and *Kettridge et al.* [2011]), we have taken careful measures to ensure that ERI inversion results can be qualitatively interpreted as changes in FPG content. First, we compensated for temperature in the ERI inverse results using data from 8 sensors spanning from the peat surface to the mineral soil (Fig. 2.3a). Second, we observed stable pore fluid conductivity values at 0.2 m, 3.0 m, and 4.5 m depth, although the 1.0 m conductivity probe did exhibit some variation (Fig. 2.3c). Third, we confine our interpretations to below the water table (maximum depth 0.2 m, Fig. 2.3b) to avoid mistakenly interpreting water level variation as gas development/release. Fourth, we constrain our analysis to the foreground (high sensitivity) region of the ERI inversion mesh (Fig. 2.4a). Fifth, we cross-validated our ERI inverse resistivity magnitudes with apparent resistivity recorded at the VEAs (Fig. 2.4c).

The ERI difference inversion successfully captured several major events within the peat during the two month study period. Rates of resistivity change of over 0.2 % per hour were observed throughout the entire peat column during these events. Such events also seem to indicate some general trends in biogenic gas accumulation and release during the two month monitoring period that may be potentially related to the

stratigraphy of the peat column. For example, the event on July 6 (Figure 2.5b) shows a marked decrease in resistivity below 3 m coinciding with an increase above 3 m that could be interpreted as a breach in the wooden layers described between 3-4 m (Figure 2.2) followed by release of gas that moves into the layers above. Subsequent events (i.e., July 18 and 23, Figures 2.5c and 2.5d respectively) show a marked increase in resistivity below 3 m that could be interpreted as periods where gas accumulation below the wooden layer increases gradually due to entrapment.

Comparison of the ERI data with the CH_4 flux data and the atmospheric pressure variations (Fig. 2.7) suggests that the large $\overline{\rho_{rat}}$ events represent either large-scale ebullition and/or FPG transfer events, FPG bubble volume changes due to changes in pressure, or both. Each of these events (Figs. 2.5b, 2.5c, 2.5d, 2.5f, and 2.5g) occurs during or soon after a rapid drop in atmospheric pressure (Fig. 2.5a). The events shown in Figs. 2.5d, 2.5c, and 2.5f occur within 4 hours of the first, second, and fourth largest local minima in ratio atmospheric pressure, whereas Fig. 2.5b and Fig. 2.5g occur within several hours of smaller local ratio atmospheric pressure minima. These abrupt changes in FPG content associated with sudden drops in atmospheric pressure are consistent with the findings of many others [*Bon et al.*, 2014; *Comas et al.*, 2011a; *Kellner et al., 2006*; *Kettridge et al.*, 2011; *Tokida et al.*, 2007; *Waddington et al.*, 2009; *Yu et al.*, 2014].

Most of the events shown in Figure 2.5 (2.5c, 2.5d, 2.5f, and 2.5g) depict a pattern of decreased ρ_{rat} in the surface layer while increases primarily occur below 1 m depth. This resistivity structure is consistent with ebullition primarily occurring from the shallow peat (decreasing resistivity), and gas bubble expansion (increasing resistivity) due to decreasing atmospheric pressure occurring in the deep peat. Figures 2.5f and 2.5g

show a localized increase in ρ_{rat} in the deep peat near the center of the study area. This region of increased ρ_{rat} may reflect a gas pocket formed from the upward migration and subsequent expansion of many small bubbles within this pocket due to decreased atmospheric pressure. Although this localized increase occurs in the center of the ERI array where sensitivity is relatively greater, it is unlikely that this region is simply an artifact of the ERI sensitivity given that both our synthetic and field tests were able to image large (>0.2 %) changes in resistivity outside of this area.

Overall, the patterns observed in this time-lapse resistivity dataset support the shallow peat model of *Coulthard et al.* [2009] in that ebullition appears to most commonly originate from the shallow (upper meter) peat rather than the deep peat. As we emphasize, the link between resistivity data and FPG content is not sufficiently robust to provide an estimate of the actual volumes of gas being released from either zone. Therefore, although unlikely based on our data, it is possible that the deep peat ebullition event observed in Fig. 2.5b may be responsible for significantly more FPG release than the other events we observe. In addition, we note that this study took place in the summer months and that gas dynamics vary seasonally [*Comas et al.*, 2008]. For example, the deep peat may play a larger role during the fall and winter months as surface temperatures cool and the shallow peat eventually freezes.

2.5.2 Comparison of ERI and direct flux data

Figures 2.5b, 2.5c, 2.5d, and 2.5f show the four largest events in terms of $\overline{\rho_{rat}}$. Of these events, only the smallest, Fig. 2.5f, fails to show >0.2 % per hour changes throughout the entire peat profile, although large resistivity changes are still observed in the upper layer. Although there is some correspondence between CH_4 flux recorded at

the center of the array and $\overline{\rho_{rat}}$, there is no clear (i.e., quantitative) relationship between the timing and magnitude of these two parameters. These observations highlight the difference in scale between ERI measurements and chamber-based measurements. Apparently large ebullition events recorded at the CH_4 flux chamber do not necessarily appear as large events throughout the peat volume sampled by ERI. Clearly, the spatiotemporal resolution of the ERI is not fine enough to capture such spatially-localized events recorded at the flux chamber. Such discrepancies illustrate how upscaling from chamber measurements to a global scale could potentially be very misleading, and finding the 'appropriate' spatiotemporal scale to capture FPG dynamics in wetlands is an ongoing research problem as illustrated in other recent studies (for example, [*Stamp et al.*, 2013; *Comas and Wright*, 2014]).

2.5.3 Time series analysis of ERI, water levels, and atmospheric pressure

Atmospheric pressure and resistivity exhibit almost no linear correlation in either shallow or deep zones (Fig. 2.8a and 2.8b). This may be due to conflicting effects of atmospheric pressure on FPG dynamics: low pressure driving both gas expansion and ebullition, high pressure both causing bubble contraction and enhancing mobility (allowing for transfer/release). Although abrupt pressure decreases clearly trigger large changes in resistivity, particularly at depth, there is no linear dependency of resistivity on pressure. This indicates the non-stationary dependency of the peat gas dynamics on episodic changes in atmospheric pressure only.

A substantial portion of the peat volume shows moderate to strong linear correlations with water levels (Fig. 2.8c and 2.8d). Figure 2.9b illustrates that the strong negative correlations are primarily trend-driven, as the resistivity does not appear to respond to the

small fluctuations in water level. This is confirmed by differencing the two time series, which reveals weak to no correlation (not shown). Although each data set was interpolated to a common 1 hour interval for time-series analysis, it is possible the small fluctuations in water level are not reflected in the ERI data due to differences in the actual sampling rate of the instruments. The water level data were sampled at 15 minute intervals, whereas ERI data were collected no faster than 2 hours apart.

We therefore attribute the moderate to strong negative correlations between resistivity and water level below 0.2 m depth to bubble contraction/dilation due to hydrostatic pressure variation. The fact that more correlation is observed in the shallow peat may have to do with (1) the enhanced sensitivity of ERI within this region, (2) possibly higher FPG content in the shallow peat, and/or (3) a greater ability for bubbles to expand/constrict in the shallow peat possibly due to generally higher elasticity of the shallow peat matrix.

Assuming the FPG release dynamics we observe are primarily driven by pressure variations, we might expect to see similar relationships between resistivity and water level as well as resistivity and atmospheric pressure. We attribute this discrepancy to the magnitude of hydrostatic pressure variations, equivalent to roughly 10 hPa over weeks, versus atmospheric pressure, which varies up to 20 hPa in a single day. Thus, it seems that atmospheric pressure is primarily responsible for driving large FPG transfer and release events, whereas hydrostatic pressure may also contribute to these events (the events observed in Figs. 2.5c and 2.5d also occur during relatively low water levels). Whereas abrupt changes in atmospheric pressure episodically trigger major gas releases, water levels appear to immediately change bubble size through compression and

expansion. This phenomenon was clearly observed (visually and through GPR monitoring) by *Chen and Slater* [2015] in a peat monolith taken from Caribou Bog.

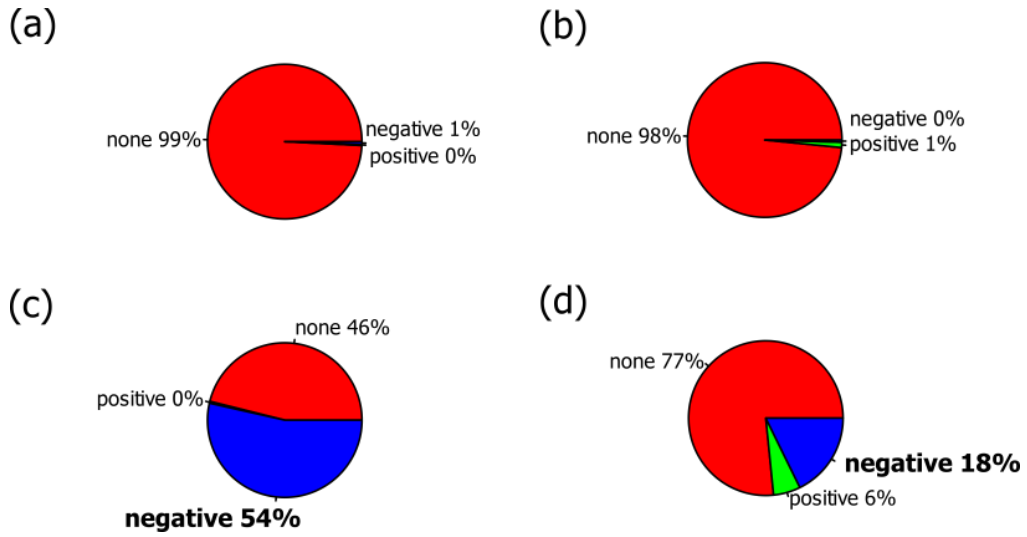

Figure 2.8 – Pie charts summarizing the Pearson correlation coefficient between ERI resistivity and environmental variables for deep (> 1 m) and shallow (top meter) peat. Note only 'moderate' to 'strong' correlations (larger than ± 0.4) are shown. (a-b) show correlations between resistivity and atmospheric pressure; 99% of the shallow (a) and deep (b) peat regions show little to no linear correlation. (c-d) shows correlations between resistivity and water levels; over half the shallow peat region (c) shows moderate to strong negative correlations with water level, whilst most of the deep peat region (d) shows no moderate to strong linear relationship with water level, 18% of the region still exhibits a negative correlation.

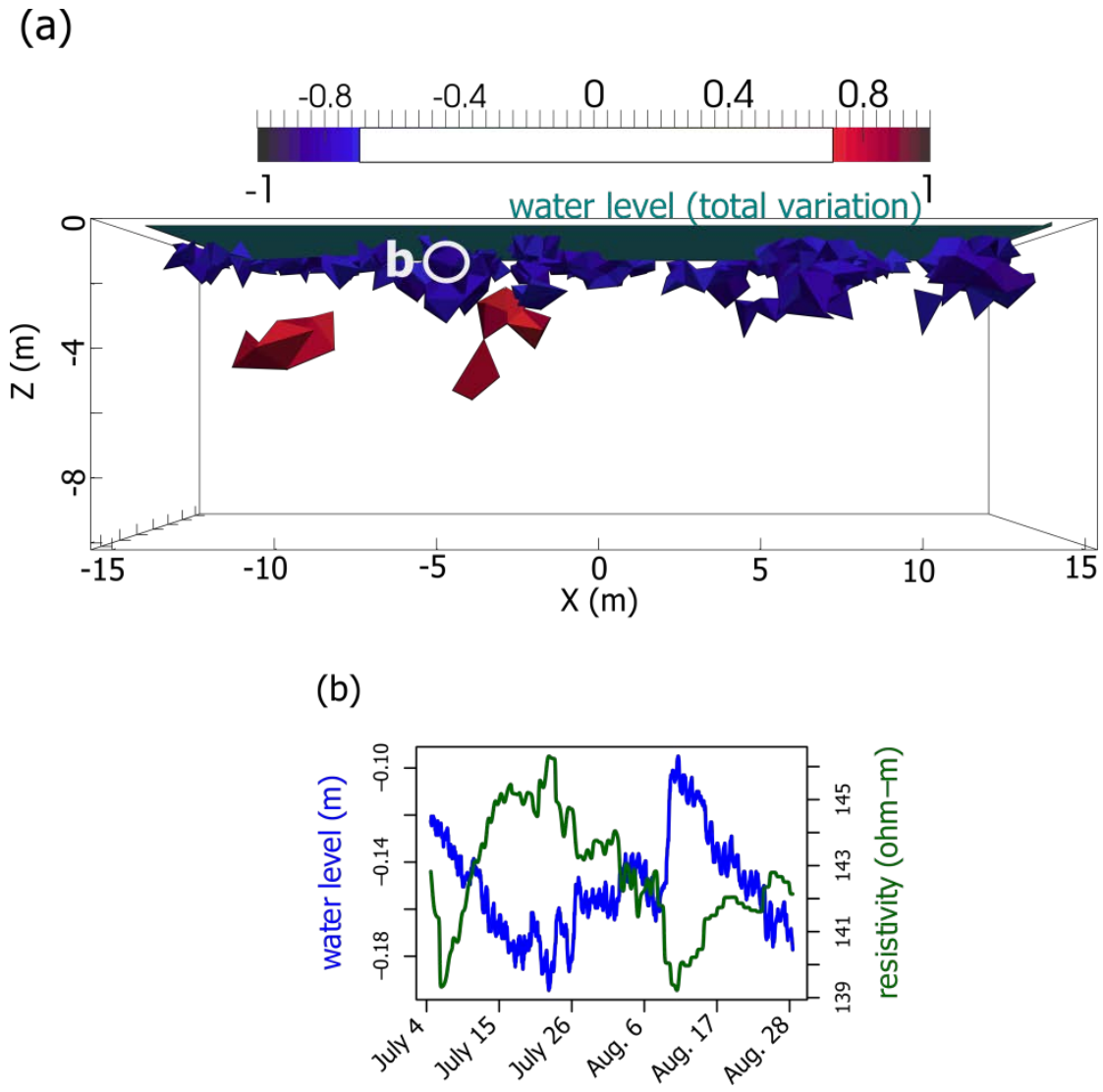

Figure 2.9 – correlation between water level and resistivity; (a) voxels with correlation coefficients having magnitudes greater than 0.7. The range of water levels are also shown; (b) water level (blue) and resistivity (green) time series at a voxel in the shallow peat exhibiting a -0.89 correlation.

2.6 Conclusions

ERI is a unique method for autonomously monitoring FPG dynamics in peat soils at high (i.e., hourly) temporal scales. The method is able to provide information on gas dynamics and migration through the peat column while bringing some insights about mechanisms for FPG releases. For example, drops in atmospheric pressure appear to exert control over FPG transfer and ebullition events as inferred from ERI. Most of these events are associated with a loss of FPG in the shallow peat and an increase in FPG in the deep peat, however we were unable to establish a quantitative link between atmospheric pressure and FPG content using our ERI data. The increase in FPG content in the deep peat during drops in atmospheric pressure may result from collection of gas below a confining layer and/or bubble expansion during low pressure. In one notable case, we observed a large decrease in FPG content from the deep peat. This likely reflects a rupturing event in which FPG buildup in the deep peat breaks through a confining layer and transfers to the shallow peat and/or is released to the atmosphere.

Water level variations were not found to trigger ebullition or FPG transfer events in this study. However, even small variations in hydrostatic pressure (less than 10 hPa over the 2 month study period) appear to control FPG bubble contraction/dilation, as evidenced by the substantial portion of the shallow and deep peat showing moderate to strong negative linear correlation between water levels and resistivity. Although it is probable that water level variation could trigger ebullition and gas transfer in a manner similar to atmospheric pressure, the gradual nature of the hydrostatic pressure change compared to atmospheric pressure change makes this hydrostatic pressure trigger less likely. Likewise, given the relatively abrupt rate of atmospheric pressure change (>20

hPa in a single day), the temporal resolution of our ERI measurements (collected twice a day on average) may not be sufficient to capture rapid changes in bubble volume.

Although power considerations and data collection time limited our maximum temporal resolution, this is not a limitation of the ERI technique. Depending on the data collection scheme, time-lapse ERI data could be collected every few minutes or possibly even more rapidly. In addition, we have shown the ability of time-lapse ERI for depicting an *in situ* dynamic process occurring over several meters within the deep peat (down to 6.4 m); a regime otherwise difficult to sample. Importantly, ERI also minimizes disturbance of peat structure. Although we recognize the inability of the technique to directly estimate FPG content, there is immense value in employing ERI coupled with other environmental measurements to study biogenic gas dynamics in wetland soils. In the future, ERI could be used to directly compare below ground CH_4 dynamics with CH_4 fluxes at the surface if coupled with systems that measure on similar scales (such as infrared CH_4 cameras [*Gålfalk* et al. 2015] and/or multiple chambers [*Stamp* et al. 2013]). Such a study would serve to constrain conceptual models of below ground peatland gas dynamics and further clarify the relative importance of shallow versus deep peat to methane fluxes.

Chapter 3: The influence of peat structure on biogenic gas dynamics: a multi-method comparison of two sites in a northern peatland[1]

Abstract

Modeling the response of peatlands to global climate change is limited by uncertainty in the spatiotemporal variability of biogenic gas dynamics within peatlands. Particularly, there are few observations of gas dynamics from deep peat (below 1 m) regimes. We apply an integrated approach using direct time-lapse measurements of free phase gas content and methane flux, combined with indirect measurements of peat surface deformation, ground penetrating radar, and electrical resistivity imaging to better understand how two sites within Caribou Bog, Maine differ in terms of gas dynamics. The first 'pool and esker' site exhibits a high degree of decomposition at depth whereas a 'wooded heath' site exhibits less decomposition and the presence of wood-rich layers. Gas content within the peat is lower at the pool and esker site, but methane fluxes are higher. Electrical resistivity imaging indicates that gas contents are highly variable in deep zones suggesting complex production and release processes, particularly near an area where an underlying esker deposit reaches a topographic high. By contrast, the wooded heath site shows higher gas content but typically lower methane fluxes and fewer sudden changes in gas content in the deep peat. Ebullition events from the deep peat seem to be at least as common as those from the shallow peat at the pool and esker site, whereas most gas dynamics occur in the upper meter of peat at the wooded heath site. Differences in gas dynamics appear to be strongly controlled by physical properties of the peat and peatland hydrogeology.

[1]This chapter submitted to *Journal of Geophysical Research: Biogeosciences* as: Terry, N., L. Slater, X. Comas, A. S. Reeve, K. V. R. Schäfer, and W. Wright (2016), The influence of peat structure on biogenic gas dynamics: a multi-method comparison of two sites in a northern peatland.

3.1 Introduction

Peatlands are extremely important in regulating the global carbon balance and are believed to hold up to 30% of the global soil carbon pool [*Parish et al.*, 2008]. Peatlands are major sinks for atmospheric CO_2 and sources for CH_4, and northern peatlands alone are estimated to be responsible for up to 10% of all CH_4 flux [*Charman*, 2002]. Despite CH_4 having 28-34 times the warming potential of CO_2 [*Stocker et al.*, 2013], peatlands are believed to have a net cooling effect on the millennial time scale [*Frolking et al.*, 2006]. However, increasing temperature and precipitation expected in the face of climate change may as much as double CH_4 emissions from peatlands in the 21st century, particularly in northern zones [*Zhuang et al.*, 2006]. The role of peatlands in response to global climate change is still highly uncertain, due to uncertainty and/or inadequate incorporation of the controls governing CH_4 dynamics within peatlands into biogeochemical models, errors due to upscaling small-scale measurements to large areas, and the relatively limited number of observations with which to constrain parameterizations of global models [*Bridgham et al.*, 2013].

The CH_4 flux from peatlands occurs through diffusion, transport through vascular plants, and ebullition processes. The role of ebullition in particular is still a much debated topic, with two conceptual models ascribing different levels of importance to different peat depth regimes. Inspired by studies in the Glacial Lake Agassiz peatlands (GLAP) in Northern Minnesota [i.e., *Chanton et al.*, 1995; *Chasar*, 2002; *Chasar et al.*, 2000a, 2000b; *Crill et al.*, 1988, 1992; *Romanowicz et al.*, 1993, 1995; *Rosenberry et al.*, 2003; *Siegel et al.*, 2001], the 'deep peat model' of *Glaser et al.* [2004] stresses hot spot

production of CH_4 in deep peat (below 3 m) and buildup of gas in overpressurized pockets maintained by structurally competent layers (such as layers of undecomposed material or peat fabric). Rupture of these confining layers, such as through a large drop in pressure, may trigger sudden release of this gas resulting in relatively enormous fluxes. For example, *Glaser et al.* [2004] calculated a loss of 130 g m^{-2} of CH_4 from 3 individual ebullition events.

On the other hand, the 'shallow peat model' proposed by *Coulthard et al.* [2009] stresses the importance of fluxes driven by production in the shallow (top meter) anaerobic peat made possible by higher summer temperatures and availability of labile C compared to deeper regimes. This model is based upon numerous studies of gas dynamics in shallow peat [e.g., *Baird et al., 2004*; *Beckwith and Baird*, 2001; *Christensen et al.*, 2003; *Comas and Slater*, 2007; *Kellner et al., 2006*; *Laing et al.*, 2008; *Ström et al.*, 2005; *Tokida et al.*, 2005a]. *Coulthard et al.* [2009] do not discount the potential importance of deep peat gas fluxes, but rather suggest that it is unknown and that more direct observations are needed.

Comas et al. [2014] suggest that both shallow and deep peat models are applicable depending on the physical properties of the peat. In their study, they compare data from two peatlands: one in Caribou Bog, Maine (characterized by lower and more variable levels of decomposition and the presence of wooden layers) and one in Cors Fochno, Wales (characterized by higher and more homogenous levels of decomposition). Through ground penetrating radar (GPR) analysis constrained by coring and gas sampling, *Comas et al. [2014]* demonstrate that Caribou Bog shows on average larger gas content and variability (5.5% -10.8%) compared to Cors Fochno (ranging between

2.5% and 5.7%). Although the findings of *Comas et al.* [2014] suggest the importance of peat physical properties for regulating gas dynamics in peat, they do not provide evidence of releases of gas from the deep peat, mainly since time-lapse measurements were not collected.

There is growing evidence to support the importance of peat structure as a control on gas dynamics in peatlands. For example, *Kettridge and Binley* [2011] found porosity and structural arrangement of the peat to be key factors in determining the gas trapping potential in a modeling experiment based on x-ray computed tomography of 8 peat samples consisting of two different types of peat. Naturally, these properties are often tied to the degree of peat decomposition, with more humified peat typically exhibiting a lower interconnected porosity and permeability [*Boelter*, 1969; *Rycroft et al.*, 1975; *Quinton et al.*, 2008; *Grover and Baldock*, 2013; *Morris et al.*, 2015]. Permeability within the peat not only influences the ability of bubbles to migrate, but also impacts the rate at which methanogens are supplied with labile C to create more gas [*Bon et al.*, 2014]. Saturated hydraulic conductivity in peatlands is highly variable ranging from 7.0 x 10^{-6} up to 1.3 x 10^{-2} m s^{-1}, with typically higher hydraulic conductivity in the shallow peat due to large pore sizes (up to 5 mm) and rapidly decreasing permeability with depth related to increased levels of decomposition and compaction [*Rezanezhad et al.*, 2016]. Among others, *Chason and Siegel* [1986] and *Baird et al.* [2016] challenge the commonly held assumption that peat permeability decreases with depth, and demonstrated that deep peat may be as permeable as shallow peat. Further, *Baird et al.* [2016] provide evidence that deep peat permeability can vary significantly between different land types, or microforms, in bogs over distances of as little as 1 – 5 m, and call

for further research to demonstrate the importance of variability between different peat microforms.

Hydrogeologic properties of the underlying mineral soil may also play a significant role in gas dynamics in peatlands. Permeable mineral soil lenses may enable a hydrological connection between the peat and the mineral soil [*Reeve et al.*, 2000, 2009; *Comas et al.*, 2011b], in contrast to the traditional view of ombotrophic peatlands as 'bathtubs' that are hydrologically disconnected from the inorganic material below. In this case, differences in permeability drive hydrologic gradients and flow reversals that enhance dispersive mixing [*Reeve et al.*, 2006] between the mineral soil and peat that facilitate increased ion exchange. These ions could act as alternative electron acceptors that enhance decomposition in deep peat. Further, a highly permeably mineral soil could drive downward flow and may also serve to supply labile C from fresh peat near the surface to methanogens in the deep peat [*Bon et al.*, 2014].

This study describes an integrated approach to compare two microsites within Caribou Bog, Maine that demonstrate clear differences in peat physical properties and associated gas dynamics. We employ time-lapse geophysical and environmental sensor monitoring, as well as measurements of CH_4 flux and peat deformation, to investigate deep peat gas dynamics. Our results suggest that a site dominated by pools and underlain by an esker deposit exhibits a high level of decomposition, relatively low gas content and gas content that varies with depth with a maximum at 3 m. In addition, there are apparently larger fluctuations in gas content over time. These combined observations support earlier hypotheses that an esker deposit enhances rates of decomposition and gas production within the deep peat. On the other hand, a wooded heath site dominated

mostly by shrubs and small trees and underlain by a continuous clay mineral soil exhibits a lower level of decomposition at depth and possesses layers of laterally contiguous woody debris. While this site exhibits higher overall gas content, gas content declines with depth and there appears to be less overall variation during the monitoring period. The results of this work highlight the importance of deep peat and underlying geology of peatlands as well as lateral variability in terms of gas dynamics within different microsites of the same peatland.

3.2 Background

3.2.1 Electrical Resistivity Imaging (ERI)

The use of electrical resistivity imaging (ERI) to monitor gas dynamics in peatlands has been demonstrated in multiple laboratory studies [*Slater et al.*, 2007; *Kettridge et al.*, 2011] and in a recent field study [*Terry et al.*, 2016]. Collecting ERI data proceeds by injecting current through multiple electrode pairs and measuring electrical potential at other electrode pairs placed in the soil. The objective of collecting these measurements is to construct a resistivity distribution of the subsurface, which typically requires a numerical (inversion) approach (as there are usually much fewer measurements than resistivity values to solve for). Since there is typically no unique solution to the inverse problem, a smoothness constraint is generally applied that encourages adjacent resistivity values in the numerical mesh to take on similar values. Thus, models of subsurface resistivity are blurred versions of real conditions.

Archie's Law provides a link between the resistivity of the soil ρ_{soil} and physical properties of the soil,

$$\frac{1}{\rho_{soil}} = \sigma_{el} = (\phi_{int})^m S^n \sigma_w, \quad (3.1)$$

where σ_{el} represents the flow of current through ions in the pore fluid, ϕ_{int} is the interconnected porosity, S is saturation, σ_w is the conductivity of the pore fluid, m is the 'cementation' factor which relates to pore geometry, and n is an exponent describing the variation of resistivity with water saturation. Eq. 3.1 does not consider surface conduction or electrical conduction effects, both of which may be at play in peat soils [*Comas and Slater*, 2004].

Slater et al. [2007] further established a link between soil resistivity and gas content,

$$\rho_{rat} = \frac{\rho_{soil,t}}{\rho_{soil,0}} = \left[\frac{\phi_t - FPG_t}{\phi_0 - FPG_0}\right]^{-n}, \quad (3.2)$$

where ρ_{rat} is the ratio between resistivity datasets, $\rho_{soil,0}$, ϕ_0, FPG_0, $\rho_{soil,t}$, ϕ_t and FPG_t are the resistivity, porosity, and free phase gas (FPG) content of the soil at time 0 and t, respectively. Eq. 3.2 thus provides a means of estimating changes in gas content with changes in resistivity between time-lapse datasets. *Terry et al.* [2016] suggest that while eq. 3.2 is useful for demonstrating the physical basis of the relationship between resistivity and FPG content, it is likely impractical and/or misleading to carry out a direct conversion from resistivity to gas content using field data given that reliable values for ϕ_0, FPG_0, and ϕ_t are difficult to establish over a relatively large 3D domain (several

meters). Furthermore, the smoothing carried out in the numerical inversion, as well as the decaying sensitivity of ERI away from the electrodes, may not provide realistic FPG values even if increases and decreases in ρ_{rat} are consistent with general increases and decreases in gas content. *Singha et al.* [2014] provide a review of methods for time-lapse analysis of ERI data in light of these challenges.

3.2.2 Accounting for pressure and temperature variations on gas content

In this study, we are primarily interested in changes in FPG content associated with production, transport, and release. However, FPG content will also vary with temperature and pressure in accordance with Henry's Law (HL) and the Ideal Gas Law (IGL). *Kellner et al.* [2008] provide equations linking changing FPG content to changes in temperature and pressure. For changes in temperature, the change in FPG content due to the IGL/HL ($\frac{\partial FPG}{\partial T}$) is,

$$\frac{\partial FPG}{\partial T} = \frac{FPG}{T} + \theta RT \times H_d(T)^2 \times \frac{\mathrm{dln}H_d}{\mathrm{d}(1/T)}, \tag{3.3}$$

where T is temperature (ºK), θ is the water content, R is the universal gas constant (= 8.314 J mol^{-1} ºK^{-1}), H_d is the Henry's Law solubility at standard temperature (mol J^{-1}), $\frac{dlnH_d}{d(1/T)}$ is the term describing the temperature dependence of the Henry's Law constant (ºK), and $H_d(T)$ is the Henry's law solubility corrected for temperature (mol J^{-1}). For a given temperature $H_d(T) = H_d \exp\left[\frac{\mathrm{dln}H_d}{\mathrm{d}(1/T)} \times \left(\frac{1}{T} - \frac{1}{298.15}\right)\right]$). *Sander* [2015] provides an extensive list of values for H_d and $\frac{\mathrm{dln}H_d}{\mathrm{d}(1/T)}$ for many different gas species. Methane

typically represents a considerable fraction of the FPG content in Caribou Bog, averaging 20% and as high as 51% based on 12 samples from 0.2 to 4.5 m depth (from gas samples described in this paper).. For simplicity, we assume free phase gas consists of CH_4 only and employ values of $\frac{\mathrm{dln}H_d}{\mathrm{d}(1/T)} = 1600$ ºK and $H_d = 1.4 \times 10^{-5}$ mol J^{-1} [*Sander et al.*, 2011].

The change in FPG content according to the IGL/HL for changes in pressure ($\frac{\partial FPG}{\partial P}$) is,

$$\frac{\partial FPG}{\partial P} = -\frac{FPG}{P} - \frac{\theta RT \times H_d(T)}{P}, \quad (3.4)$$

where P is pressure (Pa).

Thus the total variation in FPG predicted by the IGL/HL is,

$$FPG_t = FPG_0 + \Delta T \frac{\partial FPG}{\partial P} + \Delta P \frac{\partial FPG}{\partial T}, \quad (3.5)$$

Eq. 3.5 demonstrates that decreases in pressure and increases in temperature will increase the overall FPG content. By contrast, increased pressure and decreased temperature will decrease the overall FPG content without any bubble release.

3.2.3 Dielectric permittivity-water content relationship in peat soils

The *Topp et al.* [1980] empirical relationship is widely used to convert dielectric permittivity to water content in a variety of soils. This relationship is generally

unsuitable for peat soils given the typically very high water content of these soils. Multiphase mixing models such as the complex refractive index model (CRIM) consider the dielectric permittivity of individual components. A three phase mixing model has the general form:

$$\varepsilon_{r(b)}{}^{\alpha} = \theta\varepsilon_{r(w)}{}^{\alpha} + (\phi - \theta)\varepsilon_{r(g)}{}^{\alpha} + (1 - \phi)\varepsilon_{r(s)}{}^{\alpha}, \quad (3.6)$$

where $\varepsilon_{r(b)}$ is the bulk relative dielectric permittivity, $\varepsilon_{r(w)}$ is the relative dielectric permittivity of the liquid phase, $\varepsilon_{r(g)}$ is the relative dielectric permittivity of the gaseous phase, $\varepsilon_{r(s)}$ is the relative dielectric permittivity of the solid phase, and α is a fitting factor accounting for the orientation of electromagnetic waves to soil particles.

Parsekian et al. [2012b] calibrated several multiphase mixing models for peatlands including one specifically based on a lab study of Caribou Bog peat monoliths (α = 0.1, ϕ = 0.968). In *Parsekian et al.* [2012b], samples were kept in a laboratory at constant temperature and a single value for $\varepsilon_{r(w)}$ was used. In this study, however, temperature cannot be considered constant and we must further correct $\varepsilon_{r(w)}$. Here, we use the relationship [*Wheast,* 1979]:

$$\varepsilon_{r(w)}(T) = \varepsilon_{r(w)}(25) \times [1 - 0.4536 \times 10^{-2}(T - 25) + 0.9319 \times 10^{-7}(T - 25)^2], \quad (3.7)$$

where $\varepsilon_{r(w)}(25)$ = 78.34 is the relative dielectric permittivity at 25 °C.

3.2.4 Estimating biogenic gas content from GPR

Common midpoint (CMP) GPR surveys are used to estimate velocity variations in soils, and are well-documented as a means for inferring biogenic gas variations in peat

soils (i.e., *Comas et al.*, 2005; *Parsekian et al.*, 2011; *Wright and Comas*, 2016). Surveys are carried out by collecting measurements at fixed antenna separation increments surrounding a central point. In brief, strong reflectors will exhibit a characteristic hyperbolic pattern in a plot of radar two way travel time versus antenna separation, and these hyperbolae can be fit to an average velocity of the region above the reflector by assuming a raypath, where radar energy is redirected off of EM reflectors at the midpoint between the two antennas. Where multiple reflectors are present, the Dix equation can be used to convert average velocities to actual layer velocities [*Dix*, 1955]. Layer velocities can then be converted to dielectric permittivity using a low-loss assumption; a condition likely valid in Caribou Bog where electrical resistivity is typically greater than 100 ohm m (*Davis and Annan* [1989] suggest the low loss assumption is typically valid in soils with resistivity greater than 10 ohm m). Dielectric permittivity can then be converted to gas content using Eq. 3.6.

3.2.5 Biogenic gas production in peatlands

Peatlands form in waterlogged conditions where the buildup of organic matter exceeds the rate of biochemical breakdown. Complex organic matter is broken down through the processes of fermentation and hydrolysis to form methanogenic substrates such as acetate, CO_2, and H_2 [*Drake et al.*, 2009]. Where labile carbon and terminal electron acceptors such as nitrate, manganese, ferric iron, and/or sulfate are abundant, CO_2 is produced more readily during anaerobic respiration than CH_4; however where terminal electron acceptors are limited, production of CH_4 is favored [*Ye et al.*, 2012]. The efficiency of microbes in terms of producing biogenic gas is governed by the

interplay of factors such as temperature, water table position, pH, and nutrient supply [*Chasar et al.*, 2000a; *Paul et al.*, 2006; *Jaatinen et al.*, 2007; *Keller and Bridgham*, 2007]. Gases may then remain either trapped in the peat, participate in further chemical reactions, or be released to the atmosphere through diffusion, transport through vascular plants, and/or rapid ebullition. Therefore we expect to see that gas production is regulated by biogeochemical conditions within the peat, which are in turn determined by the parent material and nutrient inputs, while the transfer and release of FPG is controlled by physical forces such as peat structure, bubble volume, and pressure.

3.3 Methods

3.3.1 Study sites

This study was performed in the central unit of Caribou Bog, Maine, located between Pushaw Lake and the Penobscot River. Caribou Bog is a 2,200 ha ombotrophic peatland consisting of patterned pool and raised bog complexes [*Davis and Anderson*, 1999]. Peat ranging from 2 to 12 m thickness overlies a discontinuous layer of organic-rich lake sediment with thicknesses greater than 5 m in some locations [*Cameron et al.*, 1984; *Hu and Davis*, 1995; *Slater and Reeve* 2002; *Comas et al.*, 2004]. Initiation of the bog is estimated to have occurred between 8500 and 9000 before present [*Hu and Davis*, 1995; *Almquist- Jacobson and Sanger*, 1999]. The geology of the area consists of metamorphosed middle Ordovician to middle Devonian bedrock [*Osberg et al.*, 1985] overlain by the Presumpscot Formation. The Presumpscot Formation formed during the late Pleistocene and consists of glaciomarine silt-clay [*Bloom*, 1963].

We collected data at two sites within Caribou Bog with distinct characteristics (photographs and relative positions shown in Figure 3.1a). The first site is dominated by pools with an esker mineral soil (hereafter referred to as the 'pool and esker site' and shown in Figure 3.1b). By comparison to the surrounding peat, the esker deposit is highly permeable and is believed to facilitate groundwater exchange [*Reeve et al.*, 2009], which may in turn supply nutrients to microbes, driving more rapid peat decomposition and enhanced methanogenesis. The approximate location of the esker crest, inferred from *Comas et al.* [2011b] and located at approximately 2 m depth, is shown in Figure 3.1b. Surrounding the esker deposit, the mineral soil is an impermeable clay.

The second site is dominated by shrubs and small trees with a clay mineral soil and no esker deposit (hereafter termed the 'wooded heath site' and shown in Figure 3.1c). Without the permeable esker deposit, the impermeable clay underlying the wooded heath site prevents exchange of groundwater between the peat and mineral soil. Vegetation mainly consists of small-leaved *Sphagna* including *Sphagnum capillifolium* (Ehrh.) Hedw. and *Sphagnum fuscum* (Schimp.) Klinggr., and several ericaceous shrubs (mainly *Chamaedaphne calyculata* (L.) Moench, *Gaylussaccia baccata* (Wangenh.)**,** *Vaccinium* spp.). The surrounding areas are a typical Spruce forest (*Picea* spp, mostly *mariana* (Mill.) Britton, Sterns & Poggenburg) with interspersed Northern White Cedar (*Thuja occidentalis* L.).

3.3.2 Instrumentation and data collection timeline

Data collection at the field sites began in the summer of 2011 and ended in the fall of 2013. For the most part, we were unable to collect synchronous measurements at both sites due to logistics and lack of equipment. Given the difficulty transporting equipment between sites, the increased likelihood of upsetting natural FPG dynamics, and the increasing chance of errors introduced by slight changes in positions of the equipment, we deemed a single, comprehensive field campaign at both sites unfeasible and instead opted to carry out two separate intensive field campaigns on separate years, each focusing on a particular site. Although we understand the potential limitations of comparing biogenic gas dynamics at two different sites collected during two separate years it is important to consider that in both cases surveys were performed in a consistent manner during the time of the year when gas variability seems to be most pronounced in Caribou Bog. In a previous study that mimics the sites investigated in this study, *Comas et al.* [2008] measured gas content variability (i.e., increases and decreases) fluctuating between 4-12 % within the summer months of July and August, while most of the fall and winter were characterized by consistent periods of gas build up followed by a sharp decrease during the spring. The highest concentrations of data were collected at the pool and esker site during July-August, 2011, while most data were collected at the wooded heath site during July 2013. A timeline of data collection for both sites and years is shown in Figure 3.2, and an 'intensive study period' is marked corresponding to the four weeks when most data were collected at each field site. Hereafter, when comparing time-lapse data, we only refer to data collected during these intensive study periods. This is

primarily to make a direct comparison of the two sites more valid given the different time scales between data sets.

Layouts of the instrumentation at the pool and esker site and the wooded heath site are shown in Figure 3.1b and 3.1c, respectively. The instrumentation and data collection scheme varied somewhat between sites and years, but overall consisted of characterization by coring and GPR, peat deformation measurements, CH_4 flux measurements, time-lapse ERI, logging of atmospheric pressure and water levels, temperature logging at various depths in the peat, electrical resistivity monitoring at different depths, and soil moisture monitoring at various depths. To minimize our disturbance to the field sites and natural FPG dynamics, wooden platforms were constructed that were anchored to the sites' mineral soil.

3.3.2.1 2011 data collection

A Russian peat corer was used to gather peat samples from the surface to the mineral soil at 0.5 m depth increments in the location shown in Figure 3.1b on July 19, 2011. Von Post humification index was estimated along with notes regarding any unusual attributes of the core section. The von Post humification scale [*von Post*, 1924] is a field method for assessing the relative degree of peat decomposition with10 being entirely decomposed and 1 being the least decomposed.

A GPR common offset profile was gathered along a transect shown in Figure 3.1b. The GPR data were collected at 0.2 m trace increments using a Malå ProEx control

unit and 100 MHz antennas (Malå Geoscience, Sweden). GPR data underwent basic processing including dewow, divergence compensation gain, and bandpass filtering.

Peat deformation measurements were carried out using a Riegl Vz 400 3D terrestrial laser scanner (Riegl, Austria). Given the compressible nature of peat, the development of FPG within peat is coupled with an expansion of the peat itself [*Price*, 2003], although the expansion/contraction of peat may not accurately reflect changes in FPG due to expansion in x and y directions as well as the possibility of the presence of inelastic confining layers [*Romanowicz et al.*, 1995]. Nevertheless, variation in peat deformation may nonlinearly correlate with FPG content in peat.

Clusters of PVC elevation rods driven to specific depths in the peat (0.3, 1.5, 3.0, and 4.6 m) were placed at three locations in the pool and esker study area (as shown in Figure 3.1b). Each rod was fitted with a PVC tee fitting at the base, and rotated 90 degrees after insertion to lock the rod into the peat at the bottom of the rod so that relative changes in rod elevation reflect change in elevation of the peat at the bottom of the rod. Retroreflectors were fitted to the top of each deformation rod, which allowed the laser scanner to measure location and elevation of the top of the rod. The TLS was oriented to five static targets anchored to the mineral soil at the start of each measurement routine, and then location and elevation of deformation rod reflectors were determined. Using this configuration, changes in elevation of the peat at depth intervals (0.3, 1.5, 3.0, and 4.6 m), and therefore deformation within each interval (<0.3, 0.3-1.5, 3.0-4.6, and >4.6 m), were observed at each measurement time. Error was determined by finding the differences in elevation between static targets, with the highest observed vertical error being 0.012 m.

Gas flux measurement chambers were installed at both the pool and esker site and the wooded heath site in 2011. Chambers consisted of a bucket with a sawn off bottom (0.3 m diameter) driven a few cm below the peat surface and a PVC frame over which a plastic cover could be placed. An ambient air sample was drawn initially, then the cover was placed on the chamber and sealed at the bottom. Gas samples (typically 5 or 6) were drawn from sampling ports at consistent time intervals (usually every fifteen minutes) built into the cover by a syringe and then injected into evacuated vials for later analysis.

Limited gas sampling data (2 times per day for 2 days at the pool and esker site, 2 times per day for 3 days at the wooded heath site) were collected from the two chamber locations shown in Figure 3.1b and 3.1c from both sites. Figure 3.2a shows the timing of these measurements.

Atmospheric pressure and water levels were measured at the pool and esker site during 2011 by sensors attached to a GL500-7-2 logger (Global Water, Sacramento, CA, USA, location shown in Figure 3.1b). Data is available from this sensor before the period shown in Figure 3.2a but ended on September 8, 2011. Atmospheric pressure was measured by a WE100 sensor and collected at 15 minute intervals (Global Water, Sacramento, CA, USA). Water levels were recorded with a Global Water WL400 pressure transducer at 15 minute intervals and used vented cables to automatically compensate for atmospheric pressure variations. Hydraulic head (in m) recorded from this sensor was converted to water level below the peat surface by subtracting the instrument depth (0.7 m) from the recorded pressure at the sensor. Additionally, daily rainfall data were downloaded from the local weather underground station in Bangor, ME (KMEBANGO3, www.wunderground.com).

The electrical resistivity data and reciprocals were collected using an IRIS SYSCAL Pro Switch 72 electrode system (IRIS instruments, Orléans, France), with electrodes placed as in Figure 3.1b and consisting of 8 lines of 9 electrodes with 1.25 m intra-line spacing and variable spacing (3.5 to 5 m) between lines to accommodate a site platform and other instrumentation. Surveys consisted of 4,984 measurements in a mixed dipole-dipole and skip-7 array, which were collected approximately twice daily from July 27, 2011 to August 11, 2011 (see Figure 3.2a) and took roughly 1.25 hours to collect. In total, 24 datasets were collected.

Two sets of 4 vertical temperature sensors (HOBO pendant loggers, Onset, Bourne, MA, USA) were placed at 0, 0.6, 0.18, and 0.24 m depth within the ERI monitoring region at the positions shown in Figure 3.1b. The purpose of these loggers was mainly to correct ERI results for temperature variations and thus were installed for the time period corresponding to ERI data collection (Figure 3.2a). These data were recorded at hourly intervals throughout the study period.

Decagon 5TE probes (Decagon Devices, Pullman, WA, USA) were used to monitor θ, temperature, and electrical conductivity at five depths (0.5, 1.0, 2.0, 3.0, and 4.0 m) at the pool and esker site during 2011 (location shown in Figure 3.1b) during the time period shown in Figure 3.2a. Data were logged at 10-minute intervals for each probe.

One set of gas samples were collected from traps installed near the site (location shown in Fig. 3.1b, relative time of collection shown in Fig. 3.2a). Gas traps consisted of 2 inverted plastic tubs (length = 30 cm, width = 20 cm, depth = 10 cm) set into a cut out section of peat. Peat was removed from the top 30 cm (below the water table), and the

edges of the tub were driven into the peat below such that gas bubbles would collect and be visible in the bottom of the tub. Captured bubbles were sampled with a GEM2000 gas extraction meter (Landtec, Colton, CA, USA) for CH_4, CO_2, CO, and H_2S.

3.3.2.2 2013 data collection

Similar to data collection at the pool and esker site in 2011, a Russian peat corer was used to gather peat samples at 0.5 m increments from the location shown in Figure 3.1c on July 2, 2013. Photographs of the samples were taken along with any notes of unusual characteristics observed (such as bubbling or presence of large wood fragments). The level of von Post decomposition was assessed for each core section.

A GPR common offset transect corresponding to Figure 3.1c was gathered on July 2, 2013. GPR data were collected using the same acquisition parameters as at the pool and esker site. Basic processing of the GPR transect data was also the same as at the pool and esker site.

In addition, two 100 MHz GPR common midpoint (CMP) datasets were collected near each site platform on July 12, 2013. Antenna separation was increased by 0.1 m out to 4.5 m total separation. After applying the same basic processing steps used for common offset GPR, we used ReflexW software to manually pick 4 identifiable reflectors at each site and thus estimate velocity in 4 layers at each site. Layer velocities were converted to dielectric permittivity using the low loss approximation, then to gas content assuming a ϕ value of 0.925 (the average from 6 samples taken from Caribou Bog [*Comas et al.*, 2005]) and employing Eq. 3.6.

Atmospheric pressure variations were recorded in 2013 by an atmospheric pressure sensor (Hydroinnova, Albuquerque, NM, USA) at 1 hour intervals located at the

wooded heath site. The location of this sensor is shown in Figure 3.1c. Data available from this sensor extends before and beyond the time shown in Figure 3.2b.

Relative water levels at the wooded heath site were monitored during 2013 by a Solinst LevelLogger Junior 3001 water level sensor (Solinst Canada Ltd., Georgetown, ON, CAN) placed in a screened well (driven to approximately 1 m depth) at the wooded heath site, which logged data at 2 minute intervals (location shown in Figure 3.1c). Data were available for the entire 2013 monitoring period in Figure 3.2b as well for some time before and after the intensive measurement campaigns. Water levels were compensated for atmospheric pressure variations using a Solinst Barologger Edge 3001 positioned at the surface. Relative water levels were converted to absolute water levels by calibrating a field measurement to a sensor measurement at the same date and time.

ERI data and reciprocals were collected at the wooded heath site using the same instrumentation and data collection scheme as the pool and esker site, as shown in Figure 3.1c. However, improvements in the power supply (including acquisition of a solar array as well as several extra batteries) enabled us to automate the ERI monitoring to extend data collection beyond the main field campaign for a total of 127 datasets (July 4 – August 28, 2013; shown in Figure 3.2b). On average, data were collected every 12 hours, although more rapid data collection (as frequently as every 2 hours) occurred during select periods of the main field campaign in July, 2013. In addition, 8 HOBO pendant style temperature loggers were installed within the ERI array region at 0, 0.8, 1.6, 2.4, 3.2, 4.0, 4.8, 5.6, and 6.4 m (position shown in Figure 3.1c and time corresponding to ERI data collection), mainly to correct resistivity values for temperature variation.

Decagon 5TE probes were placed in the location shown in Figure 3.1c and were used to monitor θ, temperature, and electrical conductivity at four depths (0.3, 1.0, 3.0, and 4.5 m) at the wooded heath site during 2013, sampled in 15 minute intervals at each probe. Data were logged from these probes for a much greater length of time than at the pool and esker site in 2011 (compare Figure 3.2a and 3.2b) due to equipment availability.

Deformation measurements at the wooded heath site during 2013 employed a similar design of deformation rods used in 2011, with rods driven to 1.5, 3.0 and 4.6 m depths. A simplified measurement system was used to measure relative deformation, where the top of each rod was fitted with a measurement scale, and readings were taken using a dumpy sight level and differential leveling techniques. Measurements were referenced to two benchmark rods driven to mineral soil. The maximum amount of error observed (changes in difference of elevation between benchmarks) yielded an accuracy within 0.002 m.

Chamber flux measurements were performed only at the wooded heath site during 2013. A total of 55 CH_4 flux (typically 4 per day) measurements were collected during July 2013.

Limited gas samples were collected from traps installed near the site using a method similar to *Comas and Wright* [2012]. Gas traps consisted of pvc tubing driven to 0.3 m, 3.0 m, and 4.5 m depth. The bottom of the tubes consisted of a funnel (with an opening of approximately 284 cm^2) to collect bubbles from peat, and a sealed clear plastic casing at the top with an extraction port. The gas traps at the wooded heath site were additionally outfitted with a measuring tape along the tube and a time-lapse camera (TimelapseCam 8.0, Wingscapes, Calera, AL, USA) that photographed the elevation of

fluid in the tubes at 15 minute intervals. Captured gas from each trap was sampled twice during the field campaign with a GEM2000 gas extraction meter (Landtec, Colton, CA, USA) for CH_4, CO_2, CO, and H_2S.

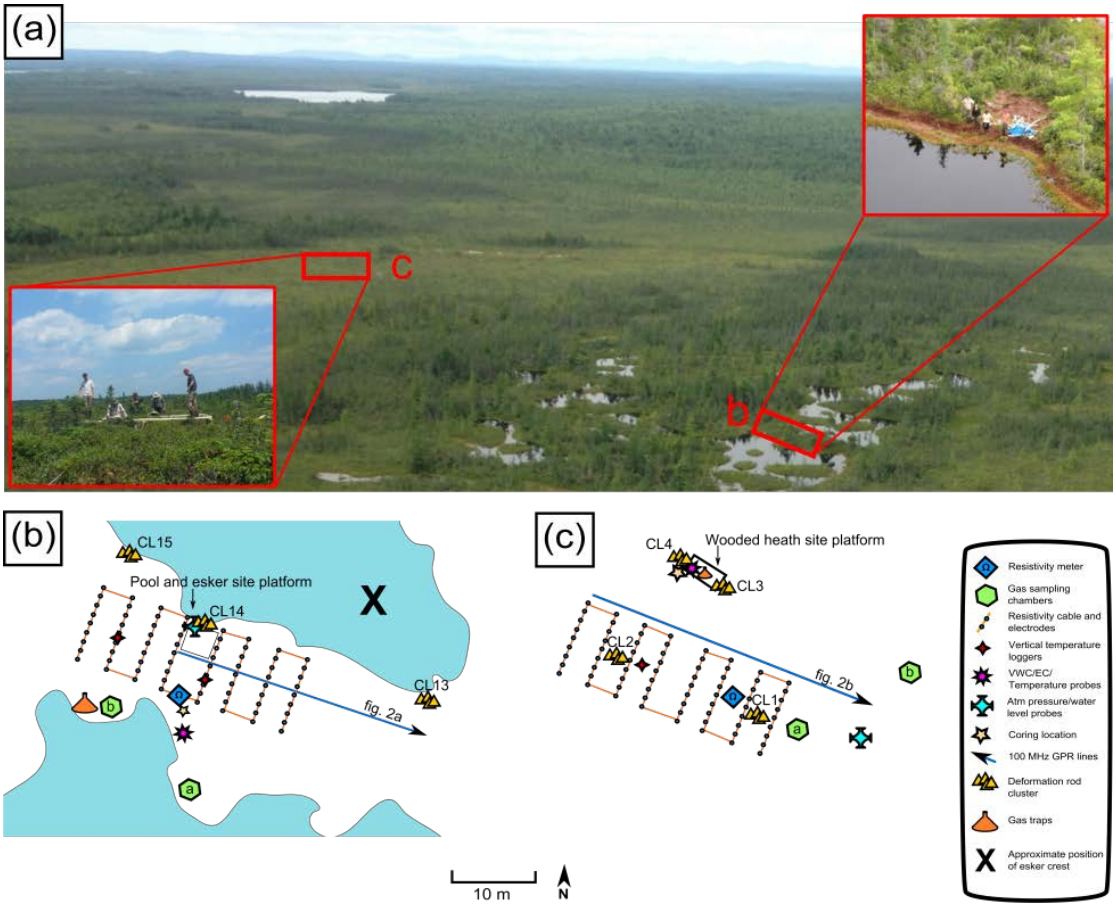

Figure 3.1 – (a) oblique aerial photo (photograph by author, 2013) showing relative locations of the pool and esker site (photo by William Wright, 2013) and the wooded heath site (photo by Barbara Goldman, 2013); (b) schematic representation of equipment at the pool and esker site; (c) schematic representation of equipment at the wooded heath site. The location of the GPR common offset profiles shown in Figure 3.3 are also shown in (b) and (c).

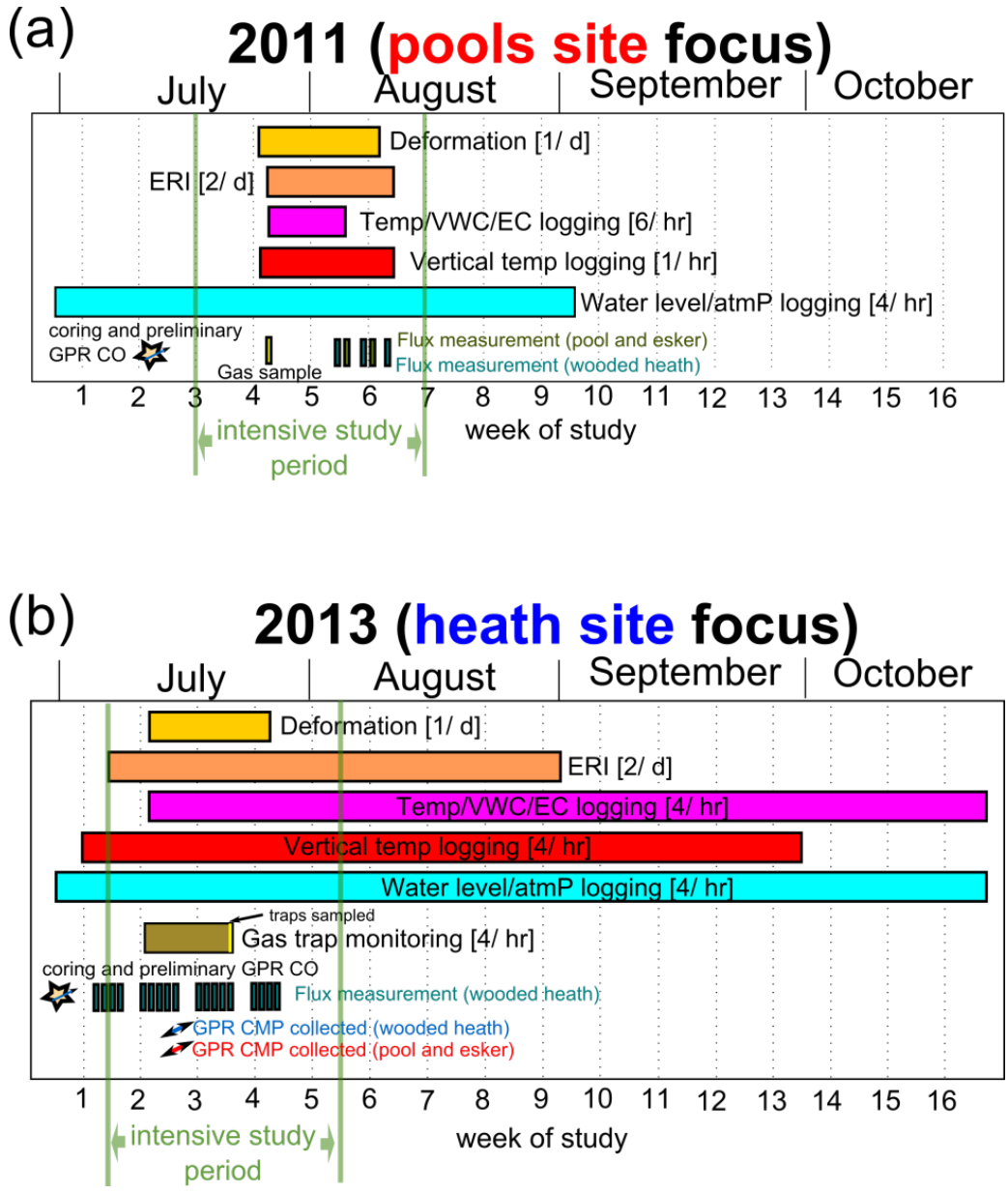

Figure 3.2 – Gantt charts showing timeline for collection of various data during (a) the 2011 field campaign at the pool and esker site with limited chamber flux data at the wooded heath site and (b) the 2013 field campaign at the wooded heath site. Approximate data collection frequencies are shown in square brackets, and periods of intensive study are enclosed by green bars.

3.3.3 Soil moisture conversion to gas content

The θ values provided by the 5TE probes are automatically calculated by converting raw $\varepsilon_{r(b)}$ measured by the probes through the *Topp et al.* [1980] equation. To employ the mixing model specific to Caribou Bog, peat samples from each site were collected and analyzed in the lab to develop a relationship between θ and raw values from the 5TE probes (mV). For each site, water was added (0 to 12 mL) to 6 samples (each 116 cm^3) with a 5TE probe installed. Measurements from the probes were recorded and the samples were weighed, oven dried, then weighed again to establish volumetric water content. A linear calibration curve for each site was established as follows: (1) pool and esker site $\theta = 4 \times 10^{-5}x + 0.6934$ (R^2 = 0.99) and (2) wooded heath site $\theta = 1 \times 10^{-5}x + 0.7212$ (R^2 = 0.99), where x is the raw probe output.

The 5TE calculated θ values were further corrected for temperature by back calculating $\varepsilon_{r(b)}$ through eq. 3.6 and correcting the $\varepsilon_{r(w)}$ term for temperature variations according to Eq. 3.7. Values for equation 3.6 were $\varepsilon_{r(s)}$ = 2 (*Comas et al.*, 2005); $\varepsilon_{r(g)}$ = 1, α = 0.1 (*Parsekian et al.*, 2012b), and ϕ = 0.94. Gas content is given as $\phi - \theta$.

Likely, porosity values vary somewhat at different depths and between sites, however we did not collect detailed porosity information during this study due to time constraints.

3.3.4 ERI data processing

Time-lapse analysis of ERI datasets followed the approach of *Terry et al.* [2016]. Basic filtering applied to the ERI data included removing measurements with (1) > 25 % reciprocal error, (2) a negative resistivity, or (3) an applied current or measured voltage

of less than 1 millivolt or 1 milliAmp. Measurements failing to meet these criteria were removed from the entire time series for consistency in time-lapse inversion. Each dataset underwent error analysis using the method of *Koestel et al.* [2008] to construct an error model – a linear model was selected for both sites with slightly higher error levels at the pool and esker site. Error levels were relatively low and are consistent with the low electrical noise environment enjoyed in our remote field locations. There were 2,876 measurements for each data collection time remaining after this filtering.

Time-lapse ERI data were prepared for inversion following the approach of *Labrecque and Yang* [2001]. Data were inverted in R3t (A. Binley, Lancaster University) using the same finite element mesh (47,722 elements) and inversion options (smoothness constraint and singularity removal) for each site. An initial background dataset was inverted using a 100 ohm m starting model. Subsequent inversions used the previous inverse result as a starting model, and reduced error levels (scaled to 25%) to allow for convergence. The original errors propagated to the time-lapse datasets assume that these errors are uncorrelated, while in reality these errors are likely largely systematic (see discussion in *Labrecque and Yang* [2001]). Inverted models were corrected for temperature variations (both with depth and through time) using peat temperature data from each site. We assumed no horizontal variation in temperature to construct 1D temperature spline models for each time step following the approach of *Hayley et al.* [2007].

3.3.5 Flux data analysis

Chamber fluxes were computed by taking gas samples from closed chambers at fixed time increments (typically 5 or 6 samples with 10 to 20 minute sampling increments). The samples were collected via syringe into prevaccuumed 20 mL glass vials. These samples were later analyzed using a gas chromatograph (GC, Shimadzu, GC-8A, Japan) and converted to CH_4 concentration. CH_4 flux is the slope of the line, fitting time versus CH_4 concentration, divided by the footprint of the chamber. Poor regression fits indicate non-steady flux [*Altor and Mitsch*, 2006]. For the purposes of this study, we considered regressions with R^2 values of less than 0.8 to indicate non-steady flux.

3.4 Results

3.4.1 Comparison of site characteristics

Observations recorded while coring are summarized in Figure 3.3. In general, the core at the pool and esker site (Figure 3.3a) shows little decomposition in the shallow peat (H1 – H3) that is gradually increasing to a high level of decomposition deeper below 3 m into the peat (H6 – H9). Interestingly, the wooded heath site (Figure 3.3b) shows overall less decomposition (between H3-H6), and an opposite pattern of relatively low decomposition at depth and relatively higher decomposition in the shallow peat. Large wood fragments (> 1 cm) were encountered during coring at both sites, although small roots and undecomposed material were more prevalent at the wooded heath site. In addition, a large bubbling event was observed at the wooded heath site when the corer punctured peat fabric at 1.5 m depth.

The GPR profiles corresponding to Figure 3.1d and 3.1e are shown in GPR Figure 3.3a and 3b. Root mean square EM wave velocities of the peat established from corresponding common midpoint analysis applied to the mineral soil (not shown) were 0.0378 m/ns at the pool and esker site and 0.0384 m/ns at the wooded heath site. These velocities are consistent with ranges previously reported for Caribou Bog (i.e., *Comas et al.*, 2011b). GPR data further highlight distinct structural differences between the two sites. The pool and esker site (Figure 3.3a) depicts a distinctive reflection from the esker deposit (cresting toward the eastern side) and laterally inconsistent reflections throughout the rest of the radargram that appear chaotically. Meanwhile, the wooded heath site (Figure 3.3b) shows a more subparallel structure with several apparently laterally continuous reflectors appearing in the image, one of which corresponds to large wood debris encountered during coring (at 3.75 m depth). Another distinct reflector occurs at 5.5 m that does not correspond to compositional changes encountered during coring.

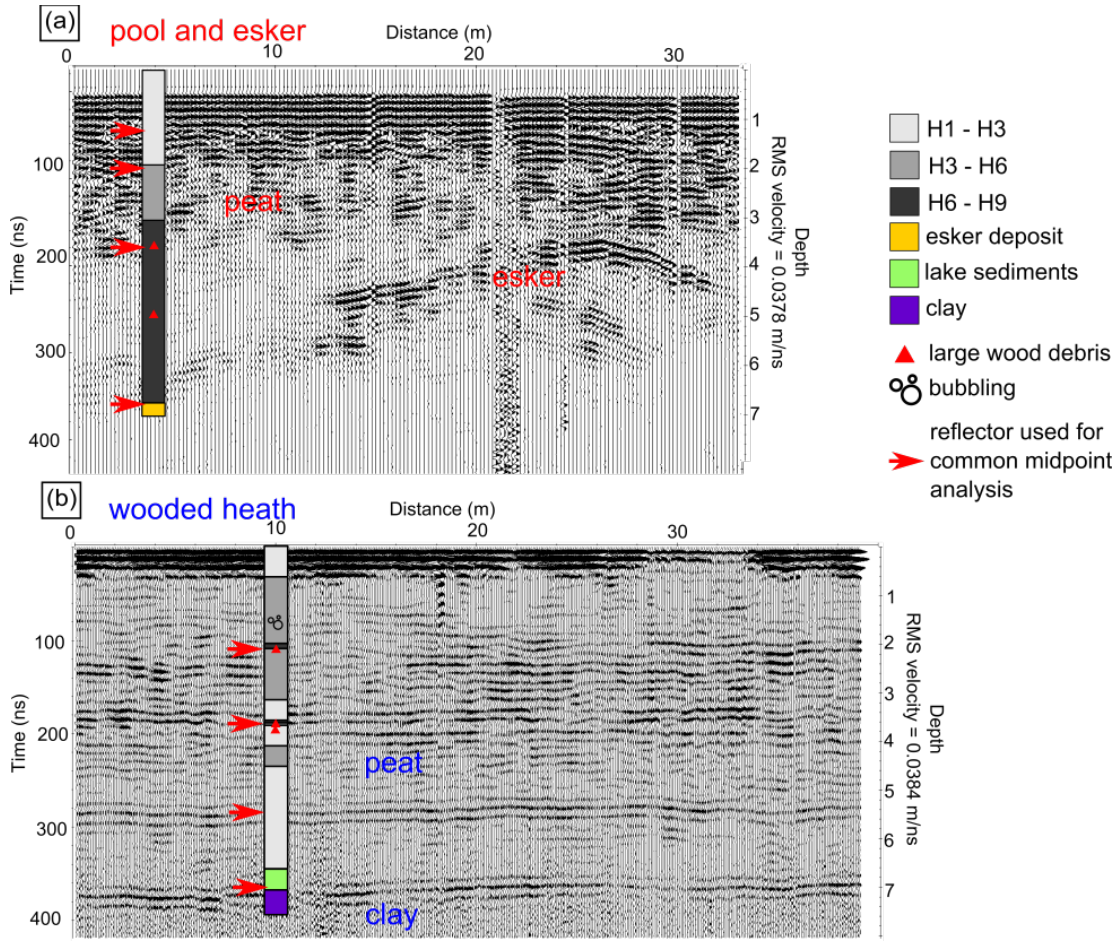

Figure 3.3 – comparison of 100 MHz common offset GPR data from (a) the pool and esker site and (b) the wooded heath site. Von Post decomposition, mineral soil material, and the presence of large wood from cores at each site are also shown. RMS velocity for each figure is based off of CMP analysis.

Fence diagrams of temperature corrected background ERI inversion results from the pool and esker site and the wooded heath site are shown in Figure 3.4a and 3.4b, respectively. Immediately evident from the images are a relatively high resistivity anomaly (500 – 1000 ohm m) at depth corresponding to the esker deposit (consistent with values published by *Comas et al.*, [2004]) at the pool and esker site, and the relatively low resistivity anomaly (30 – 50 ohm m) at depth corresponding to the silt-clay mineral

soil at the wooded heath site. The images further highlight the distinctly different physical properties of the peat, as well as the underlying mineral soil, at the two sites.

Averaged resistivity values (taken from the black cylinder region of Figure 3.4a and 3.4b) for both sites are shown as depth profiles in Figure 3.4c. The upper 4 m of peat at the wooded heath site has, on average, a higher resistivity than at the pool and esker site (150 – 225 ohm m versus 125 – 175 ohm m). Below 4 m, resistivity at the wooded heath site decreases gradually to around 50 ohm m, whereas resistivity increases gradually at the pool and esker site to around 200 ohm m. Another notable characteristic of resistivity profile shown for the wooded heath site in Figure 3.4c is the sudden increase at approximately 3 m (225 ohm m as opposed to 180 ohm m directly above and below).

Average, minimum, and maximum gas content during the intensive study periods of both sites is shown in Figure 3.4d. Gas content from the wooded heath site (blue line) is consistently higher than that of the pool and esker site, in agreement with the higher resistivity values also recorded at this site in the 0 – 4.0 m region (Figure 3.4c). The wooded heath site also depicts a generally decreasing gas content with depth, whereas the pool and esker site shows the highest average gas content at 3 m depth.

Gas contents derived from the permittivity estimates from the GPR CMPs are shown in Figure 3.4e. Again (compare to Fig. 3.4d) gas content is typically higher at the wooded heath site, although the 1.0 to 2.5 m appears gassier at the pool and esker site. Compared to the values recorded at the 5TE probes (Fig. 3.4d), GPR CMP derived gas content shows a wider range, varying between 1 % and 6.5% at the pool and esker site (compared to 4 – 6.5 %), and between 5 % and 11% at the wooded heath site (compared to 13.8 – 15 %). It is important to note here that the difference in sampling volume

between GPR and the probes (i.e., depth intervals in peat on the order of m^3 versus a small area ~ 1 cm^3 surrounding the probes).

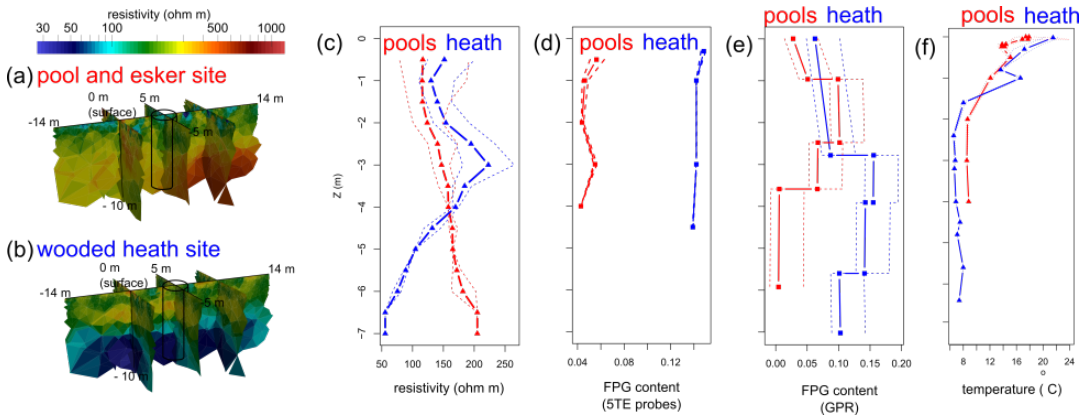

Figure 3.4 – comparison of inverted resistivity values at (a) the pool and esker site, (b) the wooded heath site, and integrated resistivity values drawn from various depth levels drawn from the center of the study area (indicated as black cylinder in (a) and (b) and plotted as triangles in (c). Resistivity values from the pool and esker site are shown as red triangles in (c), while resistivity values from the wooded heath site are shown as blue triangles in (c). Dotted lines indicate upper and lower values from each depth level in the integration area while solid lines indicate the mean. (d) Average gas content from the 5TE probes (solid lines), maximum and minimum values during the intensive study periods (dotted lines) for the pool and esker site (red) and the wooded heath site (blue). (e) Gas content derived from CMP analysis of GPR data, solid line shows values calculated from 92.5% porosity, dotted lines show uncertainty for porosity ranging from 91% to 96.8%. (f) Temperature profiles from the HOBO and 5TE sensors; dotted lines indicate maximum and minimum values during the respective intensive study periods at each site.

3.4.2 Time lapse data

3.4.2.1 Atmospheric pressure, water levels, rainfall, and peat temperature

Atmospheric pressure, daily rainfall, and water levels for the 2011 intensive study period at the pool and esker site as well as the 2013 intensive study period at the wooded heath site are presented in Figure 3.5a and 3.5b, respectively. Drops in atmospheric pressure are associated with rainfall events and subsequent water table rise. Water levels at the pool and esker site in 2011 generally rise and range from 0.26 m to 0.16 m depth throughout the study period, whereas water levels generally fall and vary between 0.20 to 0.12 m depth at the wooded heath site during 2013.

Atmospheric pressure varied from 993 to 1021 hPa during the 2011 intensive study period. Atmospheric pressure during the 2013 intensive study period varied from 996 to 1023 hPa. Each study site experienced several atmospheric pressure minima, most often coupled with rainfall events, during the respective study periods.

Peat temperature shows the greatest variation at shallow depths (Fig. 3.4f, dotted lines) at both sites and on average decreases with depth. Extreme temperature values recorded from the peat surface to the mineral soil range from 6 to 26 °C are observed at the wooded heath site, whereas the temperature range for the pool and esker site (from the peat surface down to 4.5 m depth) varied from 8.5 to 23 °C. Peat temperature is higher at the wooded heath site above 1.5 m depth on average, while the peat below 1.5 m is cooler during the study period (Fig. 3.4f).

3.4.2.2 Gas content

Gas content estimated from the 5TE probes for the pool and esker site and the wooded heath site are shown in Figure 3.5. Figure 3.5a shows the actual calculated gas

content at each of the five probe depths at the pool and esker site. The degree of variability in gas content decreases with depth at the pool and esker site (with one exception – the 3.0 m probe shows higher gas content and more total variation than the 2.0 m probe). The most variability (ranging from 5.1% to 6.3%, with a standard deviation of 0.3%), and ultimately the largest recorded gas content, is observed at the shallowest probe (0.5 m depth), followed by the 1.0 m probe (ranging from 4.4 % to 4.9 % gas content, with a standard deviation of 0.1 %), the 3.0 m probe (ranging from 5.4 % to 5.7 %, with a standard deviation of 0.1 %), the 2.0 m probe (range = 4.3 % to 4.5 %, standard deviation of < 0.1 %), and finally the 4.0 m probe (steady at 4.3 %). Meanwhile, peat temperature increases slightly at the 0.5 m and also at the 1.0 m probe (~ +1 °C Fig. 3.5c), and very slightly increases at the 2.0, 3.0 m probes, (+0.3 °C, +0.1 °C respectively), and remains steady at 8.8 °C at the 4.0 m probe.

Gas content at the wooded heath site (Figure 3.5b) was generally higher but showed less variability than at the pool and esker site. Additionally, gas content decreased with depth (as seen in Figure 3.5d). The shallowest (0.3 m) probe recorded a range of 14.6 % to 15.0 % gas content (standard deviation = 0.1 %), the 1.0 m probe recorded from 14.1% to 14.2% (standard deviation << 0.1 %), the 3.0 m probe recorded similar values ranging from 14.1 % to 14.2 % again with a standard deviation of << 0.1 %, and the deepest (4.5 m) probe recorded 13.8 % to 13.9% gas content (with a standard deviation of << 0.1 %).

At the pool and esker site, calculated changes in gas content due to pressure and temperature fluctuations (eq. 3.5) are small relative to overall gas content changes, where the change in gas content due to changes in peat temperature and atmospheric pressure

variations only accounts for approximately 0.1 – 0.2% variation in gas content at each of the probes. At the wooded heath site, however, changes predicted due to temperature and pressure variations are greater than the actual changes measured at the probes at all locations. The 0.3 m probe at the wooded heath site has theoretically the greatest variation (0.7 %), due to the larger temperature fluctuations experienced at this probe compared to those in deeper layers. The total variations calculated for the 1.0, 3.0, and 4.5 m probes were 0.6%, 0.5%, and 0.4%, respectively.

Sudden variations in gas content occur often in the 0.5 and 1.0 m probe at the pool and esker site, as well as the 0.3 m and 1.0 m probes at the wooded heath site. For example, Figure 3.5c and 3.5d show the gas content for a limited time period from both sites (for direct comparison and better visibility). The pool and esker site shows 4 sudden increases in gas content at the 0.5 m (+0.5 %) and 1.0 m probe (+0.25 %) that correspond to pressure drops and or water level rise, which are followed by gradual decreases (roughly 1 day or less) in gas content approximately back to pre-event levels (Figure 3.5c). The sudden increases at the pool and esker site appear to be accompanied by very small decreases in gas content at the 3.0 m probe (~ -0.1 % gas content). The wooded heath site shows three sudden decreases in gas content at the 0.3 m probe during 2 atmospheric pressure drops (~ -0.1 % gas content), with small increases and decreases (+/- 0.05 %) at the 1.0 m probe (Figure 3.5d). Though it may seem unrealistic to monitor such small changes in gas content (i.e., +/- 0.05 %), propagating the error reported for the raw values recorded by the 5TE probes (+/- 15% for dielectric permittivity in the range of 40-80) to gas content indicates an achievable accuracy of +/- 0.04% and +/- 0.01% gas content for the pools site and wooded heath site, respectively.

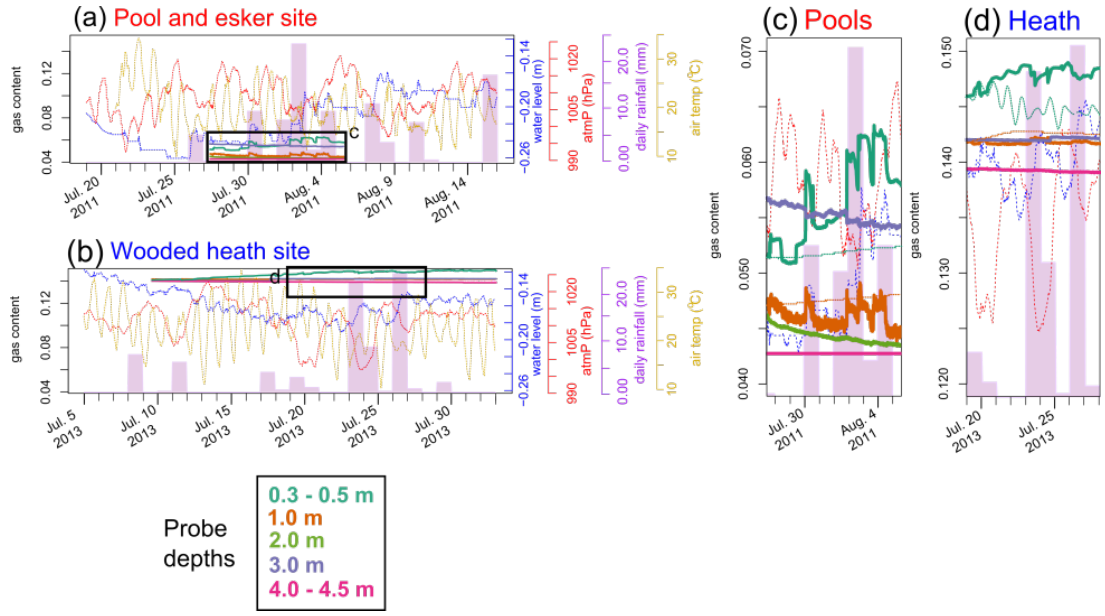

Figure 3.5 – gas content measured at the moisture probes at (a) the pool and esker site and (b) the wooded heath site. Atmospheric pressure variations are shown in (a) and (b) as dotted red lines, water levels are shown as dotted blue lines, surface temperature variations are shown as the dotted gold lines, and daily rainfall is indicated by semitransparent purple bars. (c) and (d) show specific time periods and gas content ranges from the pool and esker site in 2011 (c) and the wooded heath site in 2013 (d). Relative changes in atmospheric pressure are indicated by dotted red lines, while relative water levels are indicated by dotted blue lines and relative daily rainfall amounts are indicated by semitransparent purple bars. Relative peat soil temperature at the two shallowest probes for each site are also shown as dotted lines of the corresponding color of the probe depth in c and d.

3.4.2.3 Peat deformation

Figure 3.6a-3.6c shows the relative (to the minimum elevation observed) peat deformation from 4 depths at three different locations within the study area at the pool and esker site during 2011 (locations shown in Figure 3.1d). These values (up to 3 cm) are consistent with previous measurements made at the site using elevation rods [*Comas et al.*, 2008], as well as those observed in other northern peatlands [*Glaser et al.*, 2004]. Deformation data shows more deformation in all layers at a cluster to the east, associated with proximity to the esker crest.

Figure 3.6e-3.6h shows relative deformation at 3 depths at the wooded heath site at the four clusters shown in Figure 3.1e during the 2013 study period. The overall deformation is very small (3-4 mm) as opposed to up to 3 cm deformation at the pool and esker site (Figure 3.6c).

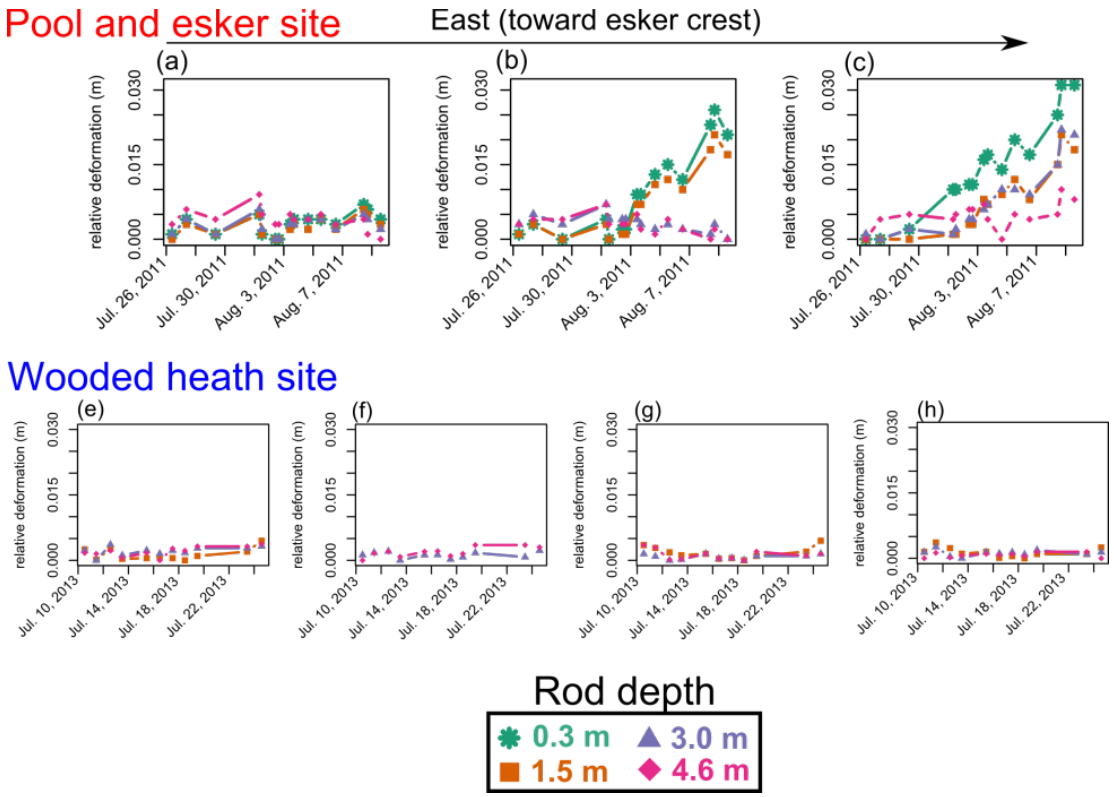

Figure 3.6 – relative (to data minimum) deformation at the three rod clusters from the pool and esker site throughout the 2011 study period corresponding to CL15 (a), CL14 (b), and CL13 (c) as shown in Figure 3.1d. (e-f) show relative (to data minimum) deformation corresponding to four rod clusters at the wooded heath site corresponding to CL1 (e), CL2 (f), CL3 (g), and CL4 (h) as shown in Figure 3.1e. Colored lines indicate the deformation relative to starting values of each rod in the cluster and legend indicates the depth of the bottom of the rod.

3.4.2.4 Direct gas measurements: gas traps and chamber fluxes

Gas buildup in three traps at the wooded heath site during the monitoring period (Fig. 3.2b) is shown in Figure 3.7a. Little to no buildup was observed between installation on July 9 and July 11. On July 12, a small (roughly 10 cm^3) increase was observed. On July 13, an additional 90 cm^3 of gas appeared in the 4.5 m trap, followed by an additional 50 cm^3 on July 14 and another 50 cm^3 on July 15. The 3.0 m trap

showed a small increase (~ 5 cm^3) on July 13, then a single large (roughly 100 cm^3) increase on July 15. The shallow 0.3 m probe showed a single large increase of approximately 80 cm^3 on July 16.

Gas sampling of the gas built up in the traps at the wooded heath site took place on July 17, 2013; CH_4 % and CO_2 % by volume are shown in Figure 3.7 b and c, respectively. The CH_4 content ranges from 11.4 % to 44 % and increases linearly with depth. The CO_2 content ranges from 4.1 % to 11.7 % and also increases linearly with depth. Other gases measured by the meter (H_2S, CO) occurred in very small proportions (< 0.5 % by volume).

The single gas sample collected from 0.5 m depth at the pool and esker site is also plotted in terms of CH_4 and CO_2 content in Figure 3.7b and 3.7c, respectively. The sample indicated 33.3% CH_4 content and 4.3 % CO_2 content at this site and depth. Additional CH_4 samples taken from the pool and esker area by *Parsekian et al.* [2011] for the 1.75 – 3.00 m depth range are also plotted in Fig. 3.7b. The highest recorded CH4 content (52%) occurs at 3 m depth. Thus, while both sites appear to have similar CO_2 content in the shallow peat (i.e., 0.3 – 0.5 m), the pool and esker site appears to have elevated CH_4 throughout the sampled depths.

Figure 3.7d shows a bar chart comparing CH_4 chamber fluxes measured at both sites. Although fewer measurements were available for the pool and esker site, larger overall fluxes are evident (average = 11 mg m^{-2} hr^{-1}, maximum = 28 mg m^{-2} hr^{-1}) compared to the wooded heath site (average = 2 mg m^{-2} hr^{-1}, maximum = 14 mg m^{-2} hr^{-1}).

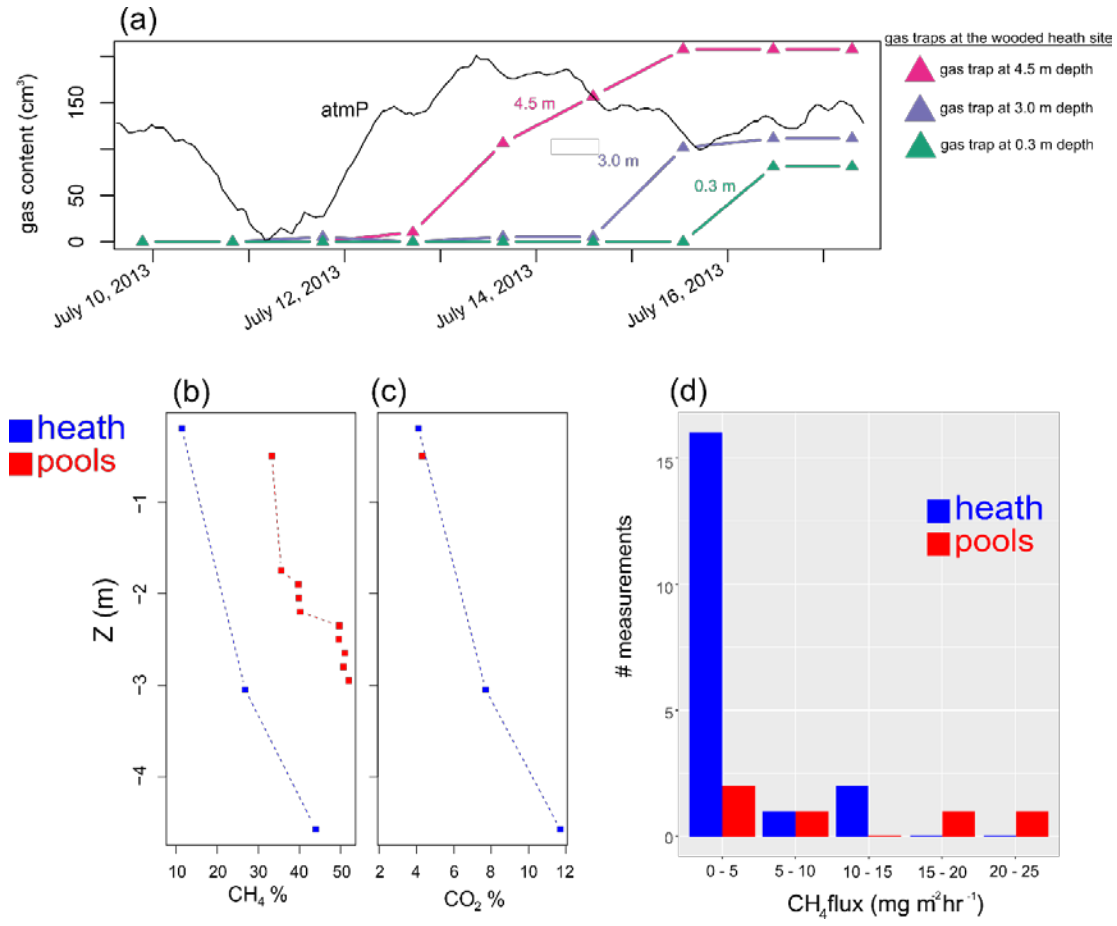

Figure 3.7 – (a) gas buildup at each of the gas traps at the wooded heath site during 2013 through the study period, with relative atmospheric pressure variation shown as black line. (b) and (c) show the proportions of CH_4 and CO_2 respectively at the time of sampling (July 17, 2013). Gas was only sampled one time at one depth at the pool and esker site during 2011 and is represented by the red square in (b) and (c). (d) bar chart showing the number of CH_4 fluxes of binned magnitudes measured at the pool and esker site (red) and the wooded heath site (blue).

3.4.2.5 Electrical Resistivity Imaging

Average ratio of resistivity from four depth zones from each time series are shown in Figure 3.8. The time series have been interpolated to one hour time steps using a Gaussian smoother in an attempt to make densely sampled portions of the time series comparable to less densely sampled portions. The dominant changes in resistivity at the pool and esker site (Figure 3.8a) occur below 1.0 m, whereas resistivity changes at the wooded heath site are seldom observed in this region, and much more often witnessed in the shallow 0.3 to 1.0 m peat (Figure 3.8b).

Although the wooded heath site shows a single ratio resistivity decrease event (corresponding to Figure 3.9h) from the shallow (0.3 to 1.0 m) zone that is slightly larger in magnitude than any of the events observed at the pool and esker site, the pool and esker site typically exhibits more activity throughout the peat profile, particularly in the 2.0 – 6.4 m zones in the eastern region of the study area. In addition, large events (showing ratio resistivity changes of greater than 0.002/hr) occur at a higher frequency at the pool and esker site.

Figure 3.9 shows select images from each ERI time series. The images have a threshold applied to only show voxels with resistivity changes of greater than 0.002 ohm m/hr. ERI data from each site show a number of significant events. The pool and esker site exhibits more activity over the esker region (Figure 3.9b and 3.9c) and in general shows increases and decreases in gas content throughout the peat profile. On the other hand, the wooded heath site typically shows activity that is more or less laterally contiguous and in general shows far fewer decreases in resistivity in regions deeper than 1 meter.

Select images from the pool and esker site are shown in Figure 3.9a – 3.9d. The event displayed in Figure 3.9a shows increases in resistivity in the top 4 m, and decreases below. Figure 3.9b and 3.9c shows activity primarily in the esker region, however Figure 3.9b consists of resistivity increases in the 0.3 to 1.0 m and 4.0 to 6.4 m range (shallow and deepest) with resistivity decreases in the middle depths (1.0 m to 4.0 m), whereas Figure 3.9c shows mixed resistivity increases and decreases, but on average decreases from all depths. Figure 3.9d shows resistivity decreases from all depths.

ERI images from the wooded heath site are shown in Figure 3.9e – 3.9h. The image in Figure 3.9e shows resistivity increases in the 0.3 – 1.0 m and 2.0 - 4.0 m zone, but decreases in the 1.0 – 2.0 m zone. Figure 3.9f shows predominantly increases in gas content in all layers (see Figure 3.8b). The event in Figure 3.9g shows a resistivity decrease in the peat from 0.3 to 1.0 m, a slight increase in the 1.0 – 2.0 m region, and slight decreases below. Note that the patterns in the regions below 1.0 m are not visible in the images due to the threshold. Finally, the event in Figure 3.9h shows a large decrease in resistivity in the 0.3 – 1.0 m peat region, as well as smaller decreases in the 1.0 – 4.0 m peat region, and increases in the 4.0 – 6.4 m region.

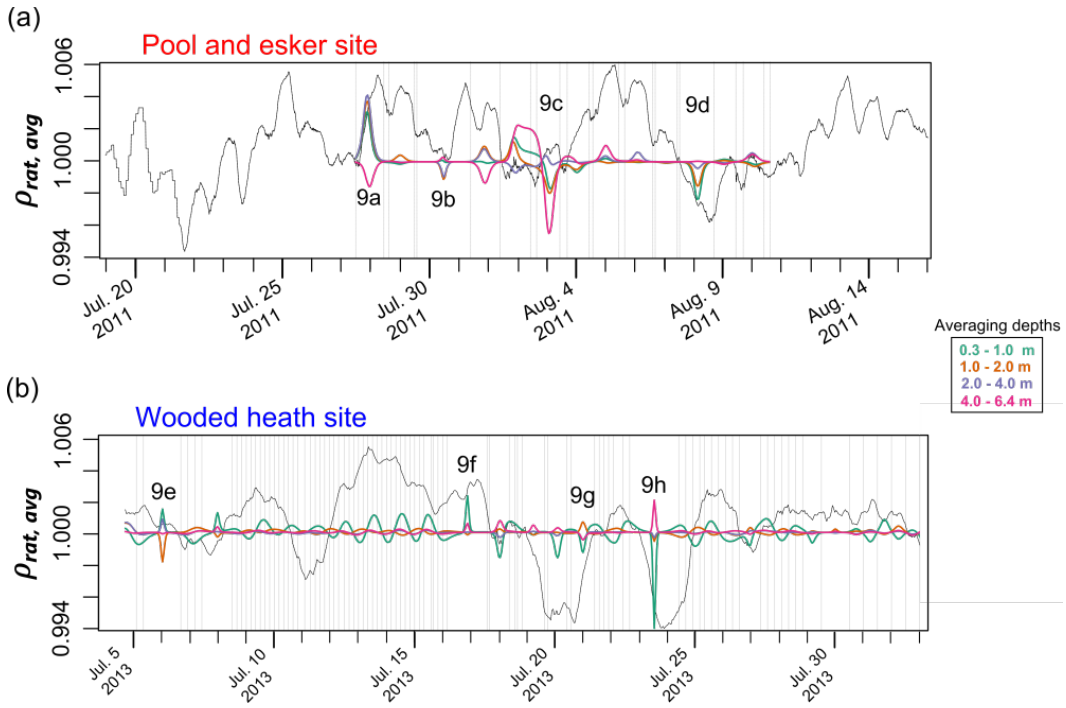

Figure 3.8 – interpolated time-series ERI results from (a) the pool and esker site in 2011 and (b) the wooded heath site in 2013. Each shows interpolated ratio resistivity data for four depth regions from the region beneath the array. Faint gray vertical lines show actual data collection initiation times, and black line shows relative atmospheric pressure variations. Slices of the time series that are shown as images in figure 3.9 are annotated.

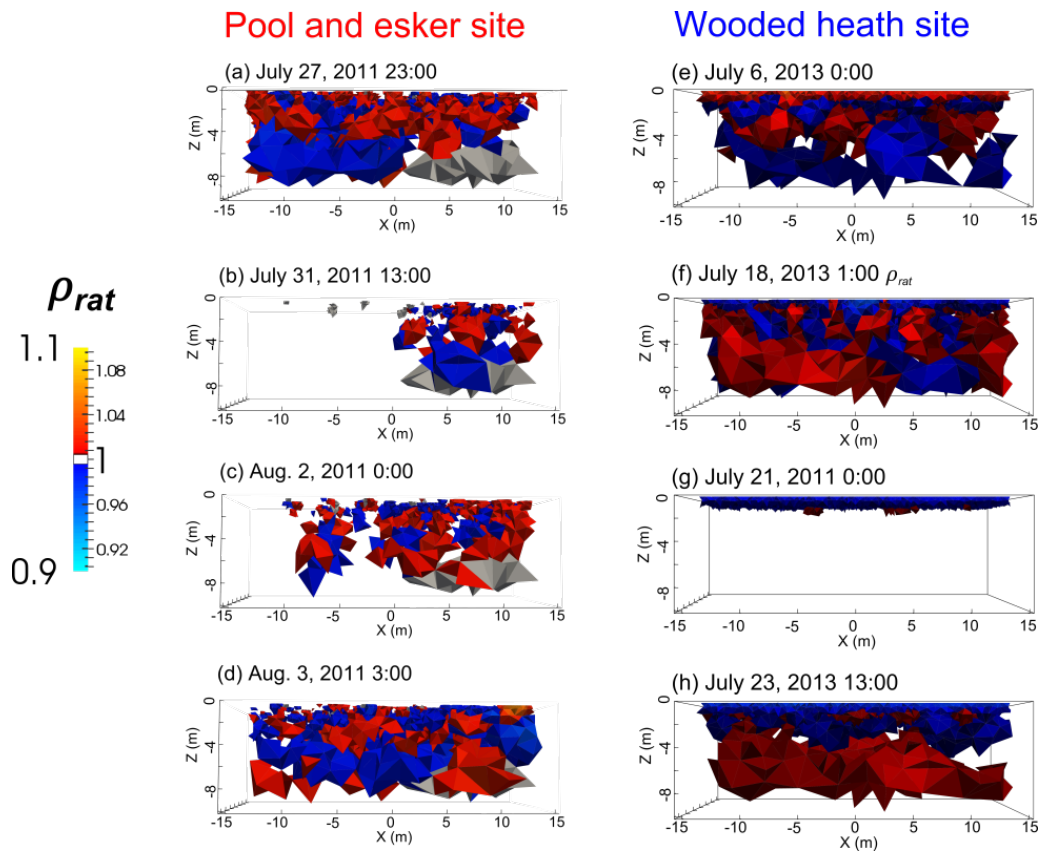

Figure 3.9 – Side views of selected ERI 3D images (with image threshold of > ±0.002). (a – d shows images from the pool and esker site ERI time series (Figure 3.8a), while (e – h) show images from the wooded heath site time series (Figure 3.8b). Raw resistivity values greater than 500 ohm m are shown in gray in (a – c) and correspond to a topographic high in the esker deposit.

3.5 Discussion

3.5.1 Site contrasts and gas dynamics

The two sites examined in this study greatly differ in terms of peat structure and composition. The pool and esker site possesses a poorly decomposed upper 2 m zone and a chaotic structure and a more decomposed and homogeneous structure below 2 m (Fig. 3.3a). Gas content values derived from the GPR CMP showing maximum gas content between 1.0 and 2.5 m depth (Fig. 3.4e), while the 5TE probes showing maximum gas content initially at the 3 m probe and later at the 0.5 m probe (Figs. 3.4d and 3.5c). Temperature data show decreasing temperature with depth that stabilizes at roughly 2 m at 8.5 °C (Fig. 3.4f).

The pool and esker ERI time series (Figure 3.8a) shows typically larger magnitude ERI events, and in particular more decreases in ratio resistivity from deeper averaging regions (2.0 to 6.4 m) than the wooded heath site (Figure 3.8b), supporting data from the 5TE probes (Figure 3.5) that loss of gas from deep regimes is more common at the pool and esker site in the absence of apparently laterally continuous confining layers. Additionally, ERI events are local to the eastern side of the array at the pool and esker site on at least two occasions (closer to the esker crest, Figure 3.9b and 3.9c). This is further supported by separating the ratio ERI time series shown in Figure 3.8a into a western and eastern side of the array, which confirmed on average larger magnitude events originating in the eastern side of the array (included in the SI). Additionally, time-lapse peat deformation data (Fig. 3.6a – 3.6c) show larger variations throughout the study period in proximity to the esker crest below the site further suggesting that gas dynamics are more active in this region.

A range of CH_4 concentrations of 33 % to 52 % by volume were sampled from peat at the pool and esker site (Fig. 3.7b), and higher chamber CH_4 fluxes (up to 30 mg m^{-2} hr^{-1}) were also recorded (Fig. 3.7d). This average CH_4 flux is high compared to other peatlands, and particularly *Sphagnum* bogs, owing to the fact that bogs typically possess a pH lower than optimal for methanogenic activity [*Dunfield et al.*, 1993] and relative difficulty decomposing *Sphagnum* litter compared to other vegetation [*Moore and Basiliko*, 2006].

By contrast, the wooded heath site depicts variable decomposition with depth, with typically less decomposed deep peat, and the presence of several subparallel GPR reflectors, often associated with woody debris (Fig. 3.3b). Gas content measured with GPR suggests a maximum gas content that occurs in a layer between 3 and 4 m depth, while the 5TE probes show a maximum gas content at the shallow (0.3 m) probe that declines with depth (down to 4.5 m, Figs. 3.4d and 3.5d). Compared to the pool and esker site, the wooded heath site shows overall larger gas content (supported by both the 5TE probes and the GPR CMPs, Fig. 3.4d and 3.4e) and less variation in gas content (Fig. 3.5). Peat deformation and ERI data also support comparatively less gas content variability at the wooded heath site (Figs. 3.6d – 3.6g and Fig. 3.8b, respectively), with ERI data additionally showing changes in gas content that are generally more layered in appearance (particularly Fig. 3.9h). Limited gas sampling data also suggest lower CO_2 and CH_4 free phase gas concentrations in the shallow peat at the wooded heath site, as well as smaller average and maximum CH_4 fluxes (Figs. 3.7b – 3.7d). The average CH_4 flux measured at this site (2 mg m^{-2} hr^{-1}) is more typical of Northern peatlands, (for example, in a review of several peatlands [*Blodau* 2002] suggests an average between 0.2

– 3 mg m^{-2} hr^{-1}). Also, gas volume and relative CO_2 and CH_4 concentrations increased with depth at this site (Figs. 3.7a – 3.7c).

Sudden changes in gas content associated with atmospheric pressure drops and/or precipitation events and subsequent water table rise are visible in both the ERI data (Fig. 3.8) and the 5TE probe data (Fig. 3.5). In particular, precipitation and low pressure events that occurred on July 30, 2011 as well as for the August 1 – 4, 2011 at the pool and esker site are associated with a small and large ERI event (Figs. 3.9b and 3.9c, respectively). The July 30, 2011 event suggests predominantly gas increases in the 0.5 m and 4.5 m layers, and decreases in the 1.0 m and 3.0 m layers (Fig. 3.8a). The August 1 – 4, 2011 event (Fig. 3.9c) indicates an increase in gas content in all but the 3 m layer (which shows a slight increase) followed by a large decrease in most layers (the 3 m layer shows a mixed increase/decrease in the ERI response). The 5TE probe data also show dynamic behavior during these periods, with sudden increases in gas content observed at the 0.5 m and 1.0 probes (Figure 3.5c) during these periods. Such gas transfer events likely reflect gas release triggered by decreasing atmospheric pressure, as has been observed by others [e.g., *Tokida et al.*, 2005a; *Strack et al., 2005*; *Kellner et al.*, 2005; *Comas et al.*, 2011b; *Chen and Slater* 2015].

Sudden decreases in gas content at the 0.3 m 5TE probe coupled with slight increases in gas content recorded at the 1.0 m probe at the wooded heath site in response to atmospheric pressure drops are also observed (Figure 3.5d). In particular, such dynamics are observed during an atmospheric pressure drop and rain event occurring on July 23 – 24, 2013 (Fig. 3.5d). This event is also associated with ERI inferred gas content decreases in the 0.3 m layer, as well as slight decreases in all other layers except 4.5 m

(Figs. 3.8b, 3.9h). In this case, the ERI may be sensing gas bubble expansion in the deep peat in accordance with Henry's Law.

3.5.2 Shallow and deep peat models

The results of this study suggest that the pool and esker site is more accurately represented by the deep peat model of *Glaser et al.* [2004], whereas the wooded heath site is better characterized by the shallow peat model of *Coulthard et al.* [2009]. At the pool and esker site, lower free phase gas content in the deep peat (Figs. 3.4d, 4e, and 3.6c), and sudden losses of gas from the deep peat combined with sudden increases in the shallow peat (Figs. 3.8a and 3.5c) during atmospheric pressure drops, support the notion that gas transfer occurs from deep to shallow peat layers, whereas similar transfer dynamics are not observed at the wooded heath site. Buildup of gas in deep peat at the wooded heath site as seen from the gas trap data (Fig. 3.7a) and only one ERI-inferred loss of gas below 1 m (Fig. 3.9e) further suggest that competent peat/undecomposed material layers (Fig. 3.3b) at this site inhibit the release of gas to upper layers and/or the atmosphere.

Furthermore, elevated deep peat temperatures are observed at the pool and esker site compared to the wooded heath site (Fig. 3.4f), which may suggest an input of warmer water facilitated by downward flow driven by a hydraulic gradient toward the permeable esker deposit [*Comas et al.*, 2011b; *Bon et al.*, 2013]. Such flow may also function to provide microbes with additional nutrients and labile C and thus enhance gas production [*Reeve et al.*, 2009] as well as decomposition observed at this site (Fig. 3.3a). This hypothesis is further supported by geochemical data collected from screened wells from

another study in Caribou Bog during July, 1999 provided by A.S. Reeve [*unpublished data*, 2000]. Compared to the wooded heath site, the pool and esker site shows distinctly elevated dissolved phosphorous (Fig. 3.10b) and nitrogen (Fig. 3.10c) concentrations at all depths, as well as elevated calcium (Fig. 3.10f), potassium (Fig. 3.10g), sodium (Fig. 3.10h), sulfur (Fig. 3.10d), and magnesium (Fig. 3.10h) concentrations at 3 m depth compared to the wooded heath site. Methanogenic activity has been shown to be slowed in nitrogen limited environments [*Kotowska and Werner*, 2013]. In addition, these data show that the pH of the water sampled from the pool and esker site is also higher on the whole and averages near 6 (Fig. 3.10a) - approximately the optimum pH for methane development in peatlands [*Dunfield et al.*, 1993; *Ye et al.*, 2012].

3.5.3 Limitations and highlights

We recognize the inherent limitation of this study in terms of concentrating data collection at each site during two different years (Fig. 3.2), however we believe each year is likely representative of annual summer conditions given similar surface temperature, atmospheric pressure, and water level ranges between the two years (Figs. 3.5a and 3.5b). Further, the GPR CMP data were collected at both sites during the same day during 2013 (Fig. 3.2b) and show a clear difference in gas content between the sites (Fig. 3.5e), with the wooded heath site having an overall higher gas content and showing a maximum gas content in the deeper peat.

The timing and magnitude of events measured and/or inferred by the various technologies used in this study are not always in agreement. However, such discrepancies are easily explained by the different sampling volumes of the various measurements and the spatial and temporal variation in biogenic gas dynamics expected

in peatlands, given the heterogeneity observed in peat properties over relatively small distances [i.e., this study; *Baird et al.*, 2016]. For instance, 5TE probe gas content is representative of a very small (i.e., 1 cm^3) volume, whereas gas traps capture bubbles from a funnel with an open area of 284 cm^2, GPR CMPs estimate gas content in layers on the order of meters, and ERI inferred gas content changes are also on the meter scale and are subject to spatial smoothing. The problem of spatial scale can be visualized by looking at Figure 3.9, where each ERI image shows both increases and decreases in resistivity that occur across the horizontal plane, and imagining placing a 5TE probe at two of these contrasting locations in the same layer. Such placement would yield conflicting results if looking at the probe data alone. On the other hand, ERI is limited in terms of temporal scale, and is unable to capture discrete events like those shown in Fig. 3.5c and 3.5d. Thus, each technique has benefits and limitations, emphasizing the need for multimethod studies of peatland gas dynamics.

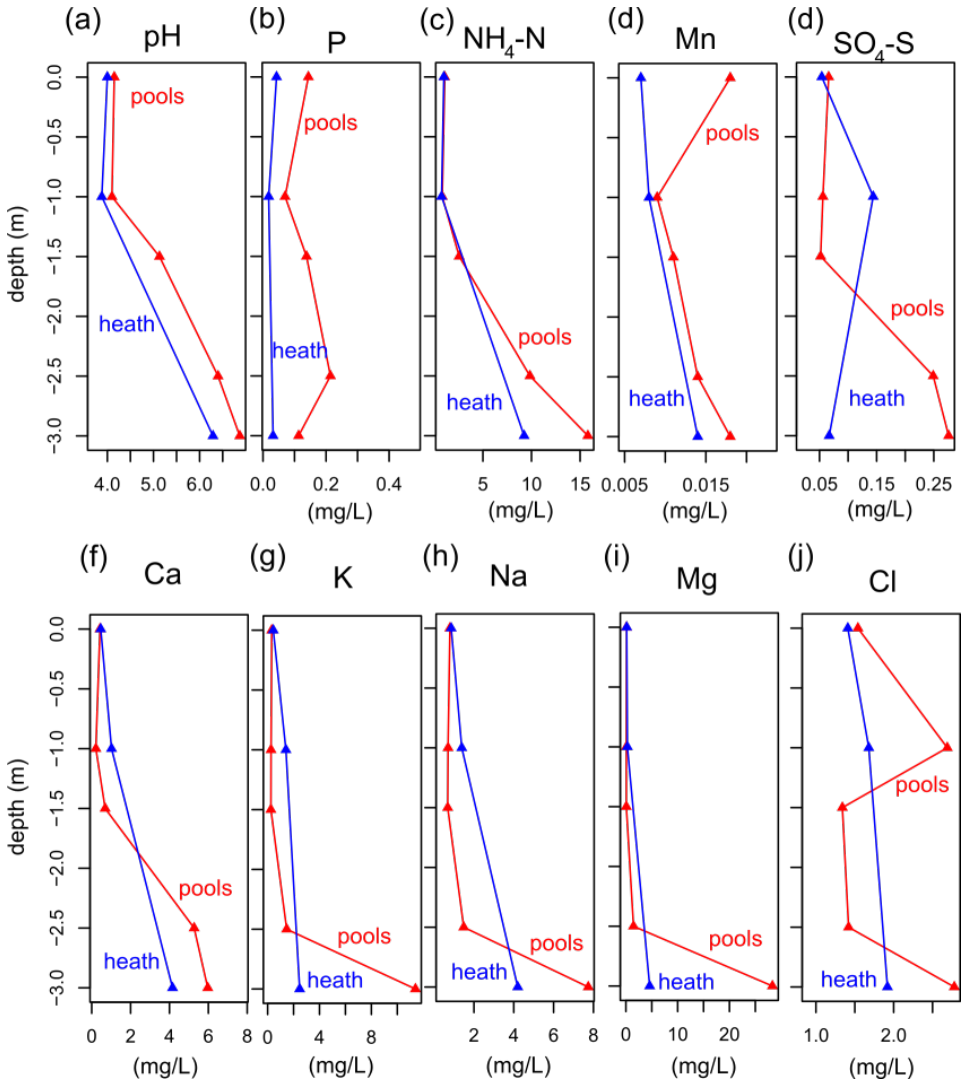

Figure 3.10 – geochemical profiles from fluid gathered from screened wells in July, 1999.

3.6 Conclusions

We find substantial differences in the gas dynamics of two sites with distinct peat physical properties within Caribou Bog, Maine. Despite a high degree of decomposition at depth and relatively low measured gas contents, the pool and esker site showed larger and more frequent gas decreases and larger fluxes (compared to the wooded heath site) that appear to often originate from the deep peat in the vicinity of the esker crest. Likely, the relatively permeable esker deposit enhances groundwater mixing as well as downward flow, supplying nutrients, labile C, and alternative electron acceptors that, in turn, drive enhanced CH_4 production and peat decomposition. This is further supported by relatively higher temperatures observed in the deep peat at the pool and esker site. During a roughly two week monitoring period, ERI data suggest at least 4 gas transfer events from regions below 1 m at the pool and esker site, whereas there is only one such event at the wooded heath site over a 2 month monitoring period (and this event is limited to the 1-2 m region). The lower level of decomposition at the wooded heath site and the presence of apparently laterally contiguous layers of woody debris likely act as barriers to the ebullition of gas at the wooded heath site. In the absence of such barriers at the pool and esker site, gas produced in deep peat more readily escapes to shallower layers and/or the atmosphere. In addition, a relatively impermeable clay mineral soil at the wooded heath site limits groundwater exchange and downward transport of labile C, rendering gas dynamics at this site more stagnant by comparison. These findings provide field-scale evidence that models of peatland gas dynamics must consider peat structural properties as well as hydrological dynamics between peat porewater and underlying mineral soil groundwater.

At the pool and esker site, we did not typically observe strong relationships between ERI data and gas content changes predicted due to solubility and/or volume changes in accordance with Henry's Law and the Ideal Gas Law. However, we did observe such relationships at the wooded heath site as well as increases in resistivity from deep peat during and following atmospheric pressure drops, which indicates ERI may be sensing large-scale increases in the volume of bubbles trapped in these layers as a result of the pressure decreases. Gas content data from 5TE probes less commonly showed this relationship. Likely, the probe data are very sensitive to small local changes in gas content (and therefore are still showing predominantly gas transport as opposed to solubility and/or volume changes). These observations highlight the importance of integrated approaches to studying gas dynamics in peatlands, given the scale differences between different types of measurements.

Chapter 4: Gas bubble size estimation in peat soils from EM wave scattering observed with ground penetrating radar[1]

Abstract

The size of biogenic gas bubbles in peatlands is believed to regulate ebullition of carbon gases to the atmosphere. The measurement of EM wave travel times using ground penetrating radar (GPR) is a proven field-scale method for indirect estimation of volumetric gas content. However, there is also the possibility that information on the size of the gas bubbles can be determined from the analysis of the spectral content of GPR signals as scattering attenuation possesses a frequency dependence for particles smaller than the EM wavelength (Rayleigh type scattering). Synthetic modeling shows that GPR data acquired with typical antenna frequencies are likely to be affected by bubble size in peat soils. Analysis of GPR data from two recent studies on peat monoliths where biogenic gas production was documented produced results consistent with the model predictions. Using the approach, zero offset cross borehole GPR data in a northern peatland suggest that large bubble clusters (i.e., > 0.04 m radius) occur in peat. These findings broaden the utility of GPR for providing information on biogenic gas dynamics in peatlands.

[1]This chapter submitted to *Water Resources Research* as: Terry, N. and L. Slater (2016), Gas bubble size estimation in peat soils from EM wave scattering observed with ground penetrating radar.

4.1. Introduction

Peatlands are an important global reservoir for the production, storage, and release of greenhouse gases like methane and carbon dioxide and are estimated to sequester up to 30 % of the global carbon pool [*Parish et al.*, 2008]. It is generally agreed that peatlands as a whole are global sinks of atmospheric CO_2 but sources of CH_4 [*Charman*, 2002]. Mechanisms for CH_4 release from peatlands include diffusion, transport through vascular plants, and ebullition (bubbling of free phase gas). Recent research has focused on the CH_4 ebullition pathway, as individual ebullition events have been shown to vary widely in magnitude across spatiotemporal scales [*Baird et al.*, 2004; *Comas and Wright*, 2012; *Klapstein et al.*, 2014].

Gas bubble size may play a crucial role in regulating ebullition from peatlands as well as determining the hydraulic properties of peat. For example, *Beckwith and Baird* [2001] demonstrated a reduction of hydraulic conductivity by 5 to 8 times which they attributed to pore blockage by gas bubbles, and that there appeared to be a bubble volume threshold after which ebullition began to occur. *Tokida et al.* [2005a] observed that volumes of ebullition recorded during drops in atmospheric pressure were proportional to increases in volumetric gas content, which suggests increasing bubble size (in addition to lower confining pressure) may play a role in triggering ebullition. *Chen and Slater* [2015] observed a similar phenomenon during bubble volume changes induced by changes in hydrostatic pressure. *Kellner et al.* [2006] developed a simple ebullition model based on bubble volume changes that incorporated threshold values for gas content and compared this model with laboratory data. While the model successfully predicted ebullition in many instances, the authors determined that, given the uncertain variation in peat

structural properties, a probabilistic, 'fuzzy' bubble volume threshold may be more appropriate for predicting ebullition.

Limited information on the size and shape of gas bubbles in peat exists, with estimates ranging from effective bubble radii of less than 10^{-5} m (in a laboratory x-ray imaging study by *Kettridge and Binley* [2008a]) to 5 x 10^{-1} m (in a field gas extraction study by *Tokida et al*., 2005b), to as large as 1 m (directly observed trapped under the ice in Caribou Bog by *Comas et al.*, 2008. In an echo sounder study of biogenic gas bubble ebullition from lake sediments, *DelSontro et al.* [2015] found bubbles with radii up to 1.5 x 10^{-2} m, and that bubbles larger than 5 x 10^{-3} m in diameter accounted for roughly 65% of the total gas volume, despite constituting less than 10% of the total bubbles counted.

Ground penetrating radar (GPR) has proven to be a useful tool for estimating free phase gas (FPG) content and bubble dynamics in peat (e.g., *Comas et al.* [2005a]; *Comas et al.* [2005c]; *Comas et al.* [2007], *Strack and Mierau* [2010]; *Parsekian et al.* [2010, 2011]). While GPR is an indirect method for studying FPG dynamics, in that a petrophysical transformation is required to convert electromagnetic (EM) wave travel time data to gas content, it has numerous advantages including (1) the ability to sense changes in FPG content without disturbing the peat structure itself, (2) rapid data acquisition time, and (3) the ability to sense changes at cm to m scales over an area (if collected along a profile) or volume (if collected on a grid) on the order of several m to km.

The general approach used in these studies to estimate FPG content from GPR data is to estimate EM wave velocity from depth intervals within the peat, then to convert velocity to dielectric permittivity, and finally to apply a petrophysical model (typically

some multiphase mixing model, such as the complex refractive index model, or CRIM [*Wharton et al.*, 1980]) to convert to FPG content. While this travel time analysis of GPR data to estimate FPG content in peat is well reported, analysis of the frequency content of the transmitted and returned EM signal has not been explored for peat gas applications. Yet, frequency content may provide information about the size of the gas bubbles themselves in addition to gas content, in that small bubbles (relative to wavelength) acting as scatterers will show preferential attenuation of higher frequencies (Rayleigh scattering), whereas scatterers of a size on the order of the wavelength will not (Mie scattering). *Comas et al.* [2005a] suggest that 'shadow zones' – areas of visible GPR signal attenuation in plots of GPR amplitudes – may represent signal scattering by small bubbles, given enhanced CH_4 and CO_2 concentrations and no evidence for a change in peat physical properties in such zones.

In this study, we demonstrate the potential for frequency analysis of GPR data to provide information about gas bubble size in addition to volumetric gas content by performing synthetic modeling, analyzing results from two laboratory studies and interpreting a field-scale cross-borehole GPR dataset. The synthetic model demonstrates that preferential attenuation of higher frequencies will occur with bubble growth for most common GPR frequencies and bubble sizes, but that such frequency dependence is lost (due to Mie scattering effects) when bubbles reach a certain size (depending on frequency). We then estimate absorption attenuation in two lab studies and a field study, and employ a curve fitting approach to GPR frequency power spectra to estimate changes in bubble radii based on changes in the power spectra after correcting for absorption attenuation.

4.2 Background

4.2.1 GPR propagation and attenuation in earth materials

In low-loss media, the electric field of a 1D plane wave at a given place and time is,

$$E(x,t) = E_0 e^{i(\omega t - kx)}, \tag{4.1}$$

where E_0 is peak wave amplitude [dB], ω is the angular frequency [radians s^{-1}], and k is the complex wavenumber [radians m^{-1}].

The complex wavenumber is,

$$k = \beta - i\alpha, \tag{4.2}$$

where β is the phase factor, ${}^{\omega}/_{\beta} = v$ is the phase velocity [m s^{-1}], and α is the attenuation coefficient [dB m^{-1}]. If attenuation is purely due to absorption (also called intrinsic attenuation), each of these quantities depends on the frequency dependent, complex quantities of electrical conductivity (σ), magnetic permeability (μ), and dielectric permittivity (ε) as follows,

$$\alpha_{abs} = \omega \left[\frac{\mu\varepsilon}{2} \left(\sqrt{1 + \left(\frac{\sigma}{\omega\varepsilon} \right)^2} - 1 \right) \right]^{1/2}, \tag{4.3}$$

and,

$$\beta = \omega \left[\frac{\mu\varepsilon}{2} \left(\sqrt{1 + \left(\frac{\sigma}{\omega\varepsilon} \right)^2} + 1 \right) \right]^{1/2}, \tag{4.4}$$

where α_{abs} is the attenuation coefficient due to absorption. For most non-magnetic soils (e.g. organic soils such as peat), μ is equal to the free space value [*Turner and Siggins*, 1994].

In addition to the absorption attenuation introduced in Eq. 4.3, total attenuation, α_{tot}, of a GPR signal consists of an additional scattering component, α_{scat}, where

$$\alpha_{tot} = \alpha_{abs} + \alpha_{scat}. \tag{4.5}$$

GPR, particularly tomography studies, have estimated attenuation as a means of inferring electrical conductivity distributions [e.g., *Lambot et al.*, 2004] and more recently, scattering zones [e.g., *Grimm et al.*, 2006; *Harbi and McMechan*, 2012]. The latter is generally by subtracting theoretical absorption attenuation (Eq. 4.3) from the total attenuation estimated from GPR (Eq. 4.5).

4.2.2 Scattering

The Mie solution to Maxwell's equations describes the scattering of electromagnetic waves by spheres. Although applicable to particles of all sizes, 'Mie scattering' typically refers to particles with a circumference of the same order as the incident wavelength, since very small and very large particles (relative to wavelength) can be generalized using the Rayleigh scattering approximation and the laws of geometrical optics, respectively. Rayleigh type scattering is 4^{th} order dependent on wavelength and 6^{th} order dependent on particle diameter. Therefore, increases in the number or size of particles (while still smaller than the incident wavelength) are expected to result in preferential

attenuation of higher frequencies, meanwhile Mie type scattering is much less wavelength dependent.

4.2.3 Time-domain analysis

Data obtained from GPR consists of time (typically presented in ns) and amplitude (typically measured in mV), obtained for a specified sampling interval. The phase velocity of GPR waves can be highly frequency dependent (Eq. 4.4); a property known as dispersion [i.e., *van der Kruk, 2006*; *Bradford*, 2007]. While there are situations where significant velocity dispersion can occur in earth materials, peat soils do not usually fall into this category due to typically high dielectric permittivity (close to that of water) and low electrical conductivity (< 10 mS m^{-1} in Caribou Bog [*Slater and Reeve*, 2002]) for frequencies commonly used in GPR [*Reppert et al.*, 2000]. Therefore, for most peat soils, where magnetic materials are also seldom present, EM wave velocity is independent of frequency and can be estimated via (low loss assumption)

$$v \approx {}^{1}/_{\sqrt{\varepsilon}}. \tag{4.6}$$

Thus the travel time t of the EM wave over a known distance d can be used to calculate EM velocity and relative dielectric permittivity,

$$\varepsilon_r = (ct/d)^2, \tag{4.7}$$

where c is the speed of light in a vacuum, and $\varepsilon_r = \varepsilon/\varepsilon_0$, where ε_0 is the free space dielectric permittivity. Increases in gas content will be reflected as decreases in ε_r.

To estimate gas content from ε_r, a multiphase mixing model may be used, which considers the dielectric permittivity of individual components. The general form of such a model is referred to as the Lichteneker-Rother model [*Lichteneker and Rother*, 1931]. When considering a peat soil with a solid, liquid, and gas phase, this model has the form:

$$\varepsilon_r{}^{\gamma} = (\phi - FPG)\varepsilon_{r(w)}{}^{\gamma} + (FPG)\varepsilon_{r(g)}{}^{\gamma} + (1-\phi)\varepsilon_{r(s)}{}^{\gamma}, \qquad (4.8)$$

where FPG is the free phase gas content, $\varepsilon_{r(w)}$ is the relative dielectric permittivity of the liquid phase, $\varepsilon_{r(g)}$ is the relative dielectric permittivity of the gaseous phase, $\varepsilon_{r(s)}$ is the relative dielectric permittivity of the solid phase, and γ is a fitting parameter that physically represents the orientation of electromagnetic waves to soil particles. The γ is commonly assumed to be 0.5, in which Eq. 4.8 is known as the complex refractive index model (CRIM) [*Wharton et al.*, 1980].

4.2.4 Frequency domain analysis

Each GPR trace consists of time and amplitude information, digitized according to a specified sampling interval. Each trace is therefore a discrete signal that can also be analyzed in the frequency domain, for example using a discrete Fourier transform (DFT). The fast Fourier transform (FFT) originally developed by *Cooley and Tukey* [1965] is the form of the DFT typically used in numerical applications due its fast execution time. The FFT provides a time-averaged frequency representation of a signal, typically presented as a power spectrum, which depicts the signal power attributed to various frequencies in the signal.

Scattering attenuation and absorption attenuation are frequency dependent for peat-like soils as we shall show. However, the scattering attenuation frequency dependence diminishes when particles (in this case, gas bubbles) exceed a certain size. Therefore, changes in scattering attenuation will have different effects on the shape of the power spectrum depending on the size of gas bubbles.

4.3 Methods

4.3.1 Synthetic study

A suite of Matlab-based codes were used to analytically calculate Mie scattering of EM waves from spheres [*Mätzler*, 2002] based on theory presented by *Bohren and Huffman* [1998]. Numerical methods for computing scattering for more complex geometries are also available [e.g., *Draine*, 1988], however such considerations are beyond the scope of this paper. In brief, the *Mätzler* [2002] code calculates the scattering cross sections for a monochromatic wave from a particle immersed in a medium. The frequency of the wave, the particle size, the particle refractive index, and the medium refractive index are input. The refractive index is another way of expressing dielectric permittivity and is defined as $(\varepsilon_r)^{1/2}$. The relative refractive index (defined as the ratio of the refractive index of the particle divided by the refractive index of the medium) of radar energy entering an air bubble from peat is very low (~0.12).

The scattering cross section describes the effective area of blocked forward going radiation by the particle. Likewise, the backscattering cross section describes the effective area of blocked radiation bouncing back from the particle. The scattering cross section (m^2) multiplied by the number of particles per unit volume (m^{-3}) gives the

scattering attenuation coefficient, α_{scat}. Although the [*Mätzler*, 2002] code also calculates the energy lost by absorption into the particles themselves, this loss is negligible compared to the energy lost by scattering due to gas bubbles.

For this study, the *Mätzler* [2002] code was used to simulate backscattering attenuation in peat for a range of bubble radii (10^{-5} m to 10^{-1}) over GPR frequency ranges (125 MHz to 2,400 MHz). One limitation of our approach is that we do not account for the fact that scattered energy is not necessarily lost and could ultimately be redirected to the receiver, however for isotropic random scatterers we believe this approach provides a good approximation of the actual attenuation we would expect to see in real data under the simulated conditions.

4.3.2 Bubble size model

Dielectric permittivity values were estimated for each trace using Eq. 4.7. The calculated permittivity values were used to infer changes in overall gas content (using Eq. 4.8) and electrical conductivity assuming non-magnetic conditions and using a starting conductivity ($\sigma \approx 3.4$ mS m^{-1}) consistent with peat materials under fully saturated conditions (typical of peat in Caribou Bog, Maine, e.g., *Comas et al.*, 2005; *Kettridge and Binley*, 2011; *Parsekian et al.*, 2012b). The electrical conductivity values were updated by the following formula from *Slater et al.*, [2007],

$$\sigma_t = \left[\frac{\phi_t - FPG_t}{\phi_0 - FPG_0}\right]^{-n} \Big/ \sigma_0, \tag{4.9}$$

Where σ_0 is the starting conductivity, σ_t is the updated conductivity, FPG_0 is the starting free phase gas content, FPG_t is the updated free phase gas content, $\phi_0$is the starting porosity, $\phi_t$is the updated porosity, and n is the saturation exponent.

The attenuation of the electric field at time 0, $E(0)$, and time t, $E(t)$, can be described as follows,

$$E(0) = E_0 e^{-d\alpha_{tot,0}}, \tag{4.10}$$

and

$$E(t) = E_0 e^{-d\alpha_{tot,t}}. \tag{4.11}$$

Putting peak amplitude in terms of $E(0)$ and substituting yields,

$$E(t) = \frac{E(0)}{e^{-d\alpha_{tot,0}}} e^{-d\alpha_{tot,t}}, \tag{4.12}$$

and taking the natural log of both sides gives,

$$\ln\left(\frac{E(t)}{E(0)}\right) = d\left(\alpha_{tot,0} - \alpha_{tot,t}\right). \tag{4.13}$$

Finally, taking the exponential of both sides and rearranging gives an equation for predicting the electric field strength at time t based on computed attenuation values and the electric field strength at time 0,

$$E(t) = E(0) e^{d\left(\alpha_{tot,0} - \alpha_{tot,t}\right)}. \tag{4.14}$$

Power spectra for each GPR trace are computed via the FFT with an initial trace chosen as a reference. Backscattering cross sections are then computed for a range of bubble radii using the *Mätzler* [2002] MATLAB code. Values for backscattering attenuation are estimated by calculating the number of scatterers per unit volume for a

given gas content. These values are added to the intrinsic attenuation value calculated by Eq. 4.3 to provide synthetic curves for $\alpha_{tot,0}$ and $\alpha_{tot,t}$. Least squares curve fitting is then performed according to Eq. 4.14 to estimate the best fit average bubble radius for the reference trace and the trace at time t.

4.3.2 Laboratory study 1: ebullition monitoring

An eight week study of ebullition from a peat monolith taken from Caribou Bog using 1200 MHz transmission GPR measurements was performed by *Yu et al.* [2014]. The monolith was placed in an acrylic container with a volume of roughly 0.3 m^3. Prior to the experiment, the sample was drained and rewetted with distilled water, then kept at room temperature (~23 °C) during the experiment. The container was sealed with the exception of ports to sample pore water and a tube connected to a fast methane analyzer to measure ebullition during the study. Transmission GPR data were collected from nine positions as shown in Figure 4.1 on a daily to twice daily basis.

We analyzed these GPR data using the approaches described above to estimate gas content and the power spectra. First, traces were corrected to the appropriate time-zero by analyzing airwave data collected before each data collection time. First arrival times were picked and assumed to represent a raypath directly through the sample. Dielectric permittivity, ε_r, was then estimated by Eq. 4.7 and converted to gas content through Eq. 4.8.

Subsequent basic processing of the data included time-zero correction, dewow, gain to correct for geometric spreading (d^2), and bandpass filtering to include a range of one

octave above and below the central frequency (600 to 2400 MHz); this choice was based upon visual analysis of FFT traces in the data.

4.3.3 Laboratory study 2: Bubble tracking

Several 1200 MHz GPR reflection datasets were collected by *Chen and Slater* [2015] as part of a study to observe bubble dynamics in peat in response to induced pressure variations. In this study, 12 GPR reflection traces were collected along four depth intervals of a peat monolith (Figure 4.1b), also gathered from Caribou Bog. In addition, the area of bubbles built up on the side of the tank was visually tracked (through a hand drawing method). We used one of these datasets (Feb. 14, 2014) to gain further insight as to how the number and size of bubbles may influence frequency properties of the GPR signal.

Our method of analysis differed somewhat compared to the *Yu et al.* [2014] lab experiment by virtue of this study representing a GPR reflection dataset. The only visible reflection from this dataset occurred from the opposite side of the tank. Although minor reflection events likely occur within the peat monolith before encountering the side of the tank, we found that this section of the signal was typically noise dominated. Therefore, we limited our analysis to the portion of the signal from the first arrival of this reflection until noise again dominated (approximately 6 ns later), and ignore the first portion of the signal consisting of the airwave and time before the reflection event. Otherwise, analysis proceeded in the same way as the previous laboratory study.

4.3.4 Field study

Several 250 MHz zero offset profile datasets were collected in Caribou Bog, Maine during the summer of 2011 and consisted of 50 transmitter-receiver positions (Figure

4.1c). The field setup included two boreholes spaced roughly 4 m apart. Antennas were turned on and lowered to the bottom of the boreholes to acclimate to temperature, then raised to the top and each lowered by 0.1 m increments. Each transmitter-receiver position was corrected for slight borehole deviations measured in the field.

Data processing for this field transmission dataset was similar to that described for the *Yu et al.* [2014] laboratory data. First, time-zero correction to all traces was performed by analyzing airwave arrivals collected over a known distance prior to the transmission measurements. Next, gas content was estimated for each trace according to Eq. 4.7 and 4.8 assuming straight raypaths between transmitter-receiver positions. Basic processing included dewow, gain to correct for geometric spreading (d^2), and a bandpass filter (125 to 500 MHz).

An additional difference in our approach to the field data was the use of actual electrical conductivity information from the field (rather than propagate changes in electrical conductivity using an assumed initial conductivity and Eq. 4.9). Although porosity values were still assumed constant, this distinction allowed us to estimate the absorption attenuation component of Eq. 4.14 rather than make assumptions about an initial conductivity and employ Eq. 4.9.

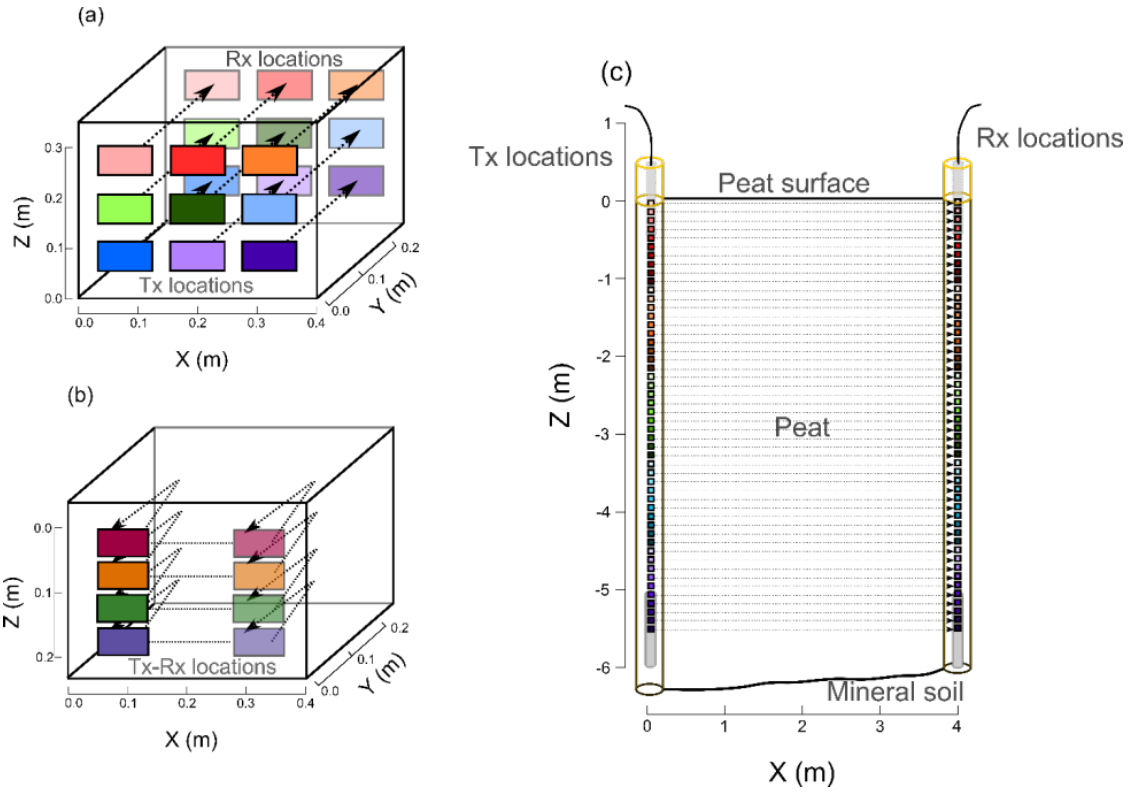

Figure 4.1 – Schematics of the two lab studies and the field study analyzed in this paper. (a) depicts the 9 transmitter-receiver locations of the 1200 Mhz GPR study of a peat monolith from *Yu et al.* [2014], (b) the 4 depth intervals (12 traces each) from which reflection GPR data were collected in the *Chen and Slater* [2015] lab study, and (c) the 50 transmitter-receiver locations in a cross borehole study in Caribou Bog, Maine.

4.4 Results

4.4.1 Synthetic results

Figure 4.2 shows the scattering attenuation for five bubble radii assuming 10 % gas content over GPR bandwidths used in this study (ranging from 125 – 2,400 MHz). The results show strong frequency dependence (i.e., Rayleigh-type scattering) where the ratio of wavelength to bubble diameter is high (this region includes the 250 MHz band

used in our field study). However, where wavelength is on the order of the particle diameter, scattering attenuation is no longer frequency dependent (see flattening of curves); this effect may be observed for large bubbles (> 0.03 m) in frequencies used for our lab study and very large bubbles (> 0.1 m) for the field study.

Figure 4.2 also shows the absorption attenuation calculated for the electrical conductivity assumed in the lab studies (3.4 mS/m). The absorption attenuation is less frequency dependent compared to Rayleigh type scattering, yet is more so compared to Mie type scattering. Although the predicted attenuation due to electrical conductivity is larger than that due to scattering across all frequencies investigated, the shape and total magnitudes of the total attenuation curve should reflect both absorption and scattering contributions (that in turn are sensitive to the size of bubbles).

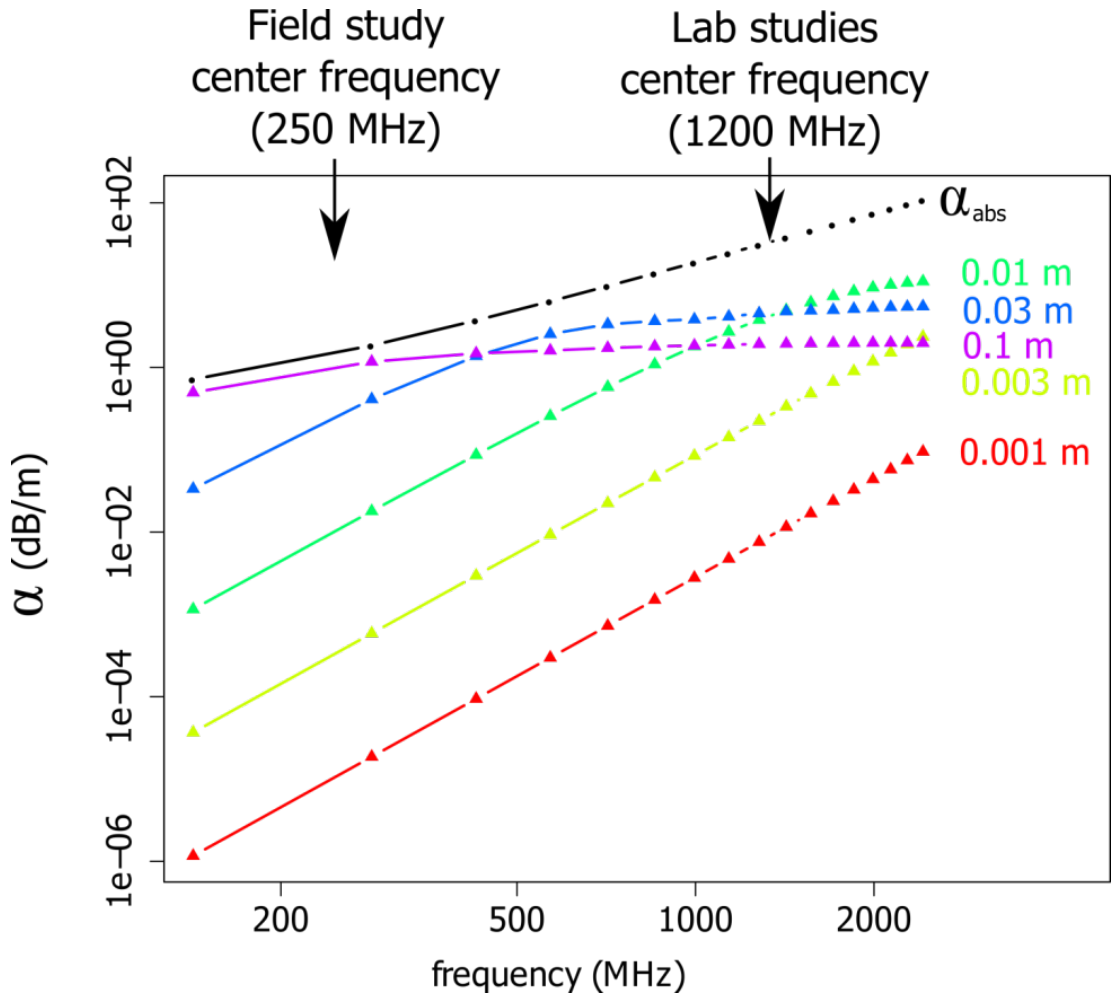

Figure 4.2 - predicted scattering attenuation for GPR frequencies considered in this study from spherical bubbles with radii ranging from 1 x 10^{-3} to 1 x 10^{-1} m and 10 % gas content (colored lines). Absorption attenuation for conductivity = 3.4 mS/m shown as black line.

4.4.2 Lab results: Yu et al. [2014]

Figure 4.3 shows the power spectra observed at each of the nine GPR transmitter-receiver positions over time. Distinct changes in the spectra are observed over time at specific locations. The upper and middle layers (particularly Figs. 4.3b – 4.3e) show a decrease in power at higher frequencies (i.e., > 600 MHz) over time, whereas the lower layer (Figs. 4.3g – 4.3i) typically show increases in power at these frequencies.

Figure 4.4 shows gas content estimated from dielectric permittivity variations through Eqs. 4.7 and 4.8. A value for γ of 0.33 was used [*Yu et al.*, 2014]. The porosity, ϕ, was assumed as 0.94 based on data collected following the experiment. The permittivity value for soil, $\varepsilon_{r(s)}$, was selected as 2 [*Comas et al.*, 2007]. Bubble radii were estimated using Eq. 4.14 and the approach described above to yield the estimates shown in Fig. 4.4. Bubble radius estimates range from 0.002 m to 0.024 m. For the upper left location (Figure 4.4a) gas content is more or less stable at nearly zero, suggesting that this region remained saturated and little FPG accumulated over time. The estimated bubble radius at this location, however, varies between minimum and maximum values. The other eight locations (Fig. 4.4b – 4.4h) show increases in gas content throughout the duration of the study, consistent with development of gas bubbles following rewetting of the peat monolith at the beginning of the study. In many cases (Figs. 4.4e – 4.4i), the rate of increase in gas content is much faster at first, then becomes less rapid or stabilizes. In the upper layer (Figs. 4.4b and 4.4c) the estimated bubble radius decreases throughout the study period. The center middle and lower layers (Figs. 4.4e and 4.4h) indicate a trend in increasing bubble radius, while the locations corresponding to Figs. 4.4d, 4.4f, 4.4g and 4.4i show mixed patterns.

4.4.3 Lab results: Chen and Slater [2015]

Figure 4.5a shows the power spectra from GPR for the four depth regions analyzed in the *Chen and Slater* [2015] lab study and Figure 4.5b shows gas content estimates. Figure 4.5c shows the area percentage of bubbles observed on the side of the tank, while Figure 4.5d shows average, minimum and maximum effective bubble radii (calculated from the total area of individual bubbles on the side of the tank). The circled

symbols in Fig. 4.5d indicate the estimated radii of bubble using the estimation approach described above. The area of bubbles observed appears to be a reasonably good proxy for the FPG content of the layers themselves, as evidenced by the direct relationship between area percentage of bubbles (Fig. 4.5c) and the gas content estimated for the layer (Fig. 4.5b). The largest gas content value and area percentage of bubbles occurs in the 10 – 15 cm layer, followed by the 15 – 20 cm layer, the 5 – 10 m layer, and finally the 0 – 5 cm layer. The estimated radii from GPR are consistently larger than those estimated by the hand drawing approach. While the 10 – 15 cm layer shows the highest gas content and the largest bubbles observed through hand drawing, the bubble size estimated through GPR indicates the largest bubbles exist in the 15 – 20 cm layer. Otherwise, bubble size estimates from GPR follow the same pattern as those estimated from hand drawing.

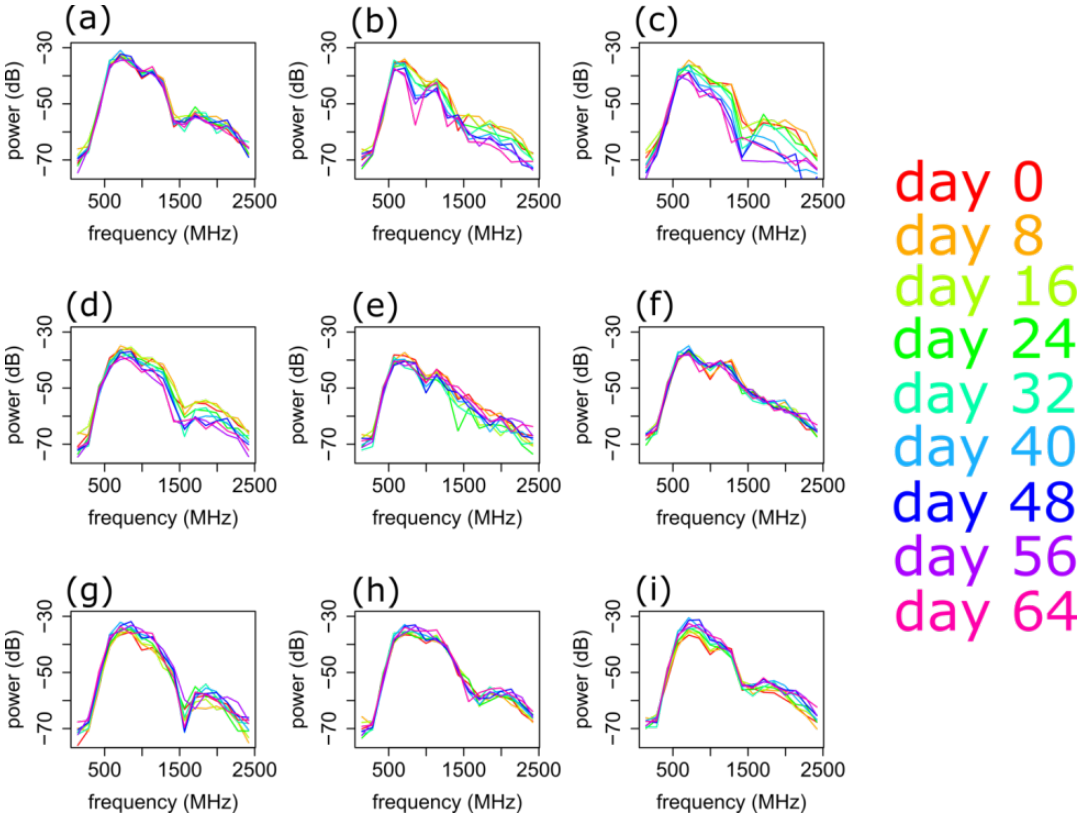

Figure 4.3 – power spectra for each of the nine observation positions in the *Yu et al.* [2014] lab study.

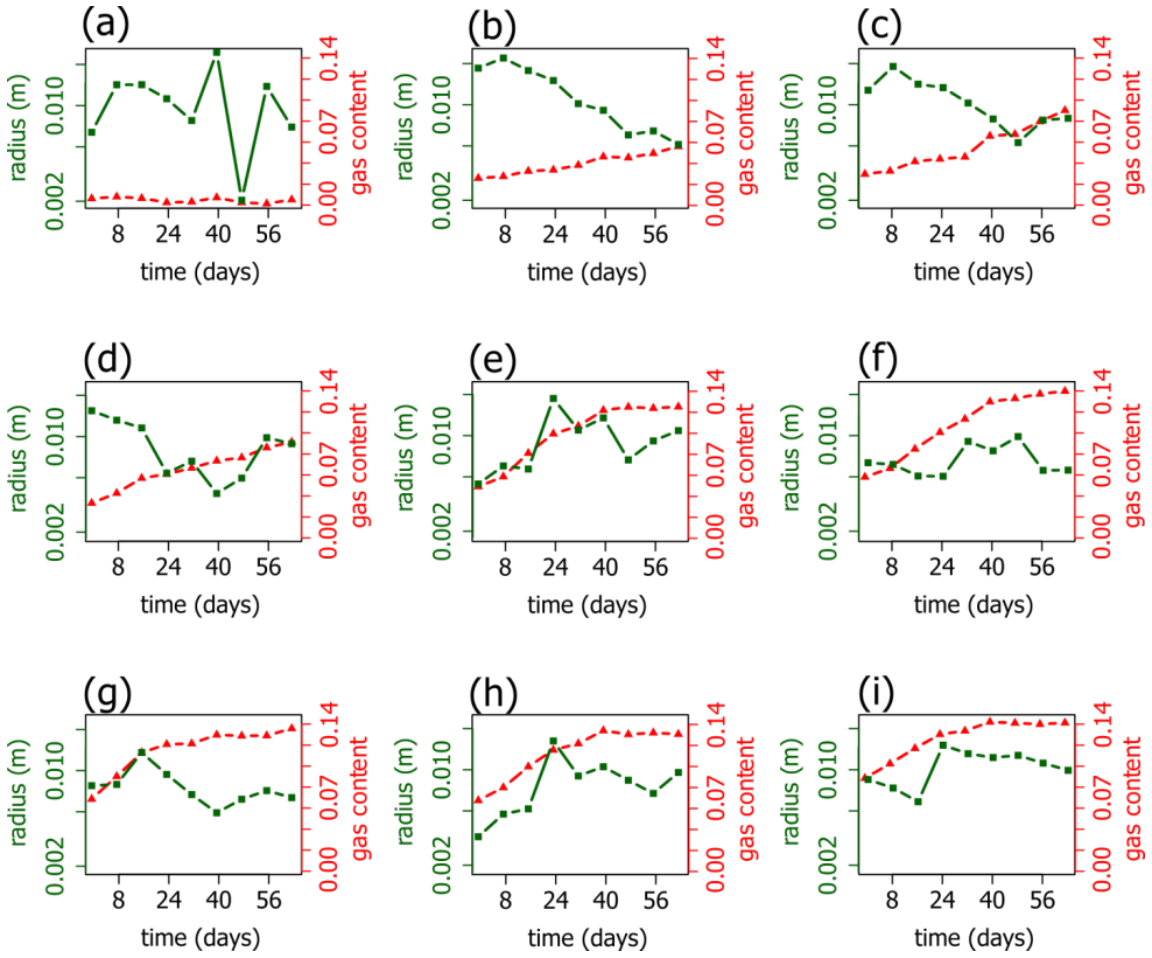

Figure 4.4 – relationship between estimated bubble radius and gas content for each of the nine observation positions in the *Yu et al.* [2014] lab study.

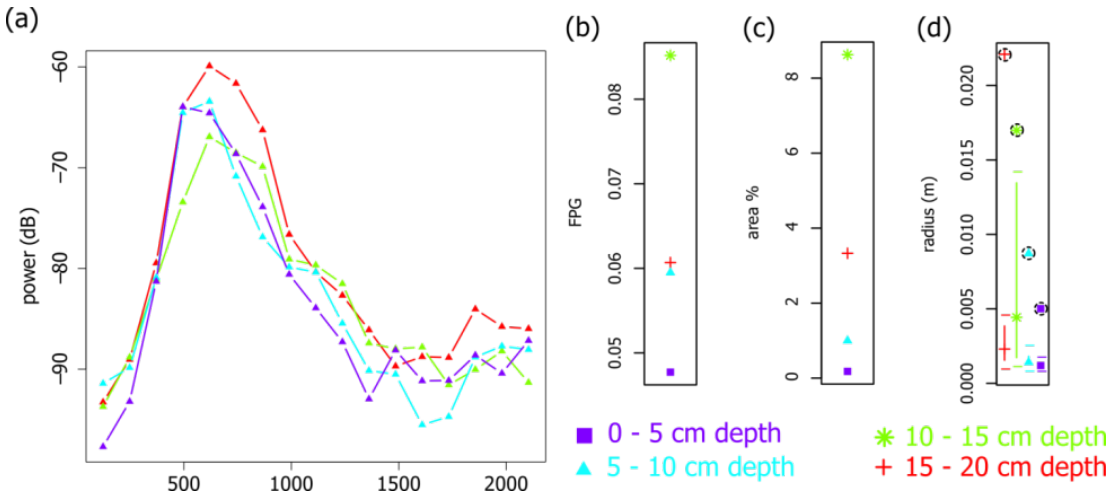

Figure 4.5 – parameters from the *Chen and Slater* [2015] bubble tracking lab study. (a) the power spectra from the 4 depth regimes. (b) the gas content calculated from GPR first arrivals, (c) relative area on the side of the tank with bubbles for each depth interval area, (d) average bubble radius observed through hand-drawing, with bars indicating the range of sizes observed. Circled points indicate the radii estimated through the GPR bubble size estimation approach used in this paper.

4.4.3 Field results

Coring information gathered during installation of the boreholes for the field study is shown in Figure 4.6a. The von Post H values shown in this figure represent a qualitative field assessment of the relative degree of decomposition (H1 being least decomposed, H10 being most decomposed). Levels of decomposition increased with depth, with generally lower decomposition observed in the upper 3 m and a more decomposed region below 3 m.

The power spectra for 11 positions from the field dataset are shown in Figure 4.6. The power spectra above 3.3 m are noticeably more peaked in shape than those at greater depths. There is also an observable decrease in magnitude from the surface to 3.3 m depth across all frequencies of the power spectra.

Depth averaged (from the borehole region) inverted bulk conductivity data from a separate electrical resistivity imaging experiment is shown in Figure 4.7b. Electrical conductivity was found to decrease with depth, averaging around 8 mS m^{-1} at the surface to 5 mS m^{-1} at the mineral soil.

The estimated gas content from all field datasets are shown in Figure 4.7c. Gas content shows a sudden decrease around 3 m depth. Changes in the estimated bubble radius also occur around this depth, showing a sudden increase in size above this layer and a sudden decrease below. The average bubble radii from this lower region are on average slightly larger than those estimated for the region above 3 m.

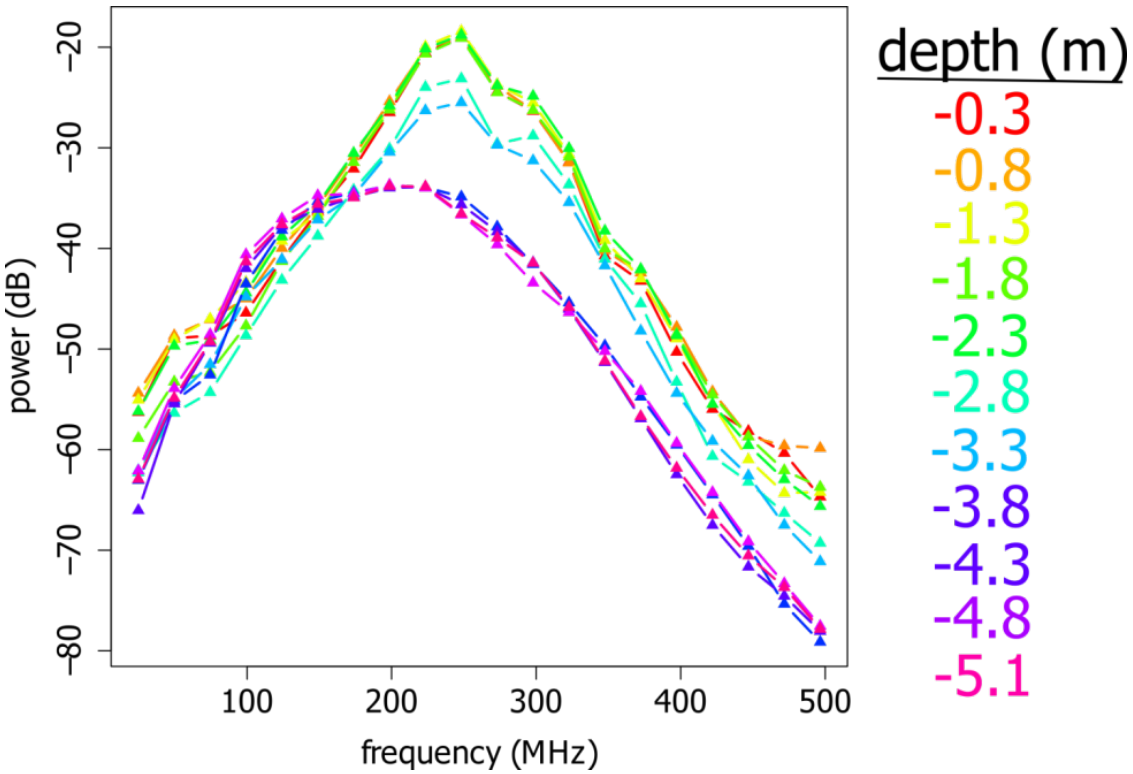

Figure 4.6 – power spectra for the field study at the 11 depths analyzed.

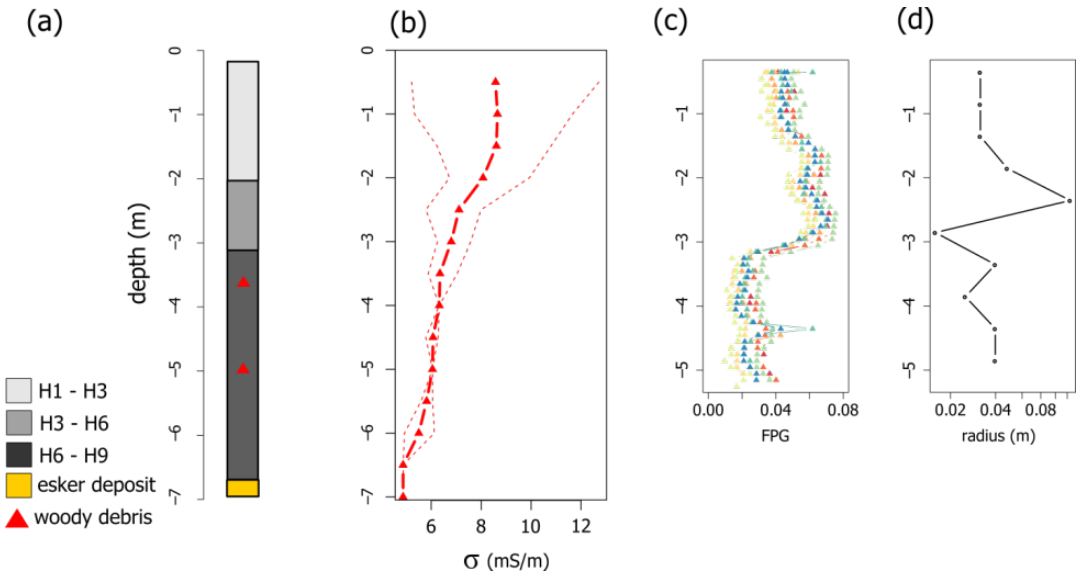

Figure 4.7 – (a) coring information from a core taken during installation of the boreholes used for the field GPR transmission study. (b) bulk conductivity response from a separate electrical resistivity imaging experiment averaged for the depth profile of the GPR borehole region. (c) estimated gas content and (d) shows estimated bubble radii.

4.5 Discussion

In general, we expect that the formation of gas bubbles has a contrasting effect on total attenuation. On the one hand, the formation of bubbles increases scattering attenuation. On the other hand, development of such bubbles decreases water content and therefore decreases absorption attenuation (primarily due to dielectric relaxation of water molecules). The overall effect of developing gas bubbles on total attenuation will therefore be dependent on the size of the bubbles themselves.

A key observation of this study is that the frequency dependence of these two attenuation phenomena differ vastly. Whereas absorption attenuation has a relatively weak frequency dependence, scattering attenuation possesses a 4^{th} order dependence on frequency and a 6^{th} order dependence on particle diameter that rapidly diminishes once

particles are of a size similar to that of the wavelength of incoming radiation. In terms of the parameters investigated in this study, synthetic modeling suggests that for frequencies and bubble sizes in the Rayleigh scattering range, relative increases in gas content (from bubbles) would be manifest as a frequency shift toward lower frequencies (indirect relationship) as higher frequencies are preferentially attenuated. We would expect to continue seeing these trends as bubbles continued to grow and/or coalesce until Mie scattering effects became significant (i.e., bubbles approached the size of the GPR wavelength). At this threshold, we would expect to see diminishing frequency dependence on bubble size.

Our approach is an attempt to use the unique attributes of scattering phenomena to estimate the average bubble radius based on changes in the shape and magnitude of the power spectra of GPR signals. Given the potential for mixed Rayleigh/Mie scattering effects, this method should provide reasonable estimates for gas bubble size given estimates of the absorption attenuation.

Figure 4.4 depicts different relationships between gas content and estimated bubble radii. In some cases, the average bubble size appears to decrease while the gas content increases, as seen in Figs. 4.4b and 4.4c, and to some extent in Figs. 4.4d, 4.4g, and 4.4i. This can be interpreted as the initial presence of larger pockets of trapped gas followed by the formation of many small bubbles. The pattern observed in Figs. 4.4e and 4.4h suggest that bubbles are on average coalescing or becoming larger.

The *Chen and Slater* [2015] lab data (Fig. 4.5) show smaller observed bubble radii on the side of the tank than those predicted through our estimation approach. In general, however, the predicted bubble radii follow a similar pattern to those observed on

the side of the tank, with larger bubble sizes estimated from both the GPR data and the hand drawing approach in the lower 10 – 20 cm depth regimes compared to the 0 – 10 cm depth regimes. This discrepancy is not necessarily surprising, however, given that bubbles observed on the side of the tank may not be representative of those existing within the center of the monolith.

Both lab studies were limited by the fact that detailed information on the electrical conductivity of the samples was absent, and were instead computed based on an assumed initial conductivity. Therefore, some error may be introduced as a result. Future studies should incorporate electrical conductivity monitoring to ensure absorption attenuation effects are well-quantified.

The field study (Fig. 4.7) indicates a decrease in gas content below 3 m (corresponding to a change in the level of decomposition observed in coring, Fig. 4.7a) coupled with a slight overall increase in the average bubble size. The overall average indicates bubbles of approximately 0.04 m radius. Such large bubbles may exist in peatlands, given that there is some evidence to suggest bubbles reach at least a meter in radius (i.e., *Comas et al., 2008*).

There is a very large estimated bubble radius (0.1 m) observed above the 3 m layer followed by the small bubble radius observed immediately below (0.01 m). This difference could be attributed to non gas-related objects (i.e., pieces of undecomposed material). Although some woody debris was encountered during coring in the lower 3 m (Fig. 4.7a), we consider this alternative unlikely as well given the overall more decomposed nature of this interval.

Although we have modeled scattering by spheres of gas in a peat soil, it is likely that large bubbles are not adequately represented as spheres, which may alter the anticipated scattering response. For instance, *Kettridge and Binley* [2008a] noted that larger bubbles seemed to become less spherical and tended to cluster in the vertical plane, and *Chen and Slater* [2015] observed large bubbles that were clearly not spherical in cross section. Nevertheless, we anticipate that relative changes in the power spectra, given a known overall gas content and after correction for absorption attenuation effects, provides an idea of the approximate bubble size in peat.

An additional consideration is that although we have corrected for geometrical spreading of energy in our preprocessing of the GPR signals in the examples used in this study, each trace cannot be considered representative of the straight line path between transmitter and receiver only. Therefore, estimates of the average bubble radius include the influence of attenuation effects outside of this direct path. In other words, bubbles or other heterogeneities from outside the straight raypath may act as primary or secondary scatterers of energy.

Future work could endeavor to model variations in bubble shape. Perhaps the most important next step, however, is to perform a similar experiment with known information on bubble size and electrical conductivity. Such information could be used to validate and/or calibrate the bubble size estimation procedure. However, the approach used here enables some inference on likely bubble size, and changes in bubble size, from GPR – information that is typically available by no other means *in situ* yet is increasingly recognized as an important control on ebullition dynamics.

4.6 Conclusions

Through synthetic modeling and evidence from lab and field data, we show that relative changes in the frequency power spectra from the non-noise dominated portions of GPR traces may yield information on gas bubble size dynamics. Further, we found evidence to suggest that large bubbles (i.e., ~ 0.04 m mean effective radius) may exist at a field site in Caribou Bog, Maine. The frequency dependent attenuation of GPR energy is a combination of absorption attenuation and scattering effects, however these effects can be theoretically modeled and used to estimate the average scatterer size. These findings have implications for the importance of bubble size with respect to gas dynamics in peatlands, and highlight the utility of GPR to provide additional information in this regard.

Chapter 5: Conclusions

5.1 Primary scientific findings

5.1.1 Updated models of gas dynamics

Results from the field studies provide evidence that both shallow and deep peat models are applicable to biogenic gas dynamics in Caribou Bog, Maine (shown as a schematic representation in Figure 5.1). While most biogenic gas activity (i.e., increases and decreases) are observed in the top meter of peat, it appears that large volumes of methane exist and are less frequently released from deeper regimes, particularly where some confining layer is present or a nutrient supply is available from below (facilitated by a permeable esker deposit in the case studied here). Consistent with previous research, drops in atmospheric pressure appear to be one of the main factors to trigger the sudden ebullition of gas.

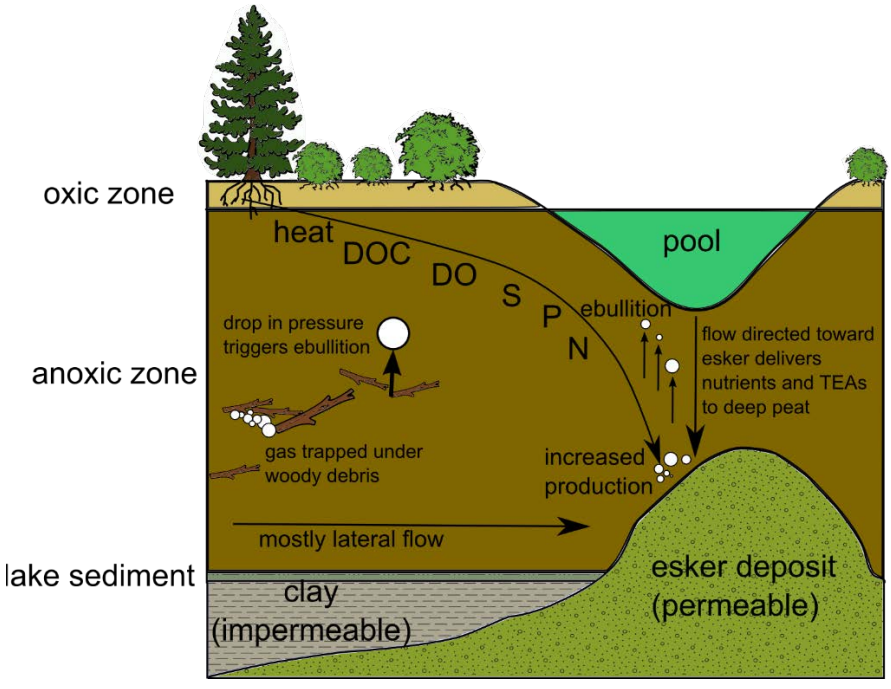

Figure 5.1 – combined gas dynamics model for the field sites investigated in Caribou Bog, Maine.

5.1.2 Gas bubble size estimates

Study of the likely size of gas bubbles (found to be on average 0.04 m in radius in this study) offers an early step in directly understanding the relationship between pressure and buoyancy forces, and may help to construct quantitative models of ebullition. These findings emphasize the importance of the deep peat as a reservoir for biogenic gases that may contribute a significant fraction of the overall methane flux to the atmosphere. Furthermore, these studies demonstrate the need for multimethod approaches for investigating biogenic gas dynamics in peatlands, as these processes occur at variable spatiotemporal scales.

5.2 Technical contributions

In addition to the scientific contributions mentioned above, the studies presented offer two key technical contributions for studying biogenic gas dynamics in peatlands.

5.2.1 Monitoring gas dynamics with autonomous ERI

First, a methodology for using autonomous ERI to study biogenic gas variations in peatlands. While ERI is not capable of directly estimating gas content, such data are invaluable as a proxy for viewing relative changes in gas content in 3D volumes at field-relevant scales (i.e., meters) and helps to bridge the scale gap between point based measurements and measurements at the km scale. The minimally invasive nature of ERI avoids disturbance of the peat and thus allows study of natural biogenic gas dynamics.

5.2.2 Bubble size estimation from GPR

Second, a simple model relating frequency dependent scattering attenuation of GPR signals to gas bubble radii in peatlands is developed (schematic representation and example in Figure 5.2). Information on the actual size of gas bubbles in peat is extremely limited due to technical limitations of direct methods. This method is therefore an

important contribution to the geophysical toolbox in regard to biogenic gas studies in peatlands. Further, this method is theoretically applicable to existing GPR datasets, and could shed new light on information already gathered from the lab and field.

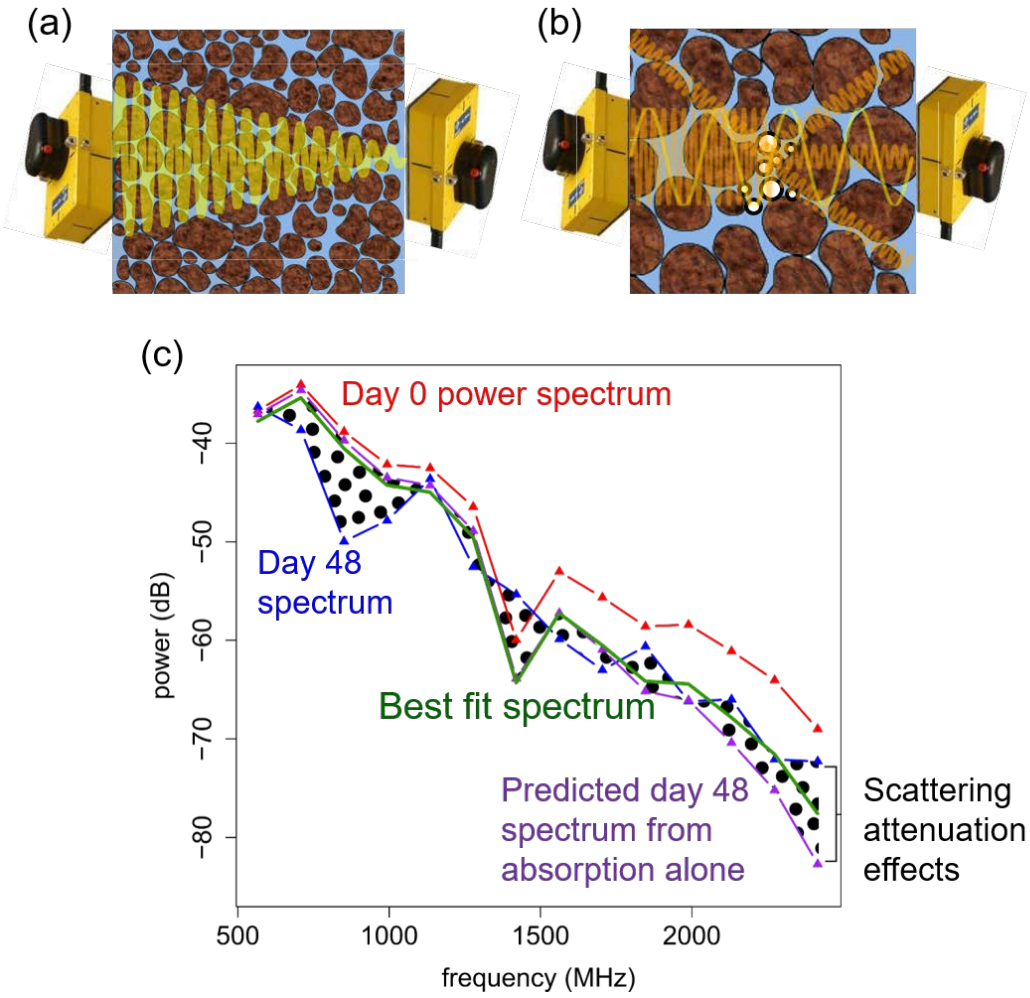

Figure 5.2 – (a) schematic representation of loss of GPR energy due to absorption and (b) loss of energy due to scattering. (c) bubble size estimation approach using time lapse GPR data (blue and red lines) and estimated absorption attenuation (purple line). The estimation procedure uses a Mie scattering model to compute the scattering contribution to total attenuation (absorption plus scattering) for a range of bubble sizes and selects bubble radii that best fit the change in the power spectrum between the two GPR datasets (green line).

5.3 Recommendations for future work

Although some significant advances have been made through this research, the study of biogenic gas dynamics in peatlands remains a field of opportunity for future study.

5.3.1 Development of peat specific petrophysical models

There is a need for further controlled laboratory studies relating geophysical parameters to biogenic gas properties. In this work, ERI is used to infer qualitative changes in gas content over a 3D volume in a natural peatland, but this approach is somewhat limited by the fact that Archie's Law is likely unsuitable for peat soils [*Comas and Slater*, 2004; *Slater et al.*, 2007; *Kettridge et al.*, 2011], given that surface conduction and electrical conduction effects also influence the bulk resistivity estimated by ERI. While *Comas and Slater* [2004] developed models to predict changes in pore water conductivity and porosity through ERI (coupled with additional induced polarization measurements), further work is needed to adapt these models to the context of gas dynamics. In particular, published induced polarization results from peatlands at the field scale are limited [*Slater and Reeve*, 2002]. An attempt was made during this PhD work to collect such data in the field, but I found that inversions yielded unrealistic results – it would seem the methodology for collecting reliable induced polarization data in peatlands is a task worthy of further investigation, given the potential of this method to provide information on fluid conductivity and porosity.

Second, this work presents a physically-based model that relates changes in shape of the power spectrum from a GPR signal to changes in spherical gas bubble radius. A

direct follow up study would be to employ the gas bubble size estimation approach under conditions where the size of the bubbles could be directly monitored, perhaps beginning with only a tank of water and a means to inject and trap gas (i.e., a gas valve at the bottom removable shelves along the side of the tank). By performing such a study, scattering attenuation could be more readily constrained (by removing the effect of peat heterogeneity).

5.3.2 Studies of the deep peat

Another research need is for studies focusing on the deep peat. Although geophysical methods offer useful indirect information on gas content and dynamics from deep peat, there is limited direct information available from deep peat to validate these findings. The two limitations of direct methods for assessing gas content are (1) invasiveness (and thus disturbance of natural processes) and (2) spatial scale (direct measurements are typically limited to very local scale on the order of cm). Despite these limitations, such measurements provide crucial information to understand the probable causes for anomalies observed in geophysical data. Along these lines, biological and geochemical data from deep peat would also be highly useful in understanding the probable causes of biogenic gas content variations.

5.3.3 Incorporation of other geophysical monitoring tools

Nuclear magnetic resonance (NMR) is a geophysical technology that is highly sensitive to water content and has great potential to study biogenic gas processes in peat, but has not yet been included in the arsenal of geophysical tools used toward this end. While NMR has long been used in resources exploration, this technology has only recently seen use in environmental investigations, and instruments are available for lab analysis as well as field surface and borehole deployment. It should be noted, however,

that field NMR field instruments require large wire loops (on the order of 100 m) and surveys are typically carried out as 1D soundings, which cannot resolve horizontally heterogeneous features. More research is therefore needed to develop NMR tools for time-lapse monitoring of near surface processes, including peatland gas content variations.

Induced polarization (IP) is sensitive to the capacitive properties of materials. Similarly, spectral induced polarization (SIP) examines how charge storage varies at different frequencies. Both methods use a similar acquisition scheme as ERI but require specialized equipment. It is already mentioned above that more work is needed to develop IP for peatland studies, and the use of SIP has seen only slight attention. *Comas and Slater* [2004] collected SIP data (0.1 – 1000 Hz) on several peat samples, however information was presented in terms of a single frequency (1 Hz) and the spectral response was not explored. Also, *Weller et al.*, 2006 demonstrated the use of SIP as a viable method to detect large wooden archeological relics in peatlands, however environmental processes were not investigated as part of this research. Further work could therefore attempt to develop links between SIP data and peat biogeochemistry, textural characteristics, and/or hydraulic properties, which could in turn serve to enhance the understanding of drivers of biogenic gas dynamics.

5.3.4 Bridging the scale gap: relating biogenic gas dynamics across spatiotemporal scales

It is crucial to understand how biogenic gas processes propagate from the local (point) scale up to the global scale if process-based models are to be successfully used for climate model calibration and simulation. The 'ideal' scenario is to be able to make

accurate, high resolution predictions on peatland gas uptake and release based on existing datasets, but it is impossible to gather detailed point-based measurements across all peatlands throughout the world. The work presented in this thesis represents an important step in upscaling from local to intermediate-scale (i.e., geophysical measurements on the order of sub meter to tens of meters scale) observations of gas dynamics, but there is also the additional step of understanding how these intermediate scale datasets can be integrated into remote, satellite-based observations.

5.3.5 More field datasets and access to those datasets

It has been shown in chapter 3 of this thesis that the underlying hydrogeology and peat physical properties play a critical role in biogenic gas dynamics. However, these types of measurements (namely, GPR and ERI) remain limited to a few select areas across the world. Collecting such measurements could yield important information on how peat properties and biogenic gas processes compare/contrast. During this PhD, I have had the opportunity to participate in collecting some preliminary geophysical data from peatlands at several sites in Indonesia and in the Ecuadorian Páramo. These data are immediately useful in determining the suitability of geophysical technologies for future study.

Additionally, it is important that researchers seeking to perform these kinds of research have open access to data that have already been acquired. Some efforts have been made to this end already, but are far from comprehensive in terms of incorporating existing data. For example, the Holocene Perspective on Peatland Biogeochemistry (https://peatlands.lehigh.edu/) [*Loisel et al.*, 2014] currently includes a searchable map with data from 268 peat cores from 215 sites in the northern hemisphere. The

International Mire Conservation Group's Global Peatland Database (http://www.imcg.net/pages/publications/imcg-materials.php) provides general information on individual countries in Africa and Asia, and some countries house databases specifically for peatlands (for example, the Peatlands of Canada database). However, there is no project that synthesizes the many types of data collected from peatlands. Admittedly, such a project would require cooperation from many entities, not to mention dedicated staff, time and monetary resources to keep such a database organized and operational.

References

Akaike, H. (1974), A new look at the statistical model identification, *IEEE Trans. Autom. Control*, 19, 716–723.

Almquist-Jacobson, H. and D. Sanger (1999), Paleogeographic changes in wetland and upland environments in the Mildford Drainage basin of central Maine, in relation to Holocene human settlement in history. In: *Current Northeast Paleoethnobotany*, edited by J. Hart, pp. 177-190, New York State Museum Bulletin.

Altor, A. E., and W. J. Mitsch (2006), Methane flux from created riparian marshes: Relationship to intermittent versus continuous inundation and emergent macrophytes, Ecological Engineering, 28(3), 224-234, doi:10.1016/j.ecoleng.2006.06.006.

Baird, A.J., C.W. Beckwith, S. Waldron, and J.M. Waddington (2004), Ebullition of methane-containing gas bubbles from near-surface *Sphagnum* peat, *Geophys. Res. Lett.*, *31*, L21505, doi:10.1029/2004GL021157.

Beckwith, C.W. and A.J. Baird (2001), Effect of biogenic gas bubbles on water flow through poorly decomposed blanket peat, *Water Resour. Res.*, 37, 551–558.

Bellisario, L. M., J. L. Bubier, T. R. Moore, and J. P. Chanton (1999), Controls on CH_4 emissions from a northern peatland, *Global Biogeochem. Cycles*, 13(1), 81–91, doi: 10.1029/1998GB900021.

Binley, A., and A. Kemna (2005), Electrical Methods, In: *Hydrogeophysics, Water Science and Technology Library*, vol. 50, edited by Y. Rubin and S.S. Hubbard, pp. 129-156, Springer, Dordrecht, Netherlands, doi: 10.1007/1-4020-3102-5.

Binley, A., P. Winship, L. J. West, M. Pokar, and R. Middleton (2002), Seasonal variation of moisture content in unsaturated sandstone inferred from borehole radar and resistivity profiles, *J. Hydrol.*, 267, 160–172, doi:10.1016/S0022-1694(02)00147-6.

Birchak, J.R., C.G. Gardner, J.E. Hipp, and J.M. Victor (1974), High Dielectric Constant Microwave Probes for Sensing Soil Moisture, *Proceedings of the IEEE,* 62(1), 93–98, doi:10.1109/PROC.1974.9388.

Blodau, C. (2002), Carbon cycling in peatlands - A review of processes and controls, Environ. Rev., 10 (2), 111–134, doi: 10.1139/a02-004.

Bloom, A.L. (1963), Late-Pleistocene Fluctuations of Sealevel and Postglacial Crustal Rebound in Coastal Maine, *American Journal of Science*, 261(9), 862-879, doi: 10.2475/ajs.261.9.862.

Boelter, D. H. (1969), Physical properties of peats as related to degree of decomposition, *Soil Sci. Soc. Am. J.*, 33, 606–609.

Bohren, C.F. and D.R. Huffman (1998), *Absorption and Scattering of Light by Small Particles*, Wiley-Interscience, New York, NY.

Bon, C. E., A. S. Reeve, L. Slater, and X. Comas (2014), Using hydrologic measurements to investigate free-phase gas ebullition in a Maine peatland, USA, *Hydrol. Earth Syst. Sci.*, 18, 953-965, doi:10.5194/hess-18-953-2014.

Borns, H.W., Preliminary report on the age and distribution of the late Pleistocene ice in north central Maine, American Journal of Science, 261(8), 738-740, doi: 10.2475/ajs.261.8.738.

Bradford, J. (2007), Frequency-dependent attenuation analysis of ground-penetrating radar data, *Geophysics*, 72 (3), J17-J16, doi: 10.1190/1.2710183.

Bridgham, S.D., H. Cadillo-Quiroz, J. K. Keller, and Q. Zhuang (2013), Methane emissions from wetlands: biogeochemical, microbial, and modeling perspectives from local to global scales, *Glob. Chang. Biol.*, 19(5), 1325–46.

Brown, A., S. P. Mathur, and D. J. Kushner (1989), An ombrotrophic bog as a methane reservoir, Global Biogeochem. Cycles, 3, 205–213.

Cameron, C.C., M.K. Mullen, C.A. Lepage, and W.A. Anderson (1984), *Peat Resources of Maine*, p. 124, Maine Geological Survey Bulletin.

Chanton, J. P., J. Bauer, P. H. Glaser, D. I. Siegel, C. Kelley, S. C. Tyler, E. A. Romanowicz, and A. Lazrus (1995), Radiocarbon evidence for the substrates supporting methane formation within northern Minnesota peatlands, *Geochim. Cosmochim. Acta*, 59, 3663– 3688.

Charman, D.J. (2002), *Peatlands and Environmental Change*, John Wiley and Sons Ltd., Chichester, NH.

Chasar, L. C. (2002), Implications of Environmental Change for Energy Flow Through Natural Systems: Wetlands and Coastal Systems, Ph.D. dissertation, Dep. of Oceanography, Florida State Univ., Tallahassee, Florida.

Chasar, L. S., J. P. Chanton, P. H. Glaser, D. I. Siegel, and J. S. Rivers (2000a), Radiocarbon and stable carbon isotopic evidence for transport and transformation of dissolved organic carbon, dissolved inorganic carbon, and CH_4 in a northern Minnesota peatland, *Global Biogeochem. Cycles*, 14, 1095–1108.

Chasar, L. S., J. P. Chanton, P. H. Glaser, and D. I. Siegel (2000b), Methane concentration and stable isotope distribution as evidence of rhizospheric processes: Comparison of a fen and bog in the Glacial Lake Agassiz peatland complex, *Ann. Bot. London*, 86, 655–663.

Chason, D. B., and D. I. Siegel, D.I., 1986. Hydraulic conductivity and related physical properties of peat, lost river peatland, Northern Minnesota, *Soil Sci.*, 142, 91–99.

Chen, X., and L. Slater (2015), Gas bubble transport and emissions for shallow peat from a northern peatland: The role of pressure changes and peat structure, *Water Resour. Res.*, 51, 151–168, doi: 10.1002/2014WR016268.

Cheng, S.-W., T. K. Dey, H. Edelsbrunner, M. A. Facello, and S.-H. Teng (1999), Sliver exudation, *Proceedings of the fifteenth annual symposium on Computational geometry*, 1–13, doi: 10.1145/304893.304894.

Christensen, T. R., A. Ekberg, L. Ström, M. Mastepanov, N. Panikov, M. Öquist, B. H. Svensson, H. Nykänen, P. J. Martikainen, and H. Oskarsson (2003), Factors controlling large scale variations in methane emissions from wetlands, *Geophys. Res. Lett.*, 30(7), 1414, doi:10.1029/2002GL016848.

Comas, X., and L. Slater (2004), Low-frequency electrical properties of peat, *Water Resour. Res.*, 40, W12414, doi:10.1029/2004WR003534.

Comas, X., and L. Slater (2007), Evolution of biogenic gases in peat blocks inferred from noninvasive dielectric permittivity measurements, *Water Resour. Res.*, 43, W05424, doi:10.1029/2006WR005562.

Comas, X., and W. Wright (2012), Heterogeneity of biogenic gas ebullition in subtropical peat soils is revealed using time-lapse cameras, Water Resour. Res., 48, W04601, doi:10.1029/2011WR011654.

Comas, X., and W. Wright (2014), Investigating carbon flux variability in subtropical peat soils of the Everglades using hydrogeophysical methods, *J. Geophys. Res. Biogeosci.*, 119, 1506–1519, doi: 10.1002/2013JG002601.

Comas, X., L. Slater, and A. Reeve (2004), Geophysical evidence for peat basin morphology and stratigraphic controls on vegetation observed in a northern peatland, *J. Hydrol.*, 295, 173–184.

Comas, X., L. Slater, and A. Reeve (2005a), Spatial variability in biogenic gas accumulations in peat soils is revealed by ground penetrating radar (GPR), *Geophys. Res. Lett.*, 32, L08401, doi:10.1029/2004GL022297.

Comas, X., L. Slater, and A. Reeve (2005b), Stratigraphic controls on pool formation in a domed bog inferred from ground penetrating radar (GPR), *J. Hydrol.*, 315 (1 – 4), 40 – 51, doi:10.1016/j.jhydrol.2005.04.020.

Comas, X., L. Slater, and A. Reeve (2005c), Geophysical and hydrological evaluation of two bog complexes in a northern peatland: Implications for the distribution of biogenic gases at the basin scale, *Global Biogeochem. Cycles*, 19, GB4023, doi:10.1029/2005GB002582.

Comas, X., L. Slater, and A. Reeve (2008), Seasonal geophysical monitoring of biogenic gases in a northern peatland: Implications for temporal and spatial variability in free phase gas production rates, *J. Geophys. Res.*, 113, G01012, doi:10.1029/2007JG000575.

Comas, X., L. D. Slater, and A. S. Reeve (2011a), Atmospheric pressure drives changes in the vertical distribution of biogenic free-phase gasses in a northern peatland, *J. Geophys. Res.*, 116, G04014, doi:10.1029/ 2011JG001701.

Comas, X., L. D. Slater, and A. S. Reeve (2011b), Pool patterning in a northern peatland: Geophysical evidence for the role of postglacial landforms, *Journal of Hydrology*, 399 (3-4), 173-184, doi:10.1016/j.jhydrol.2010.12.031.

Comas X., N. Kettridge, A. Binley, L. Slater, A. Parsekian, A. J. Baird, M. Strack, and J. M. Waddington (2014), The effect of peat structure on the spatial distribution of biogenic gases within bogs, *Hydrol. Process.*, 28, 5483–5494, doi: 10.1002/hyp.10056.

Comas, X., N. Terry, L. Slater, M. Warren, R. Kolka, A. Kristiyono, N. Sudiana, D. Nurjaman, and T. Darusman (2015), Imaging tropical peatlands in Indonesia using ground-penetrating radar (GPR) and electrical resistivity imaging (ERI): implications for carbon stock estimates and peat soil characterization, Biogeosciences, 12, 2995-3007, doi:10.5194/bg-12-2995-2015.

Cooley, J., and J. Tukey (1965), An Algorithm for the Machine Calculation of Complex Fourier Series, *Mathematics of Computation*, 19(90), 297-301.

Coulthard, T., A. J. Baird, J. Ramirez, and J. M. Waddington (2009), Methane dynamics in peat: The importance of shallow peats and a novel reduced-complexity approach for modeling ebullition, in: *Carbon Cycling in Northern Peatlands*, edited by A. J. Baird et al., 299 pp., AGU, Washington, DC.

Crill, P. M., K. B. Bartlett, R. C. Harriss, E. Gorham, E. S. Verry, D. I. Sebacher, L. Madzar, and W. Sanner (1988), Methane flux from Minnesota peatlands, *Global Biogeochem. Cycles*, 2(4), 371–384.

Crill, P. M., K. B. Bartlett, and N. T. Roulet (1992), Methane flux from boreal peatlands, *Suo*, 43, 173–182.

Daily, W., A. Ramirez, and A. Binley (2004), Remote monitoring of leaks in storage tanks using electrical resistance tomography: Application at the Hanford Site, *J. Environ. Eng. Geophys.*, 9, 11–24.

Davis, J. L. and A. P. Annan (1989), Ground-penetrating radar for high resolution mapping of soil and rock stratigraphy, *Geophysical Prospecting*, 37, 531-551.

Davis, R. B. and D.S. Anderson (1999), A numerical method and supporting database for evaluation of Maine peatlands as candidate natural areas, *Technical Bulletin 175*, pp. 166, University of Maine, Maine Agricultural and Forest Experiment Station.

DelSontro, T., D. F. McGinnis, B. Wehrli, and I. Ostrovsky (2015), Size Does Matter: Importance of Large Bubbles and Small-Scale Hot Spots for Methane Transport, *Environmental Science & Technology*, 49 (3), 1268-1276, doi: 10.1021/es5054286.
Grimm, R. E., E. Heggy, S. Clifford, C. Dinwiddie, R. McGinnis, and D. Farrell (2006), Absorption and scattering in ground-penetrating radar: Analysis of the Bishop Tuff, *J. Geophys. Res.*, 111, E06S02, doi:10.1029/2005JE002619.

Dias, A. T. C., B. Hoorens, R. S. P. Van Logtestijn, J. E. Vermaat, and R. Aerts (2010), Plant species composition can be used as a proxy to predict methane emissions in peatland ecosystems after land-use changes, *Ecosystems*, 13, 526–38, doi: 10.1007/s10021-010-9338-1.

Dijkstra, F. A., S. A. Prior, G. B. Runion, H. A. Torbert, H. Tian, C. Lu, R. T. Venterea (2012), Effects of elevated carbon dioxide and increased temperature on methane and nitrous oxide fluxes: evidence from field experiments, *Front. Ecol. Environ.*, 10(10), 520-527, doi: 10.1890/120059.

Dix, C.H. (1955), Seismic velocities from surface measurements, *Geophysics*, 20, 68-86.

DelSontro, T., D. F. McGinnis, B. Wehrli, and I. Ostrovsky (2015), Size Does Matter: Importance of Large Bubbles and Small-Scale Hot Spots for Methane Transport, *Environmental Science & Technology*, 49 (3), 1268-1276, doi: 10.1021/es5054286.
Grimm, R. E., E. Heggy, S. Clifford, C. Dinwiddie, R. McGinnis, and D. Farrell (2006), Absorption and scattering in ground-penetrating radar: Analysis of the Bishop Tuff, *Journal of Geophysical Research*, 111, 1–15, doi: 10.1029/2005JE002619.

Drake, H. L., Horn, M. A., and Wüst, P. K. (2009). Intermediary ecosystem metabolism as a main driver of methanogenesis in acidic wetland soil, *Environ. Microbiol. Rep.*, 1(5), 307–318, doi: 10.1111/j.1758-2229.2009.00050.x.

Dunfield, P., K. Knowles, R. Dumont, and T. Moore (1993), Methane production and consumption in temperate and subarctic peat soils: Response to temperature and pH, *Soil Biol. Biochem.*, 25, 321–326.

Eriksson, T., M. G. Öquist, *and* M. B. Nilsson *(*2010*),* Effects of decadal deposition of nitrogen and sulfur, and increased temperature, on methane emissions from a boreal peatland*, J. Geophys. Res.,* 115(G4)*, doi:* 10.1029/2010JG001285.

Forster, P., V. Ramaswamy, P. Artaxo, T. Berntsen, R. Betts, D.W. Fahey, J. Haywood, J. Lean, D.C. Lowe, G. Myhre, J. Nganga, R. Prinn, G. Raga, M. Schulz, and R. Van Dorland (2007), Changes in Atmospheric Constituents and in Radiative Forcing, In: *Climate Change 2007: The Physical Science Basis . Contribution of Working Group I to the Fourth Assessment Report of the Intergovernmental Panel on Climate Change*, edited by S. Solomon, D. Qin, M. Manning, Z. Chen, M. Marquis, K. B. Averyt, M. Tignor, and H. L. Miller, Cambridge University Press, Cambridge, United Kingdom and New York, NY, USA.

Fritsch, F. N., and R. E. Carlson (1980), Monotone piecewise cubic interpolation, *SIAM Journal on Numerical Analysis*, 17, 238–246.

Frolking, S., N.T. Roulet, and J. Fuglestvedt (2006), How northern peatlands influence the Earth's radiative budget: sustained methane emission versus sustained carbon sequestration, *J. Geophys. Res.*, 111, G01008, doi: 10.1029/2005JG000091.

Gao, J. Q., H. Ouyang, G. C. Lei, X. L. Xu, and M. X. Zhang (2011), Effects of temperature, soil moisture, soil type and their interactions on soil carbon mineralization in Zoigê alpine wetland, Qinghai-Tibet Plateau, *Chin. Geogr. Sci.*, 21, 27-35.

Gålfalk, M., G. Olofsson, P. Crill, and D. Bastviken (2015), Making methane visible, *Nature Clim. Change,* doi:10.1038/nclimate2877.

Geuzaine, C., and J. F. Remacle (2009), Gmsh: A 3-D Finite Element Mesh Generator with Built-in Pre- and Post- processing Facilities, *International Journal for Numerical Methods in Engineering*, 79(11), 1309–1331, doi: 10.1002/nme.2579.

Glaser, P. H., J. P. Chanton, P. Morin, D. O, Rosenberry, D. I. Siegel, O. Ruud, L. I. Chasar, and A. S. Reeve (2004), Surface deformations as indicators of deep ebullition fluxes in a large northern peatland, *Global Biogeochemical Cycles*, 18, GB1003.

Grover, S. P. P., and J. A. Baldock (2013), The link between peat hydrology and decomposition: Beyond von Post, *J. Hydrol.*, 479, 130–138, doi:10.1016/j.jhydrol.2012.11.049.

Harbi, H. and G. A. McMechan (2012), Conductivity and scattering Q in GPR data: Example from the Ellenburger dolomite, central Texas, *Geophysics*, 77(4), H63 – H78, doi: 10.1190/GEO2011-0337.1.

Hayley, K., L. R. Bentley, M. Gharibi, and M. Nightingale (2007), Low temperature dependence of electrical resistivity: Implications for near surface geophysical monitoring, *Geophysical Research Letters*, 34, L18402.

Hayley, K., L. R. Bentley, and M. Gharibi (2009), Time-lapse electrical resistivity monitoring of salt-affected soil and groundwater, *Water Resour. Res.,* 45, W07425, doi: 10.1029/2008WR007616.

Hilhorst, M. A. (2000), A Pore Water Conductivity Sensor, *Soil Science Society of America Journal*, 64(6), *1922-1925*.

Hodson, E. L., B. Poulter, N. E. Zimmermann, C. Prigent, and J. O. Kaplan (2011), The El Niño-Southern Oscillation and wetland methane interannual variability, *Geophys. Res. Lett.*, 38(8), L08810, doi: 10.1029/2011GL046861.

Hornibrook, E. R. C., F. J. Longstaffe, and W. S.Fyfe (1997), Spatial distribution of microbial methane production pathways in temperate zone wetland soils: Stable carbon and hydrogen isotope evidence, *Geochim. Cosmochim. Acta*, 61, 745–753, doi:10.1016/S0016-7037(96)00368-7.

Hu, F.S. and R.B. Davis (1995), Postglacial development of a Maine bog and paleoenviromental implications, *Canadian Journal of Botany*, 73, 638–649.

Jaatinen, K., H. Fritze, J. Laine, and R. Laiho (2007), Effects of short- and long-term water-level drawdown on the populations and activity of aerobic decomposers in a boreal Peatland, *Global Change Biol*., 13, 491–510, doi: 10.1111/j.1365-2486.2006.01312.x.

Jackowicz-Korczyski, M., T. R. Christensen, K. Bäckstrand, P. Crill, T. Friborg, M. Mastepanov, and L. Ström (2010), Annual cycle of methane emission from a subarctic peatland, *J. Geophys. Res.*, 115, G02009, doi: 10.1029/02008JG000913.

Johnson, T. C., L. Slater, D. Ntarlagiannis, F. D. Day-Lewis, and M. Elwaseif (2012), Monitoring groundwater-surface water interaction using time-series and time-

frequency analysis of transient three-dimensional electrical resistivity changes, *Water Resour. Res.*, 48, W07506, doi: 10.1029/2012WR011893.

Jol, H. M., and D. G. Smith (1995), Ground penetrating radar surveys of peatlands for oilfield pipelines in Canada, *J. Appl. Geophys.*, 34 (2), 109 – 123.

Keller, J. K. S. D. and Bridgham (2007), Pathways of anaerobic carbon cycling across an ombrotrophic-minerotrophic peatland gradient, *Limnol. Oceanogr.*, 52, 96–107, doi: 10.4319/lo.2007.52.1.0096.

Kellner, E., J. M. Waddington, and J. S. Price (2005), Dynamics of biogenic gas bubbles in peat: Potential effects on water storage and peat deformation, *Water Resour. Res.*, 41, W08417, doi:10.1029/2004WR003732.

Kellner, E., A. J. Baird, M. Oosterwoud, K. Harrison, and J. M. Waddington (2006), The effect of temperature and atmospheric pressure on methane (CH_4) ebullition from near-surface peats. *Geophysical Research Letters*, 33, L18405.

Kettridge, N. and A. Binley (2011), Characterization of peat structure using X-ray computed tomography and its control on the ebullition of biogenic gas bubbles, *Journal of Geophysical Research*, 116(G01024), doi:10.1029/2010JG001478.

Kettridge, N. and A. Binley (2008), X-ray computed tomography of peat soils: measuring gas content and peat structure. *Hydrol. Process.*, 22, 4827 – 4837, doi: 10.1002/hyp.7097.

Kettridge, N., X. Comas, A. Baird, L. Slater, M. Strack, D. Thompson, H. Jol, and A. Binley (2008), Ecohydrologically important subsurface structures in peatlands revealed by ground-penetrating radar and complex conductivity surveys, *J. Geophys. Res.*, 113, G04030, doi:10.1029/2008JG000787.

Kettridge, N., A. Binley, S. M. Green, and A. J. Baird (2011), Ebullition Events Monitored from Northern Peatlands Using Electrical Imaging, *Journal of Geophysical Research*, 116(G4), 1–14, doi: 10.1029/2010JG001561.

Klapstein, S. J., M. R. Turetsky, A. D. McGuire, J. W. Harden, C. I. Czimczik, X. Xu, J. P. Chanton, and J. M. Waddington (2014), Controls on methane released through ebullition in peatlands affected by permafrost degradation, J. Geophys. Res. Biogeosci., 119, 418–431, doi:10.1002/2013JG002441.

Koestel, J., A. Kemna, M. Javaux, A. Binley, and H. Vereecken (2008), Quantitative imaging of solute transport in an unsaturated and undisturbed soil monolith with 3-D ERT and TDR. *Water Resour. Res.* 44(17), doi: 10.1029/2007WR006755.

Kotowska, M. M., and F. A. Werner (2013), Environmental controls over methane emissions from bromeliad phytotelmata: The role of phosphorus and nitrogen

availability, temperature, and water content, *Global Biogeochem. Cycles*, 27, 1186–1193, doi:10.1002/2013GB004612.

Krautblatter, M., and C. Hauck (2007), Electrical resistivity tomography monitoring of permafrost in solid rock walls, *J. Geophys. Res.,* 112, F02S20, doi:10.1029/2006JF000546.

LaBrecque, D. and X. Yang (2001), Difference Inversion of ERT Data: Fast Inversion Method for 3-D In Situ Monitoring, *Journal of Environmental and Engineering Geophysics*, 6(2), 83-89.

LaBrecque, D.J., M. Miletto, W. Daily, A. Ramirez, and E. Owen (1996), The effects of noise on Occam's inversion of resistivity tomography data, *Geophysics*, 61, 538–548.

Lai, D. Y. F., T. R. Moore, and N. T. Roulet (2014), Spatial and temporal variations of methane flux measured by autochambers in a temperate ombrotrophic peatland, *J. Geophys. Res. Biogeosci.*, 119, 864–880, doi: 10.1002/2013JG002410.

Laine, A., D. Wilson, G. Kiely, and K. A. Bryne (2007), Methane flux dynamics in an Irish lowland blanket bog, *Plant Soil*, 299, 181–193.

Laine, A. M., K. A. Byrne, G. Kiely, E. S. Tuittila (2009), The short-term effect of altered water level on carbon dioxide and methane fluxes in a blanket bog, *Suo*, 60, 65-83.

Laing, C. G., T. G. Shreeve, and D. M. E. Pearce (2008), Methane bubbles in surface peat cores: In situ measurements, *Global Change Biol.*, *14*, 916–924, doi:10.1111/j.13652486.2007.01534.x.

Lambot, S., E. C. Slob, I. van den Bosch, B. Stockbroeckx, B. Scheers, and M. Vanclooster (2004), Estimating soil electric properties from monostatic ground-penetrating radar signal inversion in the frequency domain, *Water Resour. Res.*, 40, W04205, doi:10.1029/2003WR002095.

Lichtenecker, K., and K. Rother (1931), Die Herleitung des logarithmischen Mischungsgesetz es aus allgemeinen Prinzipien der stationären Strömung: Physikalische Zeitschrift, 32, p. 255–260.

Liu, L., J. W. Lane, and Y. Quan (1998), Radar attenuation tomography using the centroid frequency downshift method, *Journal of Applied Geophysics*, 40, 105–116, doi: 10.1016/S0926-9851(98)00024-X.

Loisel, J., Z. Yu, A. Parsekian, J. Nolan, and L. Slater (2013), Quantifying landscape morphology influence on peatland lateral expansion using ground penetrating radar (GPR) and peat core analysis, *J. Geophys. Res. Biogeosci.*, 118, 373 – 384, doi:10.1002/jgrg.20029.

Loisel, J., et al. (2014), A database and synthesis of northern peatland soil properties and Holocene carbon and nitrogen accumulation, Holocene, 24(9), 1028–1042.

Lowry, T., M. B. Allen, and P. N. Shive (1989), Singularity removal; a refinement of resistivity modeling techniques, *Geophysics*, 54(6), 766-774, doi: 10.1190/1.1442704.

Manahan, S. E. (2000), *Environmental Chemistry 7th edition,* 914 pp., CRC Press, Boca Raton, Florida.

Mastepanov, M. and T. R. Christensen (2009), Laboratory investigations of methane buildup in, and release from, shallow peats, In: *Northern Peatlands and Carbon Cycling*, edited by A.J. Baird, L.R. Belyea, X. Comas, A. Reeve, and L.D. Slater, pp. 205–218, AGU, Washington D. C.

Mätzler, C., *MATLAB Functions for Mie Scattering and Absorption*, Institut für Angewandte Physik, Research Report No. 2002-08, Bern, Switzerland, 2002.

McDermitt, D., G. Burba, L. Xu, T. Anderson, A. Komissarov, B. Riensche, J. Schedlbauer, G. Starr, D. Zona, W. Oechel, S. Oberbauer, and S. Hastings (2011), A new low-power, open-path instrument for measuring methane flux by eddy covariance, *Appl. Phys. B*, 102, 391-405.

McKenzie, J. M., D. I. Siegel, D. O. Rosenberry, P. H. Glaser, and C. I. Voss (2007), Heat transport in the Red Lake Bog, Glacial Lake Agassiz Peatlands. *Hydrol. Process.*, 21, 369–378, doi: 10.1002/hyp.6239.

Mitsch,W. J. and J.G. Gosselink (2007), *Wetlands*, Wiley, Hoboken, N.J., 2007.

Moore, T. R., and M. Dalva (1993), The influence of temperature and water table position on carbon dioxide and methane emissions from laboratory columns of peatland soils, *J. Soil Sci.*, 44, 651–664.

Moore, T. R. and N. Basiliko (2006), Decomposition in boreal peatlands, In: *Boreal Peatland Ecosystems*, edited by R. K. Wieder and D. H. Vitt, pp. 125–144, Springer-Verlag, Berlin Heidelberg, doi: 10.1007/978-3-540-31913-9_7.

Moore, T. R., A. De Young, J. Bubier, E. Humphreys, P. Lafleur, and N. Roulet (2011), A multi-year record of methane flux at the Mer Bleue bog, southern Canada, *Ecosystems*, 14(4), 646–657.

Morris, P. J., A. J. Baird, and L. R. Belyea (2015), Bridging the gap between models and measurements of peat hydraulic conductivity, *Water Resour. Res.*, 51, 5353–5364, doi:10.1002/2015WR017264.

Osberg, P. H., A. M. Hussey II, and G. M. Boone (1985), Bedrock geologic map of Maine, 1:500,000, *Maine Geological Survey*, Maine Department of Conservation.

Ours, D. P., D. I. Siegel, and P. H. Glaser (1997), Chemical dilation and the dual porosity of humified bog peat, *J. Hydrol.*, 196, 348–360.

Papa, F., C. Prigent, F. Aires, C. Jimenez, W. B. Rossow, and E. Matthews (2010), Interannual variability of surface water extent at the global scale, 1993–2004, *J. Geophys. Res.*, 115(D12), doi: 10.1029/2009JD012674.

Parish, F., A. Sirin, D. Charman, H. Joosten, T. Minayeva, M. Silvius, and L. Stringer (2008), Assessment on Peatlands, Biodiversity and Climate Change: Main Report, Global Environment Centre, Kuala Lumpur and Wetlands International, Wageningen, Netherlands.

Parrenin, F., V. Masson-Delmotte, P. Köhler, D. Raynaud, D. Paillard, J. Schwander, C. Barbante, A. Landais, A. Wegner, and J. Jouzel (2013), Synchronous change of atmospheric CO_2 and Antarctic temperature during the last deglacial warming, *Science*, 339(6123), 1060-1063, doi: 10.1126/science.1226368.

Parry, L. E., L. J. West, J. Holden, and P. J. Chapman (2014), Evaluating approaches for estimating peat depth, *J. Geophys. Res. Biogeosci.*, 119, doi:10.1002/2013JG002411.

Parsekian, A. D., L. Slater, X. Comas, and P. H. Glaser (2010), Variations in free-phase gases in peat landforms determined by ground penetrating radar, *J. Geophys. Res.*, 115, G02002, doi: 10.1029/2009JG001086.

Parsekian, A. D., X. Comas, L. Slater, and P. H. Glaser (2011), Geophysical evidence for the lateral distribution of free-phase gas at the peat basin scale in a large northern peatland, *J. Geophys. Res.*, 116, G03008, doi: 10.1029/2010JG001543.

Parsekian, A. D., L. Slater, S. Sebestyen, R. Kolka, D. Ntarlagiannis, J. Nolan and P.J. Hanson (2012a), Uncertainty in Peat Volume and Soil Carbon Estimated using Ground-Penetrating Radar and Probing. *Soil Science Society of America Journal*, 76 (5), 1911 – 1918. doi:10.2136/sssaj2012.0040.

Parsekian, A. D., L. Slater, and D. Gimenéz (2012b), Application of ground penetrating radar to measure near-saturation soil water content in peat soils, *Water Resour. Res.*, 48, W02533, doi: 10.1029/2011WR011303.

Paul, S., K. Küsel, and C. Alewell (2006), Reduction processes in forest wetlands: tracking down heterogeneity of source/sink functions with a combination of methods, *Soil Biol. Biochem,*, 38, 1028–1039, doi:10.1016/j.soilbio.2005.09.001.

Price, J. S. (2003), Role and character of seasonal peat soil deformation on the hydrology of undisturbed and cutover peatlands, *Water Resour. Res.*, 39(9), 1241, doi: 10.1029/2002WR001302.

Quinton, W. L., M. Hayashi, and S. K. Carey (2008), Peat hydraulic conductivity in cold regions and its relation to pore size geometry, *Hydrol. Processes*, 22, 2829–2837, doi:10.1002/hyp.7027.

Ramirez, J. A., A. J. Baird, and T. J. Coulthard (2016), The effect of pore structure on ebullition from peat, *J. Geophys. Res. Biogeosci.*, 121, 1646–1656, doi:10.1002/2015JG003289.

Reeve, A. S., D. I. Siegel, and P. H. Glaser (2000), Simulating vertical flow in large Peatlands, *Journal of Hydrology*, 277, 207–217, doi: 10.1016/S0022-1694(99)00183-3.

Reeve, A.S., R. Evensen, P.H. Glaser, D.I. Siegel, and D.O. Rosenberry (2006), Flow path oscillations in transient ground-water simulations of large peatland systems, *Journal of Hydrology*, 316, 313–324, doi:10.1016/j.jhydrol.2005.05.005.

Reeve, A., Z. Tyczka, X. Comas, and L. Slater (2009), The influence of permeable mineral lenses on peatland hydrology. In: *Carbon Cycling in Northern Peatlands*, edited by A. Baird, L. Belyea, X. Comas, A. Reeve, and L. Slater, L., American Geophysical Union (AGU), pp. 289–298, Washington, D. C., doi: 10.1029/2008GM000825.

Rezanezhad, F., J. S. Price, W. L. Quinton, B. Lennartz, T. Milojevic, and P. Van Cappellen (2016), Structure of peat soils and implications for water storage, flow and solute transport: A review update for geochemists, *Chemical Geology*, 429, 75-84, doi: 10.1016/j.chemgeo.2016.03.010.

Romanowicz, E. A., D. I. Siegel, and P. H. Glaser (1993), Hydraulic reversals and episodic methane emissions during drought cycles in mires, *Geology*, 21, 231–234.

Romanowicz, E. A., D. I. Siegel, J. P. Chanton, and P. H. Glaser (1995), Temporal variations in dissolved methane deep in the Lake Agassiz peatlands, Minnesota (USA), *Global Biogeochem. Cycles*, 9, 197– 212.

Rosa, E., M. Larocque, S. Pellerin, S. Gagne, and R. Fournier (2009), Determining the number of manual measurements required to improve peat thickness estimations by ground penetrating radar, *Earth Surf. Processes Landforms*, 34 (3), 377 – 383, doi: 10.1002/esp.1741.

Rosenberry, D. O., P. H. Glaser, D. I. Siegel, E. P. Weeks (2003), Use of hydraulic head to estimate volumetric gas content and ebullition flux in northern peatlands, *Water Resour. Res.*, 39(3), 1066, doi: 10.1029/2002WR001377.

Rosenberry, D. O., P. H. Glaser, and D. I. Siegel (2006), The hydrology of northern peatlands as affected by biogenic gas: current developments and research needs, *Hydrological Processes*, 20, 3601–3610.

Roulet, N. T., R. Ash, W. Quinton, and T. R. Moore (1993), Methane flux from drained northern peatlands: effect of a persistent water table lowering on flux, *Glob. Biogeochem. Cycles*, 7, 749-769.

Rycroft, D. W., D. J. A. Williams, and H. A. P. Ingram (1975), The transmission of water through peat. I: Review, *J. Ecol.*, 63, 535–556.

Sachs, T., M. Giebels, J. Boike, and L. Kutzbach (2010), Environmental controls on CH_4 emission from polygonal tundra on the microsite scale in the Lena river delta, Siberia, *Global Change Biol.*, 16(11), 3096–3110.

Sander, S.P., J. Abbatt, J.R. Barker, J.B. Burkholder, R.R. Friedl, D.M. Golden, R.E. Huie, C.E. Kolb, M.J. Kurylo, G.K. Moortgat, V.L. Orkin, and P.H. Wine (2011), Chemical Kinetics and Photochemical Data for Use in Atmospheric Studies, Evaluation No. 17, JPL Publication 10-6, Jet Propulsion Laboratory, Pasadena, CA.

Sander, R. (2015), Compilation of Henry's law constants (version 4.0) for water as solvent, Atmos. Chem. Phys., 15, 4399-4981, doi:10.5194/acp-15-4399-2015.

Sass, O., A. Friedmann, G. Haselwanter, and K. F. Wetzel (2010), Investigating thickness and internal structure of alpine mires using conventional and geophysical techniques, *Catena*, 80 (3), 195 – 203, doi:10.1016/j.catena.2009.11.006.

Shannon, R. D. and J. R. White (1994), A three-year study of controls on methane emissions from two Michigan peatlands, *Biogeochemistry*, 27, 35–60.

Siegel, D. I., J. P. Chanton, P. H. Glaser, L. S. Chasar, and D. O. Rosenberry (2001), Estimating methane production rates in bogs and landfills by deuterium enrichment of pore-water, *Global Biogeochem. Cycles*, 15, 967–975.
Simonovski, I. and M. Boltežar (2003), The norms and variances of the Gabor, Morlet and general harmonic wavelet functions, *Journal of Sound and Vibration*, 264(3), 545-557, doi: 10.1016/S0022-460X(02)01206-3.

Singha, K., F. D. Day-Lewis, T. Johnson, L. D. Slater (2015), Advances in interpretation of subsurface processes with time-lapse electrical imaging, *Hydrol. Process.,* 29, 1549–1576, doi: 10.1002/hyp.10280.

Slater, L. and A. Reeve (2002), Understanding peatland hydrology and stratigraphy using integrated electrical geophysics, *Geophysics*, 67, 365–378.

Slater, L., X. Comas, D. Ntarlagiannis, and M. R. Moulik (2007), Resistivity-based monitoring of biogenic gases in peat soils, *Water Resour. Res.*, 43, W10430, doi: 10.1029/2007WR006090.

Spahni, R., R. Wania, L. Neef, M. van Weele, I. Pison, P. Bousquet, C. Frankenberg, P. N. Foster, F. Joos, I. C. Prentice, and P. van Velthoven (2011), Constraining global methane emissions and uptake by ecosystems, *Biogeosciences*, 8(6), 1643–1665.

Stamp, I., A. J. Baird, and C. M. Heppell (2013), The importance of ebullition as a mechanism of methane (CH4) loss to the atmosphere in a northern peatland, *Geophys. Res. Lett.*, *40*, 1-4, doi: 10.1002/grl.50501.

Stocker, T.F., D. Qin, G.-K. Plattner, L.V. Alexander, S.K. Allen, N.L. Bindoff, F.-M. Bréon, J.A. Church, U. Cubasch, S. Emori, P. Forster, P. Friedlingstein, N. Gillett, J.M. Gregory, D.L. Hartmann, E. Jansen, B. Kirtman, R. Knutti, K. Krishna Kumar, P. Lemke, J. Marotzke, V. Masson-Delmotte, G.A. Meehl, I.I. Mokhov, S. Piao, V. Ramaswamy, D. Randall, M. Rhein, M. Rojas, C. Sabine, D. Shindell, L.D. Talley, D.G. Vaughan and S.-P. Xie, 2013: Technical Summary, In: *Climate Change 2013: The Physical Science Basis. Contribution of Working Group I to the Fifth Assessment Report of the Intergovernmental Panel on Climate Change*, edited by Stocker, T.F., D. Qin, G.-K. Plattner, M. Tignor, S.K. Allen, J. Boschung, A. Nauels, Y. Xia, V. Bex and P.M. Midgley, pp. 33-115, Cambridge University Press, Cambridge, United Kingdom and New York, NY, USA.

Stockwell, R. G. (1999), S-Transform analysis of gravity wave activity from a small scale network of airglow imagers, Ph.D. thesis, University of Western Ontario.

Stockwell, R. G., L. Mansinha, and R. P. Lowe (1996), Localization of the complex spectrum: The S-transform, *IEEE Transactions on Signal Processing*, 44(4), 998–1001.

Strack, M., and T. Mierau. (2010), Evaluating Spatial Variability of Free-phase Gas in Peat Using Ground-penetrating Radar and Direct Measurement, *Journal of Geophysical Research*, 115(G2), 1–11, doi: 10.1029/2009JG001045.

Strack, M., E. Kellner, and J. M. Waddington (2005), Dynamics of biogenic gas bubbles in peat and their effects on peatland biogeochemistry, *Global Biogeochem. Cycles*, 19, GB1003, doi:10.1029/2004GB002330.

Strack, M., E. Kellner, and J. M. Waddington (2006), Effect of entrapped gas on peatland surface level fluctuations, *Hydrol. Processes*, 20(17), 3611–3622.

Ström, L., M. Mastepanov, and T. R. Christensen (2005), Species specific effects of vascular plants on carbon turnover and methane emissions from wetlands, *Biogeochemistry*, *75*, 65–82, doi:10.1007/s10533-004-6124-1.

Sundh, I., M. Nilsson, and B. H. Svensson (1992), Depth distribution of methane production and oxidation in a sphagnum peat bog, *Suo*, 5, 267– 269.

Terry, N., L. Slater, X. Comas, A.S. Reeve, K.V.R. Schäfer, and Z. Yu (2016), Free phase gas processes in a northern peatland inferred from autonomous field-scale resistivity imaging, *Water Resour. Res.*, in press, doi: 10.1002/2015WR018111.

Theimer, B. D., D. C. Nobes, and B. G. Warner (1994), A study of the geoelectrical properties of peatlands and their influence on ground-penetrating radar surveying, *Geophys. Prospect.*,42 (3), 179 – 209, doi: 10.1111/j.1365-2478.1994.tb00205.x

Tokida, T., T. Miyazaki, and M. Mizoguchi (2005a), Ebullition of methane from peat with falling atmospheric pressure, *Geophys. Res. Lett.*, *32*, L13823, doi:10.1029/2005GL022949.

Tokida, T., T. Miyazaki, M. Mizoguchi, and K. Seki (2005b), In situ accumulation of methane bubbles in a natural wetland soil, *Eur. J. Soil Sci.*, 56, 389–395, doi:10.1111/j.1365-2389.2004.00674.x.

Tokida, T., T. Miyazaki, M. Mizoguchi, O. Nagata, F. Takakai, A. Kagemoto, and R. Hatano (2007), Falling atmospheric pressure as a trigger for methane ebullition from peatland, *Global Biogeochem. Cycles*, 21, GB2003, doi: 10.1029/2006GB002790.

Topp, G.C., J. L. Davis, and A. P. Annan (1980), Electromagnetic determination of soil-water content: Measurements in coaxial transmission lines, *Water Resour. Res.*, 16, 574–582, doi:10.1029/WR016i003p00574.

Treat, C. C., J. L. Bubier, R. K. Varner, and P. M. Crill (2007), Time scale dependence of environmental and plant-mediated controls on CH_4 flux in a temperate fen, *J. Geophys. Res.*, 112, G01014, doi: 10.1029/02006JG000210.

Turetsky, M. R., C. C. Treat, M. P. Waldrop, J. M. Waddington, J. W. Harden, and A. D. McGuire (2008), Short-term response of methane fluxes and methanogen activity to water table and soil warming manipulations in an Alaskan peatland, *J. Geophys. Res.*, 113, G00A10, doi: 10.1029/2007JG000496.

Turner, G. and A. F. Siggins (1994), Constant Q attenuation of subsurface radar pulses, *Geophysics*, 59, 1192–1200, doi: 10.1190/1.1443677.

van Bellen, S., P.-L. Dallaire, M. Garneau, and Y. Bergeron (2011), Quantifying spatial and temporal Holocene carbon accumulation in ombrotrophic peatlands of the Eastmain region, Quebec, Canada, *Global Biogeochem. Cycles*, 25, GB2016, doi:10.1029/2010GB003877.

von Post, L. (1924), Das genetische System der organogenen Bildungen Schwedens (The genetic system of the organogenic formations of Sweden), *Memoires sur la nomenclature et la classification des sols,* edited by B. Frosterus, International Committee of Soil Science, Helsinki, 287-304.

Waddington, J. M., N. T. Roulet, and R. V. Swanson (1996), Water table control of CH_4 emission enhancement by vascular plants in boreal peatlands, *J. Geophys. Res.*, 101(D17), 22775–22785, doi: 10.1029/96JD02014.

Waddington, J. M., K. Harrison, E. Kellner, and A. J. Baird (2009), Effect of atmospheric pressure and temperature on entrapped gas content in peat, *Hydrol. Process.*, 23, 2970–2980, doi: 10.1002/hyp.7412.

Walter, B.P. and M. Heimann (2000), A process-based, climate-sensitive model to derive methane emissions from natural wetlands: Application to five wetland sites, sensitivity to model parameters, and climate, *Global Biogeochem. Cycles*, 14(3), 745-765, doi: 10.1029/1999GB001204.

Webb, E. K., G. I. Pearman, and R. Leuning (1980), Correction of flux measurements for density effects due to heat and water vapour transfer, *Quart. J. R. Met. Soc.*, 106, 85-100.

Weller, A., A. Bauerochse, and S. Nordsiek (2006), Spectral induced polarisation – a geophysical method for archaeological prospection in peatlands, *Journal of Wetland Archaeology*, 6, 105-125, doi: 10.1179/jwa.2006.6.1.105.

Wharton, R.P., G. A. Hazen, R. N. Rau, and D. L. Best (1980), Advancements in electromagnetic propagation logging, *Soc. Petr. Eng.*, Paper 9041.

Wheast, R.C. (1979), *CRC handbook of chemistry and physics*, CRC Press Inc., Boca Raton. Florida, USA.

Wille, C., L. Kutzbach, T. Sachs, D. Wagner, and E.-M. Pfeiffer (2008), Methane emission from Siberian arctic polygonal tundra: Eddy covariance measurements and modeling, *Global Change Biol.*, 14(6), 1395–1408.

Wright, W., and X. Comas (2016), Estimating methane gas production in peat soils of the Florida Everglades using hydrogeophysical methods, *J. Geophys. Res. Biogeosci.*, 121, 1190–1202, doi:10.1002/2015JG003246.

Yager, R. M. and J. C. Fountain (2001), Effect of natural gas exsolution on specific storage in a confined aquifer undergoing water level decline, *Ground Water*, 39(4), 517–525.

Yang, G., H. Chen, N. Wu, J. Tian, C. Peng, Q. Zhu, D. Zhu, Y. He, Q. Zheng, and C. Zhang (2014a). Effects of soil warming, rainfall reduction and water table level on CH_4 emissions from the Zoige peatland in China, *Soil Biology & Biochemistry*, 78, 83-89.

Yang, X., X. Chen, C. R. Carrigan, and A. L. Ramirez (2014b), Uncertainty quantification of CO_2 saturation estimated from electrical resistance tomography data at the Cranfield site, International Journal of Greenhouse Gas Control, 27, 59-68, doi: 10.1016/j.ijggc.2014.05.006.

Ye, R., Q. Jin, B. Bohannan, J. K. Keller, S. A. McAllister, and S. D. Bridgham (2012), pH controls over anaerobic carbon mineralization, the efficiency of methane production,

and methanogenic pathways in peatlands across an ombrotrophic—Minerotrophic gradient, *Soil Biol. Biochem.*, 54,36–47, doi: 10.1002/2014JG002797.

Yrjala, K., T. Tuomivirta, H. Juottonen, A. Putkinen, K. Lappi, E. S. Tuittila, T. Penttila, K. Minkkinen, J. Laine, K. Peltoniemi, and H. Fritze (2011), CH_4 production and oxidation processes in a boreal fen ecosystem after long-term water table drawdown, *Glob. Change Biol.*, 17, 1311-1320.

Yu, Z., L. D. Slater, K. V. R. Schäfer, A. S. Reeve, and R. K. Varner (2014), Dynamics of methane ebullition from a peat monolith revealed from a dynamic flux chamber system, *J. Geophys. Res. Biogeosci.*, 119, 1789–1806, doi: 10.1002/2014JG002654.

Zhuang, Q., J.M. Melillo, M.C. Sarofim, D.W. Kicklighter, A.D. McGuire, B.S. Felzer, A. Sokolov, R.G. Prinn, P.A. Steudler, and S. Hu (2006), CO2 and CH4 exchanges between land ecosystems and the atmosphere in northern high latitudes over the 21st century, *Geophysical Research Letters*, 33, L17403, doi: 10.1029/2006gl026972.